ANISOTROPY OF MAGNETOCONDUCTIVITY OF METALS

ANISOTROPY OF MAGNETOCONDUCTIVITY OF METALS

By

ROBERT JAMES DOUGLAS, B.Sc. (Hons).

A Thesis

Submitted to the School of Graduate Studies

in Partial Fulfilment of the Requirements

for the Degree

Doctor of Philosophy

McMaster University

August, 1973

DOCTOR OF PHILOSOPHY (1973)
(Physics)

McMASTER UNIVERSITY
Hamilton, Ontario

TITLE: Anisotropy of Magnetoconductivity of Metals

AUTHOR: Robert James Douglas, B.Sc. (Hons) (University of Manitoba)

SUPERVISOR: Dr. W. R. Datars

NUMBER OF PAGES: xiv, 128.

SCOPE AND CONTENTS:

The anisotropy and field dependence of the magnetoresistivity tensor was calculated for aluminum and indium. The calculations used the semi-classical path-integral method, usually in conjunction with a modified nearly-free-electron Fermi surface and a uniform relaxation time. These calculations, and calculations with more general Fermi surfaces and anisotropic relaxation times, were compared with experiment. These calculations were used to interpret experimental induced torque of aluminum. The results of induced torque experiments in high-purity aluminum are presented and are compared with reported four-probe high-field transverse linear magnetoresistance. Calculations are presented which eliminate one class of explanations of the linear magnetoresistance as the major cause of the reported linear magnetoresistance of aluminum.

ABSTRACT

The components of the electrical magnetoconductivity and magnetoresistivity tensors of aluminum and indium were calculated by the path-integral method using closed nearly-free electron Fermi surfaces and a uniform relaxation time. The anisotropy of the components is shown to depend primarily on the symmetry of the Fermi surface in relation to the magnetic field axis. The high-field longitudinal magnetoresistance is found to be a minimum for fields along high-symmetry directions, where the mean orbitally averaged longitudinal component of carrier velocity is a minimum. The anisotropy of the transverse magnetoresistance is larger in indium, which is face centered tetragonal, than in face-centered-cubic aluminum. The calculated Hall coefficients of both metals are isotropic in the high-field regime, but show considerable anisotropy for intermediate fields. The longitudinal-transverse components of magnetoresistivity can saturate at values as high as 0.26 of the zero-field resistivity, but the effects of the longitudinal-transverse magnetoconductivity components on the Hall coefficients and magnetoresistance are small. The calculated results are compared with experiment where possible, and are used to fit the induced torque data for aluminum. The theory reproduces the

field dependence and anisotropy of the induced torque data. Induced torque experiments in high-purity aluminum showed no linear magnetoresistance (slope < 10^{-3}) except for fields within ±3° of <100>. This anomaly was tentatively identified as due to open orbits resulting from magnetic breakdown. Calculations were done which show that the anisotropy of the transverse linear magnetoresistance observed in four-probe experiments cannot be due to an orbital enhancement of the semi-classical transverse conductivity.

The uniform relaxation time path-integral magnetoconductivity was also calculated for Ashcroft's (1963) Fermi surface model of aluminum for a <100> direction. The transverse magnetoresistivity and Hall coefficient were the same as for the nearly-free-electron Fermi surface, but the low-field resistivity and the high-field longitudinal magnetoresistivity were some 50% larger than the nearly-free-electron calculations, and the absolute value of the low-field Hall coefficient was some 20% smaller.

The effects of an anisotropic relaxation time on the calculations were also illustrated. Assuming a different relaxation time for the electron and hole bands was found to explain, qualitatively, the low-field Hall coefficients of indium and aluminum, and their temperature dependences. The

effects of neglecting the nearly free electron α arms of indium were also calculated, and it was found that these effects should be separable from the effects of relaxation time anisotropy if the anisotropy as well as the field dependence of the Hall coefficient of a single sample could be measured.

The path-integral method was found to be a powerful, flexible and economical computational method which was capable of generating physically useful insight. When used with a complete Fermi surface (even a nearly-free electron one), and not just some subset of "representative" orbits, the calculations agreed quite well with experiments. The anisotropy of the magnetoresistivity components was found to be of much greater use in testing transport theories than was the field dependence or the values of the galvanomagnetic coefficients.

ACKNOWLEDGEMENTS

It is with a deep sense of gratitude, and the greatest of pleasure that I acknowledge those who have made my graduate studies at McMaster an exciting and rewarding period of my life. Dr. W. R. Datars, my supervisor, was unstintingly generous of his time, advice and assistance through times of failure and success. I extend my thanks to him, and to those who have shaped the research and educational environment I have enjoyed at McMaster. The faculty members of diverse departments, seminar speakers, post-doctoral fellows, graduate students and undergraduates have all contributed to the great vitality of the university and my experiences here.

I also thank Professor L. M. Falicov and Dr. P.B. Visscher for their helpful communication about the path-integral method. Mr. Clarence Verge provided excellent technical assistance, both for experiments described in this thesis, and for previous, unsuccessful thesis projects. I am grateful to Mr. F. W. Holroyd for providing the initial induced torque data, which was instrumental in establishing confidence in the path-integral calculations; and for numerous useful discussions. Financial support for this research was provided by the National Research Council

of Canada. I gratefully acknowledge personal financial support in the form of graduate fellowships from the International Nickel Company of Canada Limited, and from the National Research Council of Canada.

TABLE OF CONTENTS

LIST OF FIGURES

LIST OF TABLES

CHAPTER I

INTRODUCTION

This thesis is about charge transport in metals. Not all about the transport of electric charge in metals, for that task has already consumed the lifetimes of many physicists and will undoubtedly occupy many more. The scope of this thesis is restricted to the steady state transport of electric charge in single crystals of metals in a magnetic field, at temperatures low enough so that the thermal motions of the crystal lattice do not appreciably affect the transport properties.

The major breakthrough in this field was the development of the concept of the Fermi surface of a metal and its application to transport theory (Lifshitz et al 1956-a, 1956-b, Chambers 1956). This concept (which is discussed further in the next chapter) had such an apparent utility as well as aesthetic appeal that experimentalists developed specific experiments to determine the geometry and other properties of the Fermi surface of metals. For the simpler metals, the data often may be summarised quite accurately using only a few parameters.

The D.C. galvanomagnetic transport properties are

usually average properties of the entire Fermi surface, and as such their utility in determining the Fermi surface parameters is quite limited when compared to other techniques. The most notable exception to this generalisation is the study of bands of "open orbits" on the Fermi surface, since even a narrow band of such orbits can dominate the galvanomagnetic properties of a metal. These studies have proved very useful in the preliminary investigations of many metals to determine the topology and connectivity of their Fermi surfaces.

For the semi-classical transport regime, where quantum oscillatory effects are negligible (that is, the effects of Landau level quantization), the galvanomagnetic properties of a metal, being average properties of the Fermi surface, offer a check on the accuracy of the understanding both of the metal itself, and of transport theories in general. If consistent experimental data are available for the field dependence of the galvanomagnetic properties of a metal, with the field in a large number of crystallographic orientations, and if the Fermi surface parameters are determined, then the transport theorist has a testing ground for transport theories. Ideally, all of the galvanomagnetic data would be taken from a single sample, and the Fermiologist would have measured the Landau level widths to obtain information on the scattering of the conduction electrons in this same sample. This approach would offer a direct comparison of theory with experimental data using no free parameters, and has become technically feasible in the noble metals only rather recently.

If the scattering information is not available, some additional assumption about the form of the scattering must be made, and free parameters must be introduced. This is the approach taken in this thesis: to compare theoretical predictions of few-parameter models to measured field dependences and anisotropies of the galvanomagnetic properties.

Aluminum and indium are, in many ways, ideal candidates for such a project. Their galvanomagnetic properties are largely devoid of the complexities which open orbits introduce. The paths of most charge carriers are far from free-electron like, which may generate interesting galvanomagnetic anisotropy; and yet the Fermi surfaces are close to being re-mapped spheres. The major obstacle in mounting such a program for these metals was the lack of a consistent picture of the galvanomagnetic properties of monocrystalline indium and aluminum. Until recently, of the magnetoresistivity components of these two metals, only the Hall terms in aluminum had shown any real experimental consistency (Forsvoll and Holwech (1965)). Magnetoresistance measurements (Balcombe (1963), Volotskaya (1963), Borovik and Volotskaya (1965), Chiang et al (1969), Balcombe and Parker (1970), Kesternich and Ullmaier (1971)) using the conventional four-probe technique show a very wide range of high-field magnetoresistance behaviour. Feder and Lothe (1965) calculated the field dependence of the galvanomagnetic properties of aluminum with the magnetic field along <001>, but their limited agreement with Balcombe's (1963) measurements did not provide encourage-

ment to calculate the galvanomagnetic anisotropy. The anisotropy was apparently viewed as a more difficult problem than the field dependence, both experimentally and theoretically.

With the advent of the extensive, and fully reproducible galvanomagnetic measurements of Holroyd et al (1973), the major obstacle was removed for aluminum. These measurements were not conventional four-lead measurements, but were induced torque measurements. This leadless technique permitted the investigation of the field dependence of the galvanomagnetic properties of each sample for all field directions in the (100), (110) and (112) planes. The penalty which this technique inflicts is a small one: the induced torque is a scrambled function of the calculated magnetoconductivity components (Visscher and Falicov, 1970), but only slightly more scrambled than are the quantities measured in four-probe measurements.

The calculations required to make such a comparison of these extensive induced torque data with theory, as well as other calculations which followed from them, make up this thesis. As well as this direct comparison, the calculated results of aluminum and indium are presented in some detail, together with some more general insights which may prove useful in understanding the galvanomagnetic properties of other metals. The calculated results are compared to other

experiments where possible, and extended where necessary. The induced torque anisotropy of high-purity aluminum was measured in a search for the linear transverse magnetoresistance which is measured in many four-probe experiments. One class of possible explanations for the linear magnetoresistance was investigated and the calculated anisotropy compared to the measured four-probe anisotropy of the linear term.

CHAPTER II

THEORY

A. The Goal of Magnetoconductivity Theories

The transport of electric charge by metallic crystals depends on the applied electric and magnetic fields, as well as the internal structure of the metal. The electric current resulting from an applied static electric field $\vec{E}$, for our purposes here, is sufficiently well described by linear response theory (the Ohm's Law regime). Because the electric current density, $\vec{J}$, and the electric field are not in general co-linear, the linear response is a second rank tensor, $\overleftrightarrow{\sigma}$, where

$$\vec{J} = \overleftrightarrow{\sigma}\vec{E}. \qquad [1]$$

The conductivity tensor $\overleftrightarrow{\sigma}$, for a particular crystal, is a tensor function of the applied magnetic field vector $\vec{H}$, depending on both the direction and magnitude of $\vec{H}$. The goal of any magnetoconductivity theory is to predict the field dependence and anisotropy of the nine components of $\overleftrightarrow{\sigma}$ as the field magnitude and direction are varied, and to do this in terms of a small number of parameters (the Fermi surface parameters).

B. Electrons in Metals

The charge carriers in metals are the mobile conduction electrons which are not localized to a particular atomic ion core, but move through the periodic potential of the positive ion cores. A very useful picture of this complex many-body system is to consider one electron moving in the medium of the other electrons and ion cores. The major effect that the medium of the other conduction electrons has is the screening of the strong, long-range Coulomb interaction, which leaves a much weaker short-range interaction. The electron which we have singled out moves through an effective screened potential of the ion cores which is rather weak. The solutions to the Schrödinger wave equation describing a charged particle moving through a periodic potential are Bloch states $|\vec{k}\rangle$, where $\vec{k}$ is the wavevector (the quasi-momentum divided by $\hbar$, where $\hbar$ is Planck's constant divided by 2π). There are only certain allowed energies, $\varepsilon_i(\vec{k})$ for each wavevector: the subscript i is referred to as the band index.

These single-particle energy states are filled by the conduction electrons to minimize the total free energy while at the same time putting only two electrons per state $|i,\vec{k}\rangle$ (one spin up and one spin down) as prescribed by the Pauli exclusion principle. Thus, in the absence of interactions between the electrons, the single particle electron energy

bands would be filled to a certain energy, E_F - the Fermi energy, and empty above E_F. The screened Coulomb interaction introduces correlations which act to spread the occupancy of the energy bands, but does not remove the zero-temperature (T = 0) discontinuity in occupancy at the Fermi energy. The surface in k-space which is described by $\epsilon_i(\vec{k}) = \epsilon_F$ is the Fermi surface of the ith band.

For many metals the nearly free electron Fermi surface is a good approximation to the experimentally deduced Fermi surface, due to the greatly weakened screened Coulomb potential. This surface, also known as the single orthogonalized plane wave (single-OPW) Fermi surface is easily obtained for any metal using the Harrison (1960) construction of re-mapped spheres. For many metals there is significant deviation from the single-OPW surface only in the vicinity of Brillouin zone boundaries, where the sharp cusps of the single-OPW Fermi surface are rounded by the finite size of the lattice potential. In Fig. 1-b and 1-c the single-OPW Fermi surface of aluminum is shown, and for comparison the four-OPW pseudopotential third band model of Ashcroft (1963) is also shown. The surface identified as a "hole" surface in Fig. 1, has its interior states $\vec{k}$ unoccupied, while the "electron" surfaces have their interior states occupied. In a magnetic field, carriers on these two types of surface

Figure 1-a

The Brillouin zone of face centered cubic aluminum.

Figure 1-b

The single-OPW second band hole Fermi surface of aluminum. The only major difference of the four-OPW hole surface from this is a rounding of the sharp single-OPW cusps.

Figure 1-c

The single-OPW third band electron Fermi surface of aluminum.

Figure 1-d

The four-OPW third band electron Fermi surface of aluminum, after Ashcroft (1963).

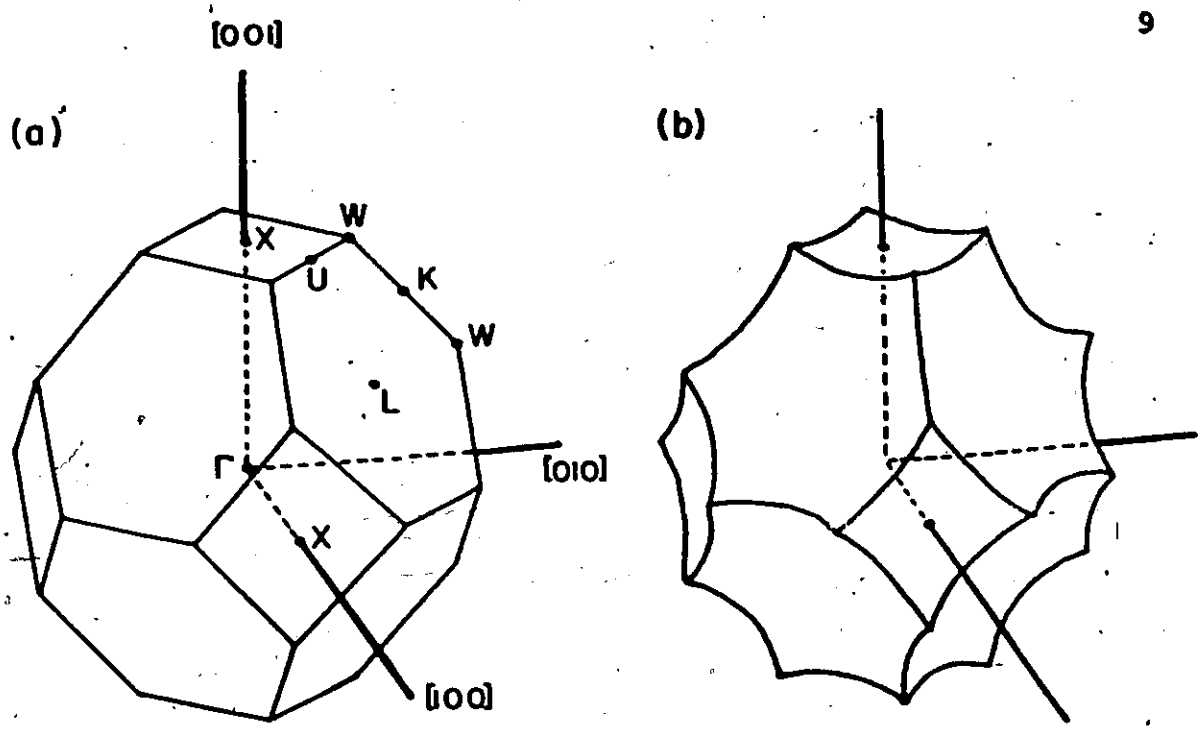

Aluminum

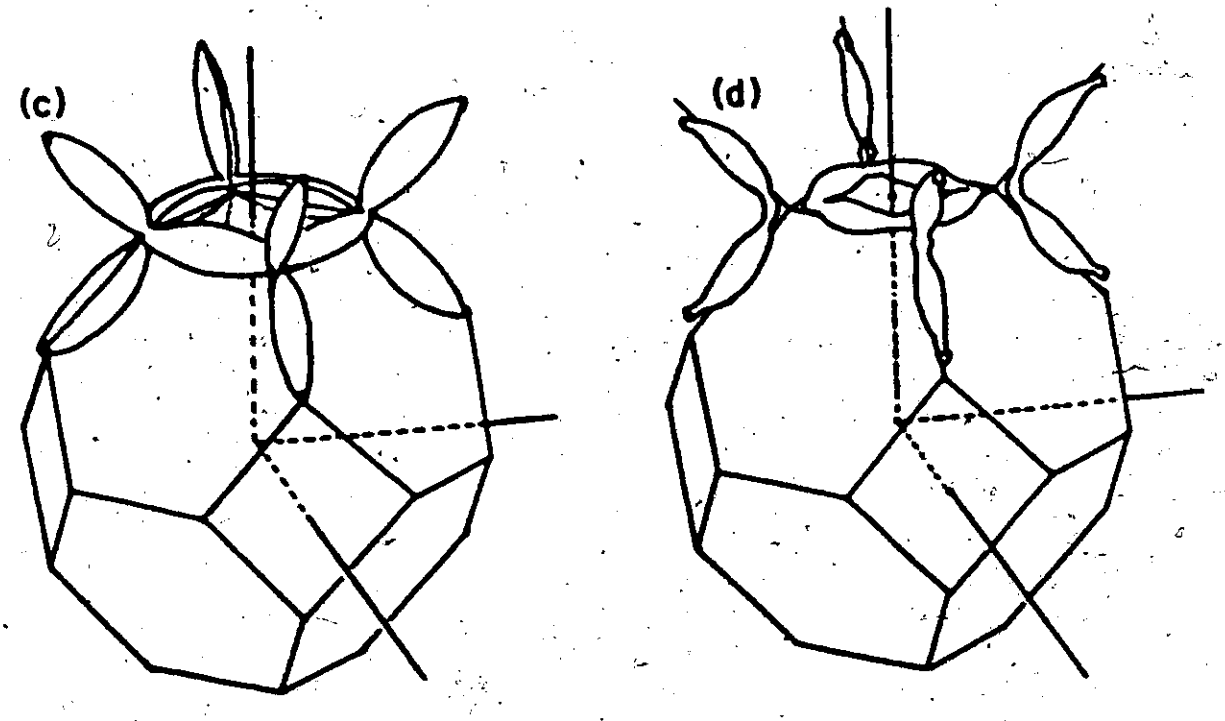

traverse their orbits (in both real and reciprocal space) in opposite senses. This fact has observable effects in the galvanomagnetic properties of metals, and so is a useful distinction to make.

The electrons within energy k_BT (where k_B is the Boltzmann constant) of the Fermi surface dominate electronic transport properties, since only at the Fermi surface is there a large number of occupied states separated from a large number of unoccupied states by a small energy difference; and any electronic transport will be dominated by those states where a minimal amount of energy can result in a maximal displacement of the electronic distribution from equilibrium.

C. Quasiparticles in Metals

For electronic transport properties, it is advantageous to think of quasiparticles rather than electrons. A quasiparticle is an excitation of the ground state of a metal - for a metal at T = 0 with no electric field present, the quasiparticle density is zero. The quasiparticle is the carrier of energy in a metal and should not be confused with the structural unit of the electronic sea - the electron, although both have the same charge. The utility of this concept lies in the fact that at low temperatures, the quasiparticle density is low, and the quasiparticles are constrained to be near the Fermi surface. The quasiparticle velocity (or Fermi velocity) is $v(\vec{k})$, where

$$\vec{v}(\vec{k}) = \frac{1}{\hbar} \nabla_k \, \varepsilon(\vec{k}) \Big|_{\varepsilon(\vec{k}) = \varepsilon_F} \qquad [2]$$

Copious data are available about the geometry of the Fermi surface and the Fermi velocity for many metals. These data are available as inputs to any magnetoconductivity theory.

D. Boltzmann Equation

The distribution of conduction electrons in phase space, $f(\vec{k},\vec{r})$, will depend on the externally applied fields, and will differ from $f^{\circ}(\vec{k},\vec{r})$, the zero-field equilibrium concentration at $\vec{r}$ of electrons in state $\vec{k}$. The electronic transport properties depend on the difference between $f(\vec{k},\vec{r})$ and $f^{\circ}(\vec{k},\vec{r})$, denoted by $g(\vec{k},\vec{r})$. This difference may be determined in some cases from the boundary conditions appropriate to the problem, and from the Boltzmann transport equation which states that the sum of the time rates of change of $f(\vec{k},\vec{r})$ must be zero for steady-state transport:

$$\frac{\partial f(\vec{k},\vec{r})}{\partial t}\Big|_{\text{fields}} + \frac{\partial f(\vec{k},\vec{r})}{\partial t}\Big|_{\text{scattering}} + \frac{\partial f(\vec{k},\vec{r})}{\partial t}\Big|_{\text{diffusion}} = 0 \qquad [3]$$

The first term, due to externally applied fields, is perhaps the simplest to deal with, that is

$$\frac{\partial f(\vec{k},\vec{r})}{\partial t}\Big|_{\text{fields}} = -\dot{\vec{k}} \cdot \nabla_k f(\vec{k},\vec{r})$$

$$= -\frac{e}{\hbar}\left(\vec{E} + \frac{1}{c}\,\vec{v}(\vec{k},\vec{r}) \times \vec{B}\right) \cdot \nabla_k f(\vec{k},\vec{r}) \qquad [4]$$

where e is the charge of an electron, and $\vec{B} = \vec{\mu}\vec{H}$. (For most of this work we will make no great distinction between the magnetic field $\vec{H}$ and the magnetic induction, $\vec{B}$.) Equation [4] is derived (Ziman (1964), pg. 179) from the assumption of the Liouville theorem, and the external Coulomb and Lorentz forces applied to electrons, where $\vec{v}(\vec{k},\vec{r})$ is the velocity of electrons in state $\vec{k}$ in the vicinity of $\vec{r}$.

The diffusion term, similarly is

$$\left.\frac{\partial f(\vec{k},\vec{r})}{\partial t}\right|_{\text{diffusion}} = -\vec{v}(\vec{k},\vec{r})\cdot\nabla_r f(\vec{k},\vec{r}), \qquad [5]$$

which is usually neglected in magnetoconductivity theories, with the justification that the ideal sample is homogeneous, so that $\nabla_r f(\vec{k},\vec{r})$ is zero, and the $\vec{r}$ dependences of $f(\vec{k},\vec{r})$, $f^{\circ}(\vec{k},\vec{r})$ and $g(\vec{k},\vec{r})$ disappear. This point will be discussed again in conjunction with the observed linear magnetoresistance of some metals.

The scattering term can be dealt with on different levels. We have used the simplest treatment in this work, having assumed that the scattering may be adequately described using a relaxation time $\tau(\vec{k})$, defined over the Fermi surface:

$$\left.\frac{\partial f(\vec{k},\vec{r})}{\partial t}\right|_{\text{scattering}} = \frac{g(\vec{k},\vec{r})}{\tau(\vec{k})}. \qquad [6]$$

We also assume that an excitation at $\vec{k}$ (near the Fermi surface) is scattered equally to all states at the Fermi surface.

Since this kind of scattering is, for the most part, large-angle scattering which results in quasiparticle destruction, it will be identified as catastrophic scattering. In practice, we have usually assumed τ to be isotropic, so that there is but a single adjustable parameter available to describe the tensor function $\overleftrightarrow{\sigma}(\vec{H})$. We have also used different relaxation times on different bands (Chapter VI), but even these were constant over the individual bands.

E. The Path-Integral Method

If we can also neglect the effects of the Landau level quantization of the electrons (discussed further in Chapter VI), then the zero-temperature limit to the linearized Boltzmann transport equation is the Chambers path-integral formula (Chambers, 1956).

With the magnetic field in the z direction, a set of cyclotron orbits over the Fermi surface is selected around which the quasiparticles are driven by the Lorentz force, at constant k_z. This set of orbits depends on the crystallographic orientation of the magnetic field, so for any particular field orientation, the conductivity tensor components, $\sigma_{ij}(B)$, are given by the integral over all these orbits (i.e. all k_z of the Brillouin zone) for each band of the path integral of the Fermi velocity components $(v_i(\vec{k}))$ weighted by a relaxation factor.

$$\sigma_{ij}(B) = \frac{m_o e^2}{4\pi^3 \hbar^2 \omega_o} \int_{\text{zone}} dk_z \sum_{\substack{\text{all}\\ \text{orbits}}} \int_{\substack{\text{around}\\ \text{orbit}}} d\theta v_j(\theta,k_z) \int_{-\infty}^{\theta} d\psi v_i(\psi,k_z) \qquad [7]$$

$$\exp\{\frac{\psi-\theta}{\omega_o \tau(\vec{k})}\}$$

where m_o is the free electron mass, and we use $\omega_o = \frac{eB}{m_o c}$ as the field parameter for convenience; but this in no way restricts the band structure for which eq. [7] is valid. The phase variables ψ and θ are defined by integrals along the orbit: $\int \frac{\hbar|d\vec{k}|}{m_o v_\perp}$, where $v_\perp = \sqrt{v_x^2 + v_y^2}$.

Equation [7] would be a standard numerical integration for any band structure, were it not for the $-\infty$ as the lower limit on the integration over ψ. The efficient evaluation of the path integral around each orbit was accomplished by approximating the orbit with N contiguous circular arcs and considering $v_z, v_\perp, k_z, k_\perp = \sqrt{k_x^2 + k_y^2}$ and $\tau(\vec{k})$ to be constant on each arc. For our single-OPW Fermi surface this involved no additional approximation, but for any other Fermi surface, N must be adjusted to make these approximations of the calculation reasonable. Also, on the ℓth arc, it was more convenient to use a geometrical angle γ such that $v_x = v_\perp^\ell \cos\gamma$ and $v_y = v_\perp^\ell \sin\gamma$, rather than the phase variable θ. Then

$$d\theta = \frac{\hbar k_\perp^{\ell}}{m_o v_\perp^{\ell}} d\gamma$$

$$\equiv a_\ell d\gamma \qquad [8]$$

and on the ℓth arc γ is taken from α_ℓ to β_ℓ. On the ℓth arc, we also define the relaxation time anisotropy, b_ℓ, by $\tau(\vec{k}) = \tau b_\ell$ where τ is an average relaxation time. We define the transport anisotropy as $c_\ell = a_\ell/b_\ell$, which is the anisotropy of the inverse of $\omega\tau$.

It is useful to define fifteen orbit integrals and to express them in terms of integrals which have analytic forms over the circular arcs (Falicov; private communication). With the phase variable going from 0 to ϕ for one traversal of the orbit, these orbit integrals are:

$$A_i(\omega_o\tau) \equiv \int_0^{\phi} d\theta v_i(\theta) \exp\{\frac{\theta-\phi}{\omega_o\tau(\vec{k})}\}$$

$$= \sum_{\ell=1}^{N} \exp\{-\frac{1}{\omega_o\tau} \sum_{k=\ell+1}^{N} (\beta_k-\alpha_k)c_k\} a_\ell \int_{\alpha_\ell}^{\beta_\ell} d\gamma v_i(\gamma) \exp\{\frac{(\gamma-\beta_\ell)c_\ell}{\omega_o\tau}\} \qquad [9]$$

$$B_i(\omega_o\tau) \equiv \int_0^{\phi} d\theta v_i(\theta) \exp\{\frac{-\theta}{\omega_o\tau(\vec{k})}\}$$

$$= \sum_{\ell=1}^{N} \exp\{-\frac{1}{\omega_o\tau} \sum_{k=1}^{\ell-1} (\beta_k-\alpha_k)c_k\} a_\ell \int_{\alpha_\ell}^{\beta_\ell} d\gamma v_i(\gamma) \exp\{\frac{(\alpha_\ell-\gamma)c_\ell}{\omega_o\tau}\} \qquad [10]$$

$$C_{ij}\ (\omega_o\tau) \equiv \int_0^{\phi} d\theta \int_0^{\theta} d\theta' v_i(\theta) v_j(\theta') \exp\{\frac{\theta'-\theta}{\omega_o\tau(\vec{k})}\}$$

$$= \sum_{k=1}^{N} a_k^2 \int_{\alpha_k}^{\beta_k} d\gamma \int_{\alpha_k}^{\gamma} d\gamma' v_i(\gamma) v_j(\gamma') \exp\{\frac{(\gamma'-\gamma)c_k}{\omega_o\tau}\}$$

$$+ a_k \int_{\alpha_k}^{\beta_k} d\gamma v_i(\gamma) \exp\{\frac{(\alpha_k-\gamma)c_k}{\omega_o\tau}\} \sum_{\ell=1}^{k-1} \exp\{-\frac{1}{\omega_o\tau} \sum_{n=\ell+1}^{k-1} (\beta_n-\alpha_n)c_n\}$$

$$\times a_\ell \int_{\alpha_\ell}^{\beta_\ell} d\gamma v_j(\gamma) \exp\{\frac{(\gamma-\beta_\ell)c_\ell}{\omega_o\tau}\} . \qquad [11]$$

The definite integrals which will account for previous traversals of the orbit into the infinitely remote past are defined as

$$D_i(\omega_o\tau) \equiv \int_{-\infty} d\theta v_i(\theta) \exp\{\theta/\omega_o\tau(\vec{k})\}$$

$$= A_i/(1-\exp\{-\phi/\omega_o\tau\})$$

$$= A_i/(1-\exp\{-\frac{1}{\omega_o\tau} \sum_{j=1}^{N} (\beta_j-\alpha_j)c_j\}). \qquad [12]$$

Using [9]-[12] in [7] results in the differential conductivity

$$\frac{d\sigma_{ij}(k_z)}{dk_z} = \frac{m_o e^2}{4\pi^3\hbar^2\omega_o} \sum_{\substack{\text{all}\\ \text{orbits}}} (B_i D_j + C_{ij}). \qquad [13]$$

Numerical integration of [13] with respect to k_z gives the conductivity tensor component for a particular $\omega_o\tau$ and crystallographic orientation in the case of uniquely defined orbits (no magnetic breakdown or "hot spot" scattering (Young, 1968)). The semi-classical effects of magnetic breakdown may be included in eqs. [9]-[13] as an extension of the present theory (Falicov and Sievert 1965).

The fifteen orbit integrals (A_i, B_i and C_{ij}) were evaluated for each $\omega_o\tau$ in terms of the Fermi parameters of the N arcs comprising the orbit. For most of the calculations herein described, an isotropic relaxation time ($b_\ell = 1$) was assumed for all ℓ and all k_z, although for some calculations b_ℓ was allowed to be different for the different electronic bands. The magnitude of the Fermi velocity was taken to be constant for each arc, and for the single-OPW calculations, was taken to be constant for all arcs. For other band structures, the Fermi velocity must be determined for each arc using Eq. [2].

A uniform electron-phonon mass enhancement ($a_\ell = (1+\lambda)$) can easily be included. The bare cyclotron frequency ω_o (henceforth ω) and the bare relaxation time τ are oppositely affected by the electron-phonon interaction (Prange and Kadanoff, 1964), so that $b_\ell = (1+\lambda)$ and $c_\ell = 1$. It should be emphasized that $\omega\tau$ remains unaffected by the electron-phonon interaction, that is $\omega\tau=\omega^*\tau^*$, (where the stars denote dressed quantities), and that the conductivity is scaled by τ, not τ^*. With any measured

cyclotron frequency ω_c, of a particular orbit, τ^* should be used to obtain a value of $\omega\tau$.

The efficient numerical integration of eq. [13] with respect to k_z requires some knowledge of the k_z variation of the integrands. The variation of the high-field ($\omega\tau$=100) differential conductivities with respect to k_z for the second-band hole surface of aluminum is shown in Fig. 2 for the field along a <012> direction. For a spherical Fermi surface, these curves would be parabolas opening down, excepting the zz component for which the parabola would open upward. The different forms in Fig. 2 arise from the complex manner in which the orbit changes with k_z. At high fields the differential Hall component, $d\sigma_{xy}/dk_z$ is directly proportional to the orbital area in reciprocal space. Thus, $d\sigma_{xy}/dk_z$ is a smooth function of k_z in the high-field limit. The k_z integration of the transverse differential conductivities requires more care since they are discontinous when segments of an orbit with large v_x and v_y are cut off as k_z is varied. The differential longitudinal component $d\sigma_{zz}/dk_z$, has large discontinuities where there is a limit point orbit. The width of this region in Fig. 2 is about 3×10^{-3} $\mathring{A}^{-1}$ at k_z = 1.198 $\mathring{A}^{-1}$. This narrow set of orbits contributes about 1% to σ_{zz} in the high-field region.

Thus, to ensure convergence of the k_z integrals to their true values, cuts were taken through the Fermi surface

Figure 2. The contribution to the various conductivity components of the orbits at each k_z on the second band hole surface with the field along $[\bar{1}02]$, y along [010] and $\omega\tau = 100$. Note the different scale factors and origins for the four components that are shown. To the right are shown representative orbits, each with its k_z value. Note in particular the limit point orbit $k_z = 1.198\ \mathring{A}^{-1}$, and its contribution to σ_{zz}, which is off the graph by about a factor of two.

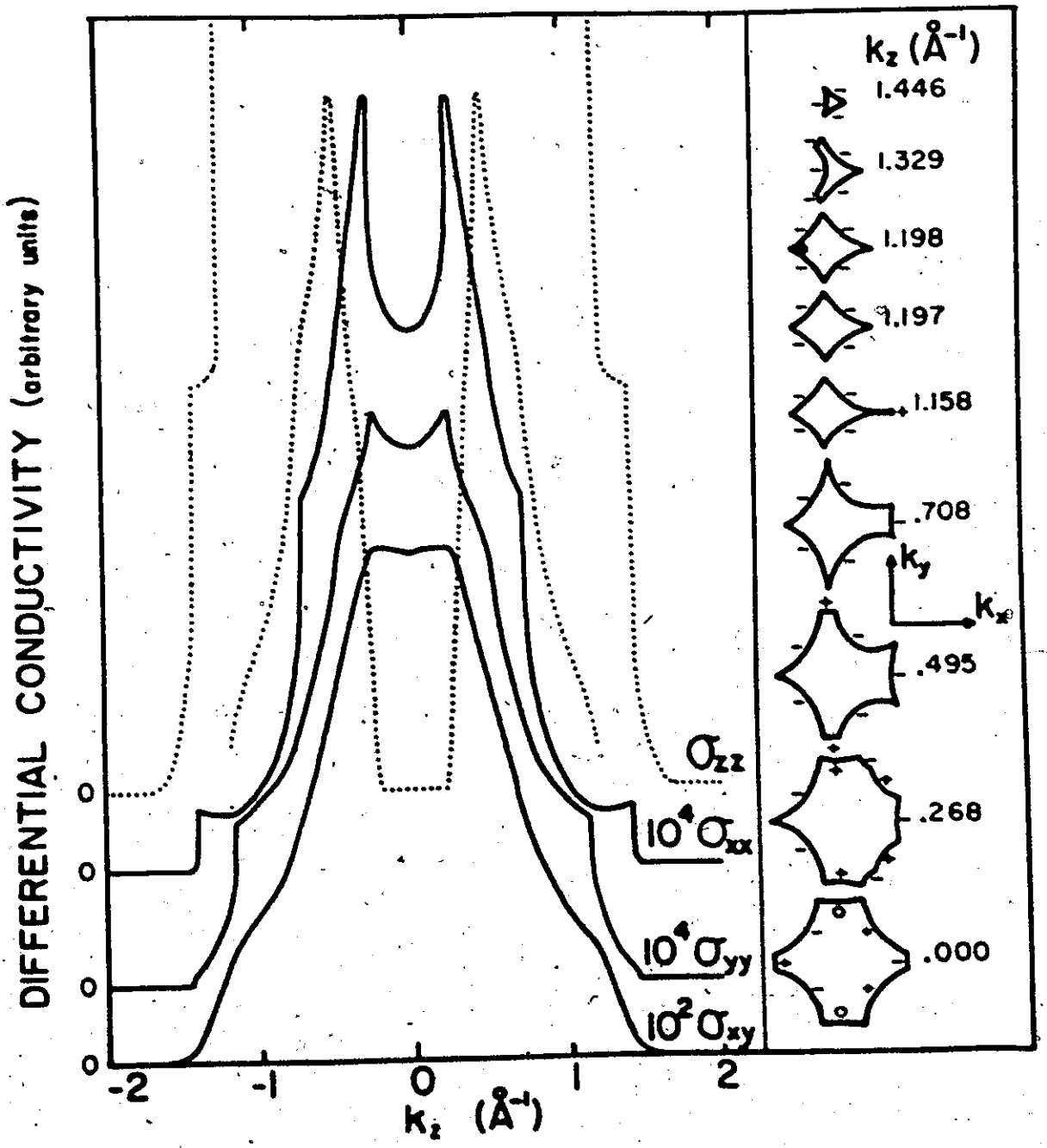
DIFFERENTIAL CONDUCTIVITY (arbitrary units)
0
0
0
0
-2
-1
0
1
2
k_z (Å^{-1})
σ_{zz}
$10^4\sigma_{xx}$
$10^4\sigma_{yy}$
$10^2\sigma_{xy}$
k_z (Å^{-1})
1.446
1.329
1.198
1.197
1.158
.708
.495
.268
.000
k_y
k_x

at a nominal k_z spacing of from $k_F/60$ to $k_F/100$ (k_F is the free electron Fermi radius), and the cut spacing was decreased as required using an adaptive algorithm. The cut spacing was decreased in k_z regions where one or more of the $\left|\frac{d^2\sigma_{ij}}{dk_z^2}\right|$'s were large. These regions occurred only where the character of one or more of the orbits changed (see Fig. 2). The symmetry of the differential conductivity components about $k_z = 0$ which is apparent in Fig. 2 is a consequence of the inversion symmetry of the Fermi surface about Γ. This symmetry was used to reduce the required range of k_z integration by a factor of two. With z in a mirror plane, or along an axis of n-fold symmetry, the orbital path integrals could be reduced by factors of 2 and n, respectively.

F. Useful Distinctions

F.1 Compensated and Uncompensated Metals

Metals with equal reciprocal-space volumes of electrons and holes (those with an even number of conduction electrons per unit cell) are referred to as compensated metals. This seemingly minor distinction changes the high-field dependence of the Hall term, σ_{xy} from H^{-1} to a more rapid H^{-2} field dependence. This may be seen in the log-log graphs in Fig. 3a and 3b, where we compare the calculated <100> field dependences of $\sigma_{ij}(H)$ for the single-OPW Fermi surfaces of aluminum (uncompensated) and lead (compensated). The field dependence of σ_{xy} for lead is largely H^{-3} ($\vec{H}$ being in a mirror plane means there is no H^{-2} term of σ_{xy} in the high-

Figure 3. A comparison of the calculated field dependence of an uncompensated metal (aluminum) and a compensated metal (lead) for the field along four-fold axis. The calculations used the path-integral method and assumed a uniform relaxation time and the single-OPW Fermi surfaces. Both metals are face centered cubic and for the field along <100> their single-OPW Fermi surfaces support no open orbits. Aluminum has three valence electrons per atom, and lead has four.

Figure 3-a. The field dependence of the conductivity components of aluminum, divided by the relaxation time. Note that σ_{xy} has an $(\omega\tau)^{-1}$ (or H^{-1}) field dependence in the high-field limit.

Figure 3-b. The field dependence of the conductivity components of lead, divided by the relaxation time. σ_{xy} has only a small high-field H^{-1} term, which should be identically zero but for the numerical inaccuracies of the calculations (<0.1%).

Figure 3-c. The field dependence of the resistivity components of aluminum, multiplied by the relaxation time.

Figure 3-d. The field dependence of the resistivity components of lead, multiplied by the relaxation time.

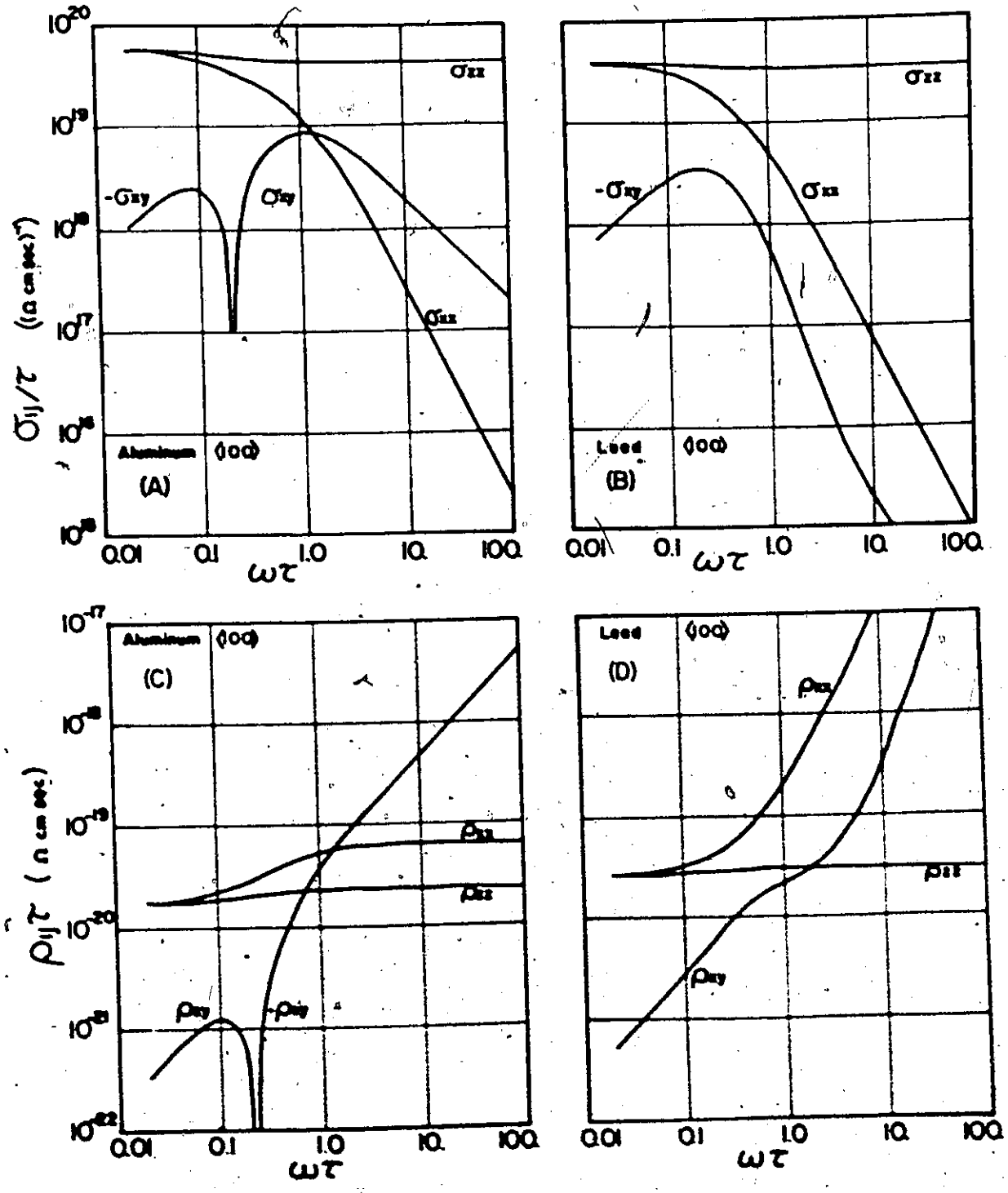
Aluminum ⟨100⟩
(A)
Lead ⟨100⟩
(B)
Aluminum ⟨100⟩
(C)
Lead ⟨100⟩
(D)
σ_{ij}/τ ((Ω cm sec)$^{-1}$)
$\rho_{ij}\tau$ (Ω cm sec)
$\omega\tau$
0.01
0.1
1.0
10
100

field limit) with a small H^{-1} term which reflects the numerical inaccuracies in determining the electron and hole surface volumes, which is less than 0.1%. This apparently minor difference in the Hall term of the conductivity tensor of compensated and uncompensated metals, has a dramatic effect on the field dependences of most of the resistivity tensor components $\overleftrightarrow{\rho}_{ij}(\vec{H}) = (\overleftrightarrow{\sigma}(\vec{H}))^{-1}_{ij}$, as may be seen by comparing Fig. 3c and 3d. The transverse magnetoresistivity of aluminum has saturated in the high-field limit, while that of lead has an H^2 field dependence.

F.2 Open Orbits and Closed Orbits

A similarly dramatic effect occurs in the field dependence of the magnetoresistivity if an open orbit exists in the x-z plane for some range (even a very small range) of k_z. This is illustrated in Fig. 4 for indium. Fig. 4b and 4d are the single-OPW conductivity and resistivity field dependences of indium (uncompensated, with the field in the [100] direction, where there is an open orbit along the x direction ([010]) in reciprocal space which is indicated by the dotted line on the second band hole surface of indium in Fig. 5b. Figures 4a and 4c are the same as 4b and 4d respectively, except that the second band hole Fermi surface has been slightly modified at W to remove the open orbits.

These dramatic effects have been observed and used to study Fermi surface volumes and connectivity for some 2 decades. It is the purpose of this thesis to show

Figure 4. A comparison of the calculated field dependence of the conductivity and resistivity components of indium for closed and open Fermi surfaces with the field in the <100> direction. These path-integral calculations used a uniform relaxation time and either the single-OPW Fermi surface (4-b and 4-d), or these surfaces modified to exclude open orbits by cutting the connections between the second band hole surfaces at W (4-a and 4-c). The open orbit in real space is along the four-fold axis - the y axis.

Figure 4-a. The field dependence of the conductivity components of indium, divided by the relaxation time, for a closed Fermi surface.

Figure 4-b. The field dependence of the conductivity components of indium, divided by the relaxation time, for the single-OPW Fermi surface, with its band of open orbits.

Figure 4-c. The field dependence of the resistivity components of indium, multiplied by the relaxation time, for a closed Fermi surface.

Figure 4-d. The field dependence of the resistivity components of indium, multiplied by the relaxation time, for the single-OPW Fermi surface, with its band of open orbits.

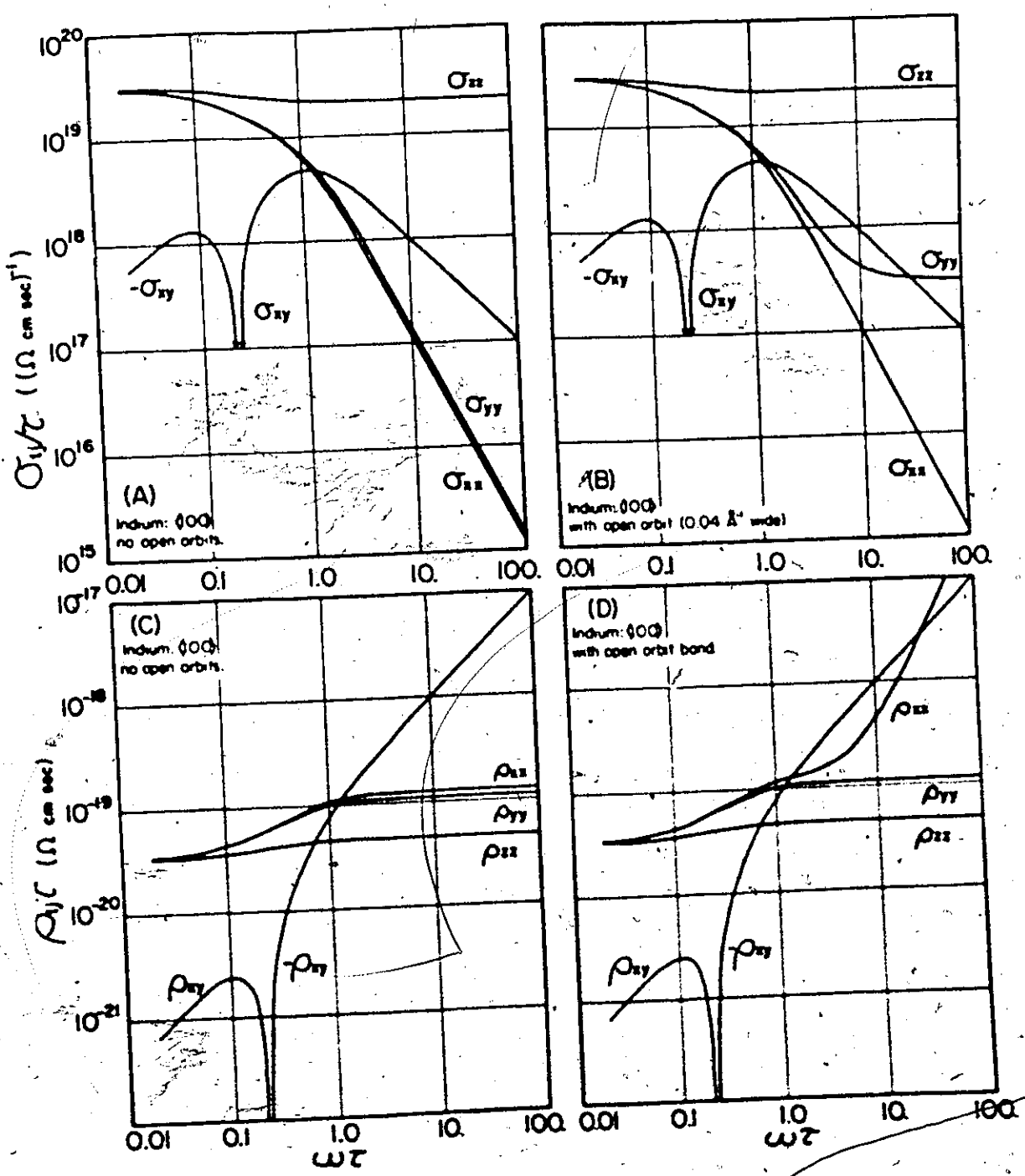
(A)
Indium: ⟨001⟩
no open orbits.
(B)
Indium: ⟨001⟩
with open orbit (0.04 Å⁻¹ wide)
(C)
Indium: ⟨001⟩
no open orbits.
(D)
Indium: ⟨001⟩
with open orbit band
σ_{zz}
σ_{yy}
σ_{xx}
$-\sigma_{xy}$
σ_{xy}
ρ_{xx}
ρ_{yy}
ρ_{zz}
$-\rho_{xy}$
ρ_{xy}
$\sigma_{ij}\tau$ ((Ω cm sec)⁻¹)
$\rho_{ij}\tau$ (Ω cm sec)
$\omega\tau$
0.01
0.1
1.0
10.
100.

Figure 5-a. The Brillouin zone of face centered tetragonal indium.

Figure 5-b. The single-OPW second band hole Fermi surface of indium. The dotted line shows the open orbit which exists for fields in the [100] direction. The black parts of the surface, near the W points (but not the T points) of the zone, are regions where the hole surface touches the zone boundary in the single-OPW model. In our modified single-OPW model these regions do not touch the zone boundary.

Figure 5-c. The single-OPW third band electron Fermi surface of indium. The hatched arms are the α-arms, and the unhatched arms are the β-arms.

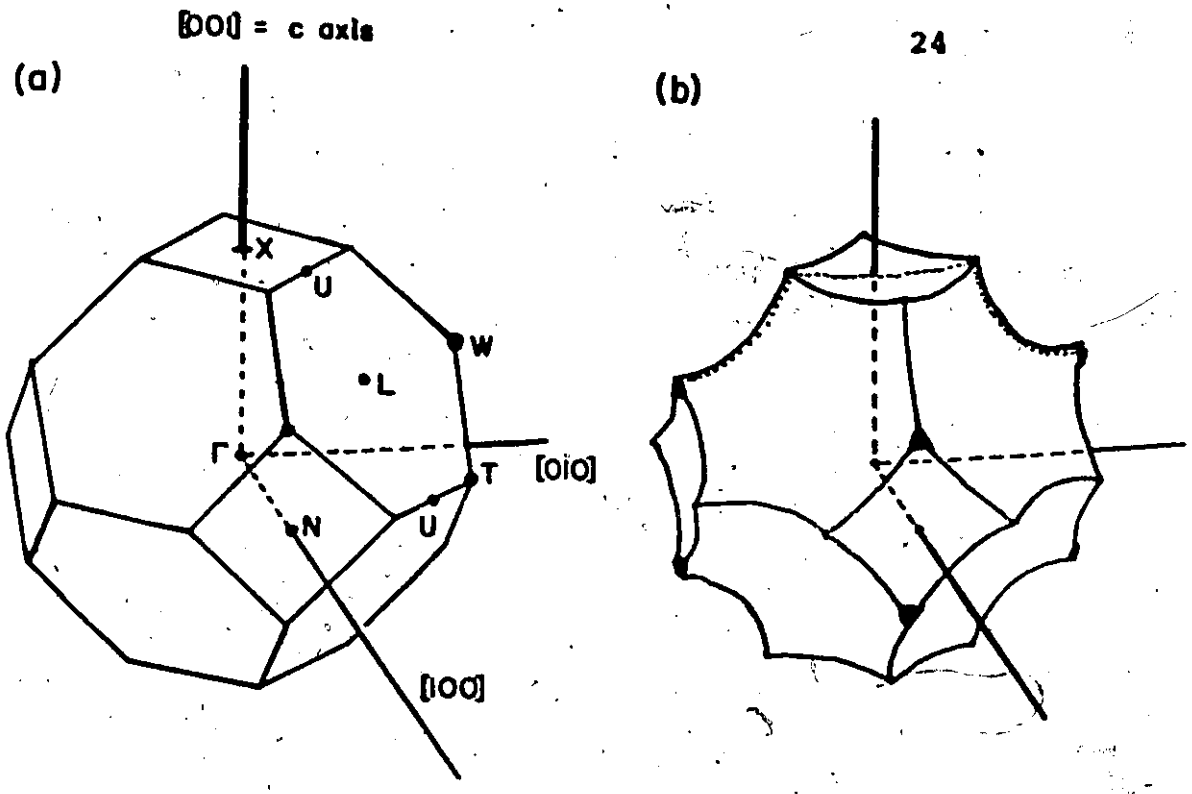

Indium

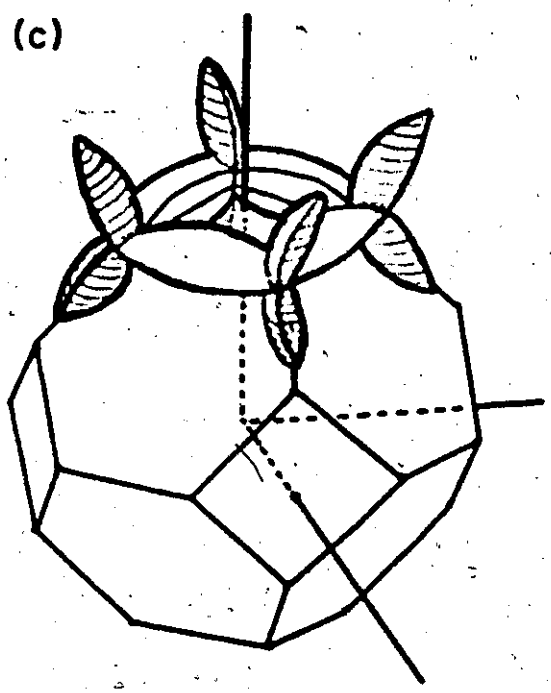

how the geometry of closed Fermi surfaces of uncompensated metals relates to the anisotropy of the magnetoconductivity tensor components. The restriction to closed Fermi surfaces avoids the obscuring complexity of anisotropy due to open orbits, which is fully understood in principle. The restriction to uncompensated metals means that the Hall coefficient and the magnetoresistance should saturate in the high-field limit. Besides the alkali metals, which have nearly spherical Fermi surfaces, there are only two simple metals which are uncompensated and have closed Fermi surfaces: aluminum and indium, and these two metals are discussed in the following chapters.

CHAPTER III

MAGNETOCONDUCTIVITY OF ALUMINUM

A. Introduction

In this chapter, we examine the field dependence and anisotropy of the magnetoconductivity and magnetoresistivity tensor components of single-crystal aluminum calculated by the path-integral over a nearly-free-electron Fermi surface, assuming a uniform relaxation time. These calculations were motivated by induced torque measurements that showed reproducible induced torque minima in the low-temperature, high-field limit for the magnetic field at <100> and <111> directions (Holroyd *et al* 1973). These minima persisted in samples that had been strained by up to 8%, and for temperatures from 1.2 to 25 K. The minima disappeared gradually as the temperature was increased above 25 K, because the increasing phonon scattering slowly removed the sample from the high-field regime. The small changes in resistivity with strain and temperature indicated to us that the scattering was impurity dominated in the samples of nominal 5-9's purity, and hence likely close to the catastrophic ideal of the relaxation time approximation.

The contribution of the Fermi surface geometry to this persistent anisotropy was considered to be of sufficient im-

portance to merit detailed path-integral calculations, using a simplified Fermi surface model and a uniform relaxation time. The path-integral method, as discussed in Chapter II, admits the inclusion of the effects of Fermi surface topology, and has provided the basis for the qualitative understanding of the galvanomagnetic properties of many metals. Since the aluminum Fermi surface is free-electron-like, these calculations used the single-orthogonalized-plane-wave (single-OPW) second-band hole surface and disconnected toroidal composites of the third and fourth band single-OPW electron pieces. This Fermi surface accounts for the effects of Bragg reflection.

Essentially these same assumptions were used by Feder and Lothe (1965) in their calculation of the magnetoresistivity tensor of aluminum with the magnetic field along <100>, although they neglected the very small fourth band single-OPW electron pockets rather than including them in a composite electron band. They solved the Boltzmann transport equations by modifying the free electron uniform relaxation time solution to be continuous for Bragg reflections.

The path-integral method permits the straightforward inclusion of the effects of magnetic breakdown, relaxation time anisotropy, and a more accurate Fermi surface. The extensions to the simplest theory are discussed separately in Chapter VI because the simple theory reproduced our induced torque data with only small systematic deviations.

In particular our induced torque data, in fields up to 18 kOe, show no evidence of the open orbits which magnetic breakdown would induce.

In this chapter we present the results of these detailed simple calculations for aluminum, and some general insights which may prove useful in understanding the galvanomagnetic properties of metals.

The single-OPW Fermi surface of aluminum consists of a second-band hole surface and electron pieces in the third and fourth bands as is shown in Fig. 1. The hole surface (Fig. 1-b) is very similar to that determined by Ashcroft (1963) by a four-OPW calculation, except for the rounding of the sharp cusps that are evident in the single-OPW model.

We have modified the single-OPW electron pieces (Fig. 1-c) into disconnected toroidal composites equal in volume to the single-OPW third and fourth band electron pieces. This composite has the form of Ashcroft's electron surface (Fig. 1-d) although the shapes of the arms differ somewhat. The arcs of the modified single-OPW Fermi surface are large and few in number. Each arc terminates in a Bragg reflection which generally changes the parameters v_z and $v_\perp$ from arc to arc. These abrupt and often large changes have significance for the low-field dependences of the conductivity and resistivity components, as well as the high-field dependences.

In the numerical evaluation of the path-integrals

for each orbit, considerable care had to be taken to ensure that the arcs were traversed in the correct order and that the resulting orbits were in fact closed, since even one orbit (of the some 200-300 orbits which had to be evaluated for each field orientation) with an artificial open orbit character would vitiate the high-field calculations.

To evaluate each conductivity component, the k_z integration was carried out for each conductivity component using the adaptive algorithm described in Chapter II. For each crystallographic orientation, the conductivity tensor divided by τ was evaluated for values of $\omega\tau$ over a range of almost 4 decades, from 0.02 to 100. The $\omega\tau$ values were logarithmically distributed to permit accurate interpolations to be made in each field regime, so that from these computed values $\sigma_{ij}(H)$ could be simply determined given a value for τ.

The $\omega\tau$ (recall that $\omega\tau=\omega^*\tau^*$) dependence of the conductivity components for selected field directions are shown in log-log plots in Fig. 6, where the conductivity is scaled by τ^{-1}. The resistivity tensor was obtained for each $\omega\tau$ value by inverting the corresponding conductivity matrix. The resulting $\omega\tau$ dependences of the resistivity tensor components, scaled by τ, are plotted in log-log graphs in Fig. 7. The field dependences of the index transposes of the plotted components may be inferred from the Onsager relations $\sigma_{ij}(H) = \sigma_{ji}(-H)$ and $\rho_{ij}(H) = \rho_{ji}(-H)$. Note that those components which change sign are plotted as their absolute value.

Figure 6. The computed path-integral magneto-conductivity as a function of $\omega\tau$ for aluminum with the field (z axis) in selected directions:

A: z along [100] y along [001]

B: z 0.1° from [100] towards [110], y along [001]

C: z 20° from [100] towards [110], y along [001]

D: z along [110], y along [001]

E: z 25° from $[1\bar{1}1]$ towards [110], y along $[\bar{1}12]$

F: z 50° from $[1\bar{1}1]$ towards [110], y along $[\bar{1}12]$.

Note the absolute value signs for the off-diagonal terms, and the changes in sign which vertical asymptotes indicate. The conductivity is scaled by $\frac{1}{\tau}$ to make these graphs completely general.

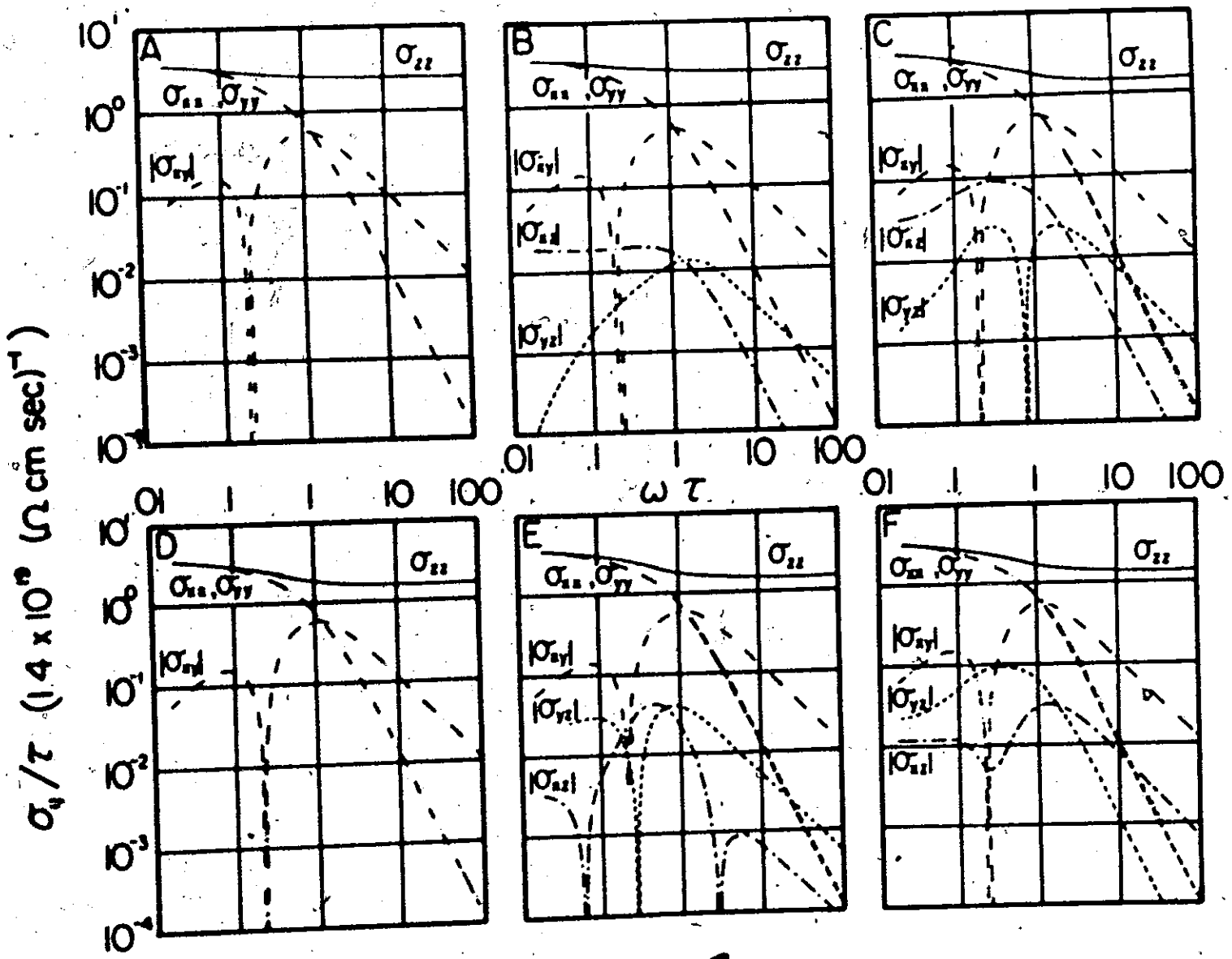
A
B
C
D
E
F
σ_{zz}
σ_{xx}, σ_{yy}
$|\sigma_{xy}|$
$|\sigma_{xz}|$
$|\sigma_{yz}|$
σ_q/τ $(14 \times 10^{10}\ \Omega\,\mathrm{cm\ sec})^{-1}$
10^{1}
10^{0}
10^{-1}
10^{-2}
10^{-3}
10^{-4}
.01
.1
1
10
100
$\omega\tau$

Figure 7. The computed path-integral magnetoresistivity of aluminum as a function of $\omega\tau$ with the field (z axis) in selected directions, (the same as Fig. 6):

A: z along [100] y along [001]

B: z 0.1° from [100] towards [110], y along [001]

C: z 20° from [100] towards [110], y along [001]

D: z along [110], y along [001]

E: z 25° from [1$\bar{1}$1] towards [110], y along [$\bar{1}$12]

F: z 50° from [1$\bar{1}$1] towards [110], y along [$\bar{1}$12]

Note the absolute value signs for the off-diagonal terms. The resistivity is scaled by τ to make these graphs completely general.

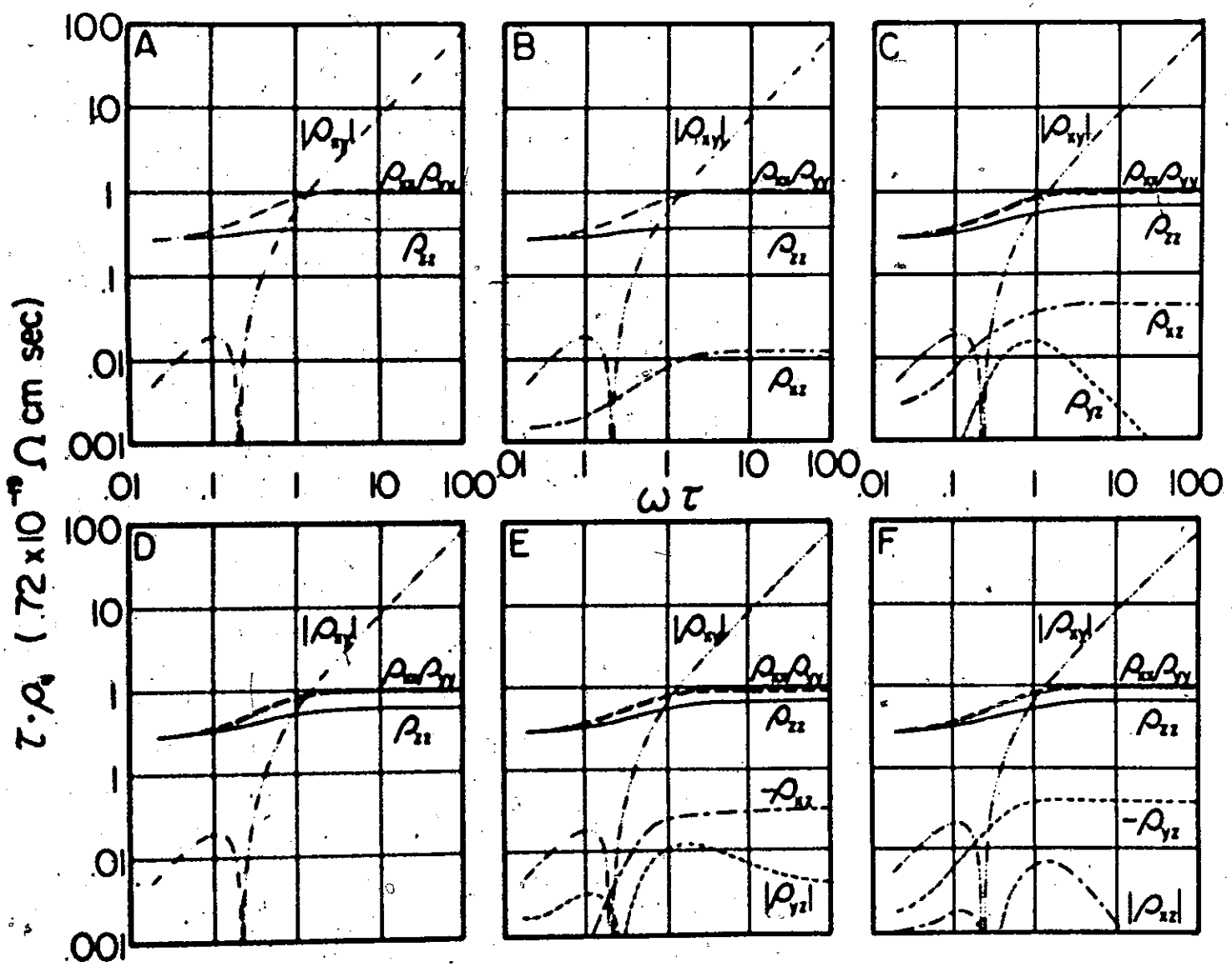
A
B
C
D
E
F
100
10
1
.1
.01
.001
.01
.1
1
10
100
$\omega\tau$
$\tau \cdot \rho_0$ ($.72 \times 10^{-6}$ Ω cm sec)
$|\rho_{xy}|$
ρ_{xx}/ρ_{yy}
ρ_{zz}
ρ_{xz}
ρ_{yz}
$-\rho_{xz}$
$-\rho_{yz}$
$|\rho_{yz}|$
$|\rho_{xz}|$

B. Calculated Galvanomagnetic Properties

In this section we separately summarize the properties of the Hall, transverse, longitudinal and longitudinal-transverse magnetoconductivity and magnetoresistivity components of aluminum as calculated by the uniform relaxation time path integral over the nearly free electron Fermi surface. The calculated field dependence and anisotropy of each component, as calculated for fields in the (100), (110) and (112) planes, are explicitly discussed.

B.1 Hall Terms

The calculated field dependence of the Hall conductivity, σ_{xy}, scaled by τ^{-1}, is shown by the solid line in Fig. 8 for magnetic fields along the <100> and <111> directions. The contributions of the second band holes and third band electrons are indicated separately by the dotted and dashed lines respectively. The hole and electron pieces contribute to σ_{xy} with opposite sign; and the electron contribution reaches the $(\omega\tau)^{-1}$, high-field regime at lower fields than does the hole contribution. Thus the Hall conductivity changes sign at a field value which depends on the k_z distribution of $\omega_c\tau$ for both bands. The approximate extrema of the calculated Hall anisotropy at intermediate fields occur at the <100> and <111> directions. Fig. 8 shows the field dependence of σ_{xy} for these directions.

In a particular field direction, at any given field,

Figure 8. The Hall conductivity of Al as a function of $\omega\tau$ for a field direction (a) along <100> and (b) along <111> directions showing the contributions of the holes (dotted curves) and electrons (dashed curves) separately, as well as the total Hall conductivity (solid curves).

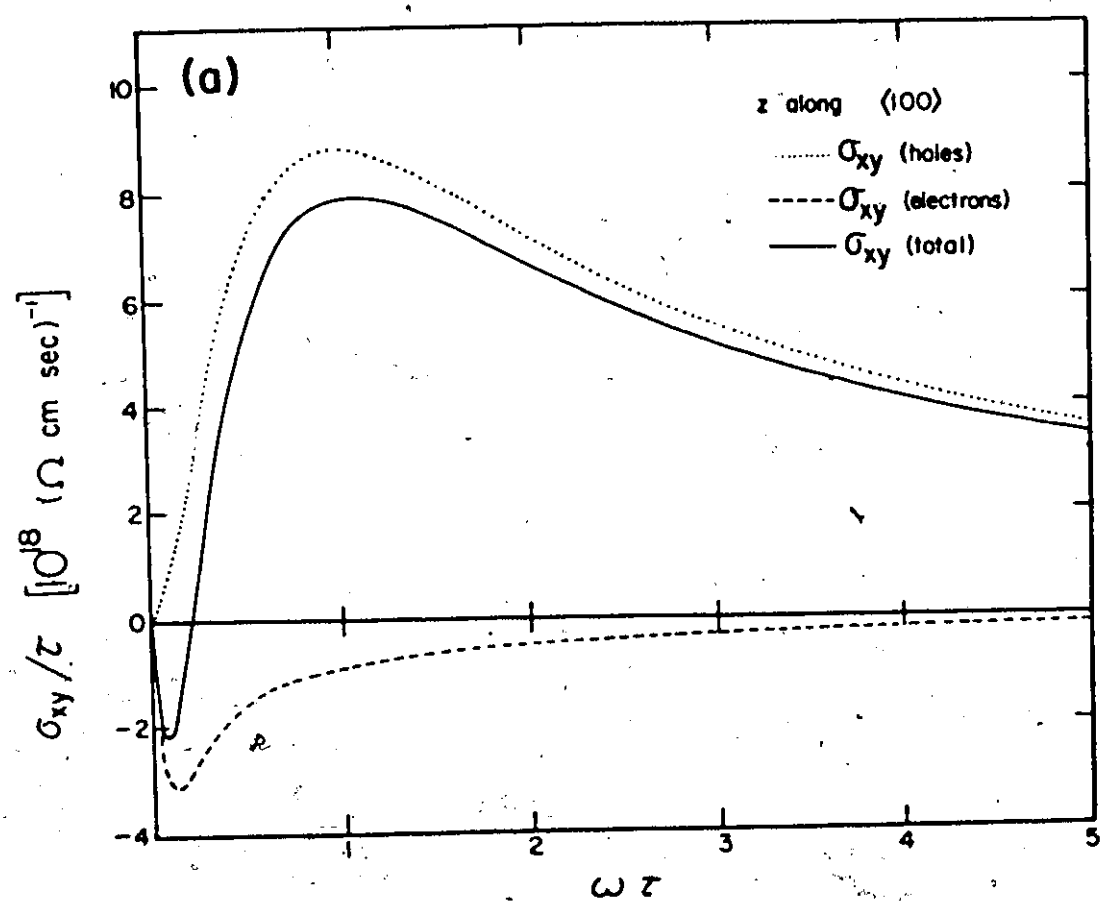
(a)
z along ⟨100⟩
σxy (holes)
σxy (electrons)
σxy (total)
σxy/τ [10^18 (Ω cm sec)^-1]
ωτ
10
8
6
4
2
0
-2
-4
1
2
3
4
5

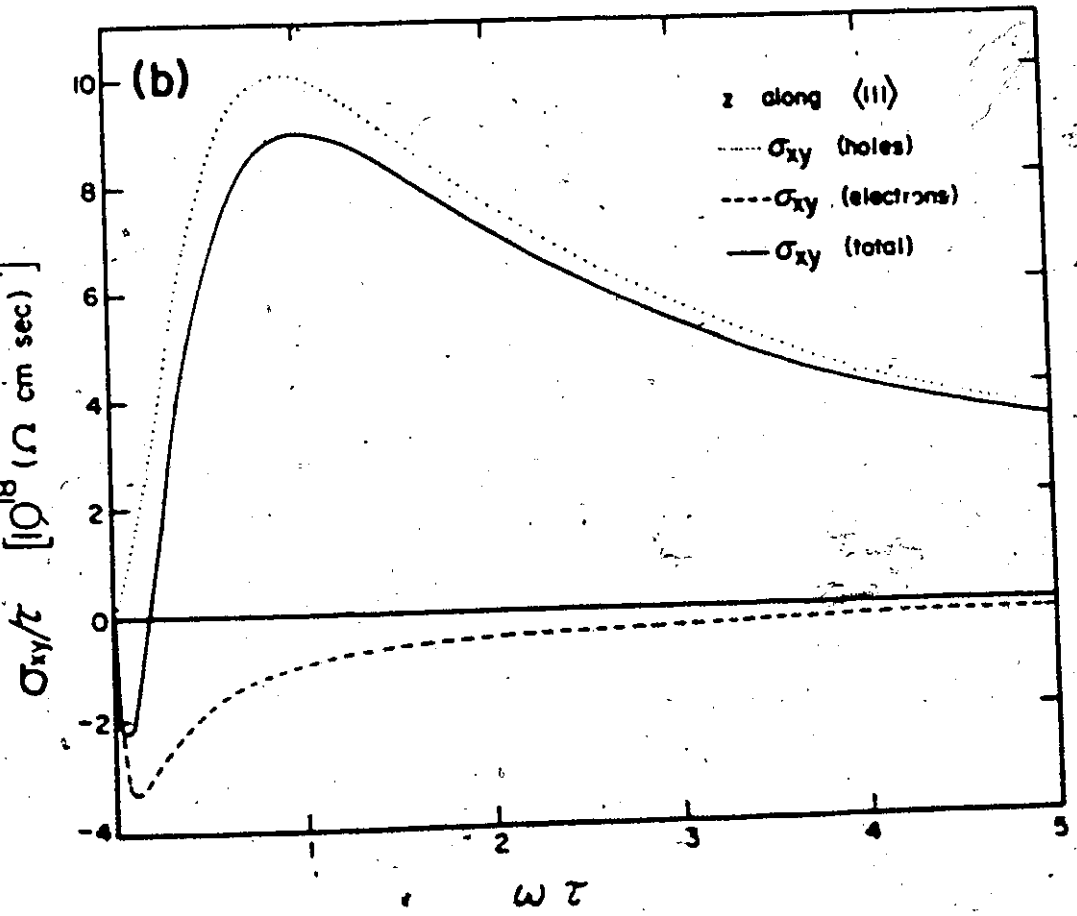
(b)
z along ⟨111⟩
σxy (holes)
σxy (electrons)
σxy (total)
σxy/τ [10^18 (Ω cm sec)^-1]
ωτ
10
8
6
4
2
0
-2
-4
1
2
3
4
5

it is always possible to find coordinates u, v, generated from x and y respectively by a proper rotation around z (the field direction) such that $\sigma_{uv} = -\sigma_{vu}$. This means that the even-field Hall term can be set to zero (from the Onsager relations: $\sigma_{xy}(H) = \sigma_{yx}(-H)$) at any specified field by such a coordinate rotation. It does not mean that a single coordinate system will have $\sigma_{uv}(H) = -\sigma_{vu}(H)$ for <u>all</u> fields. Using the general path-integral formula, it may be shown that when z is in a mirror plane, and we constrain u (or v) to be in this mirror plain also, then for all fields, $\sigma_{uv}(H) = -\sigma_{vu}(H)$, if there are no open orbits. Thus for z in the (100) and (110) planes, with y along [001] and [110] respectively, the calculated Hall terms are odd in field, while in the (112) plane, with y along [112], there is also a Hall term component which is even in field. Since there are no open orbits, these even-field components do not affect the high-field limit of the Hall coefficient. In the low-field region, our calculations indicate that σ_{xy} may differ from $-\sigma_{yx}$ by up to 15% for fields in the (112) plane and with y along [112].

The Hall coefficient of resistivity, $A_H (\equiv \rho_{yx}/H)$, was obtained from the inversion of the conductivity tensor. The field dependences of A_H for magnetic fields in <100> and <111> directions are shown in Fig. 9. In the low-field limit, few carriers encounter a Bragg reflection in a mean free path, and so the low-field Hall coefficient corresponds very

Figure 9. The Hall coefficient $A_H = \frac{\rho_{yx}}{H}$, of aluminum as a function of $\omega\tau$ for a magnetic field along <100> and <111> directions, calculated using the uniform relaxation time path-integral over our modified single-OPW Fermi surface. The two field orientations show the approximate extremes of the A_H anisotropy in the intermediate field region. A_H rises from the value nearly corresponding to the free-electron carrier density (n) of three electrons per atom in the low-field limit to one hole per atom in the high-field limit.

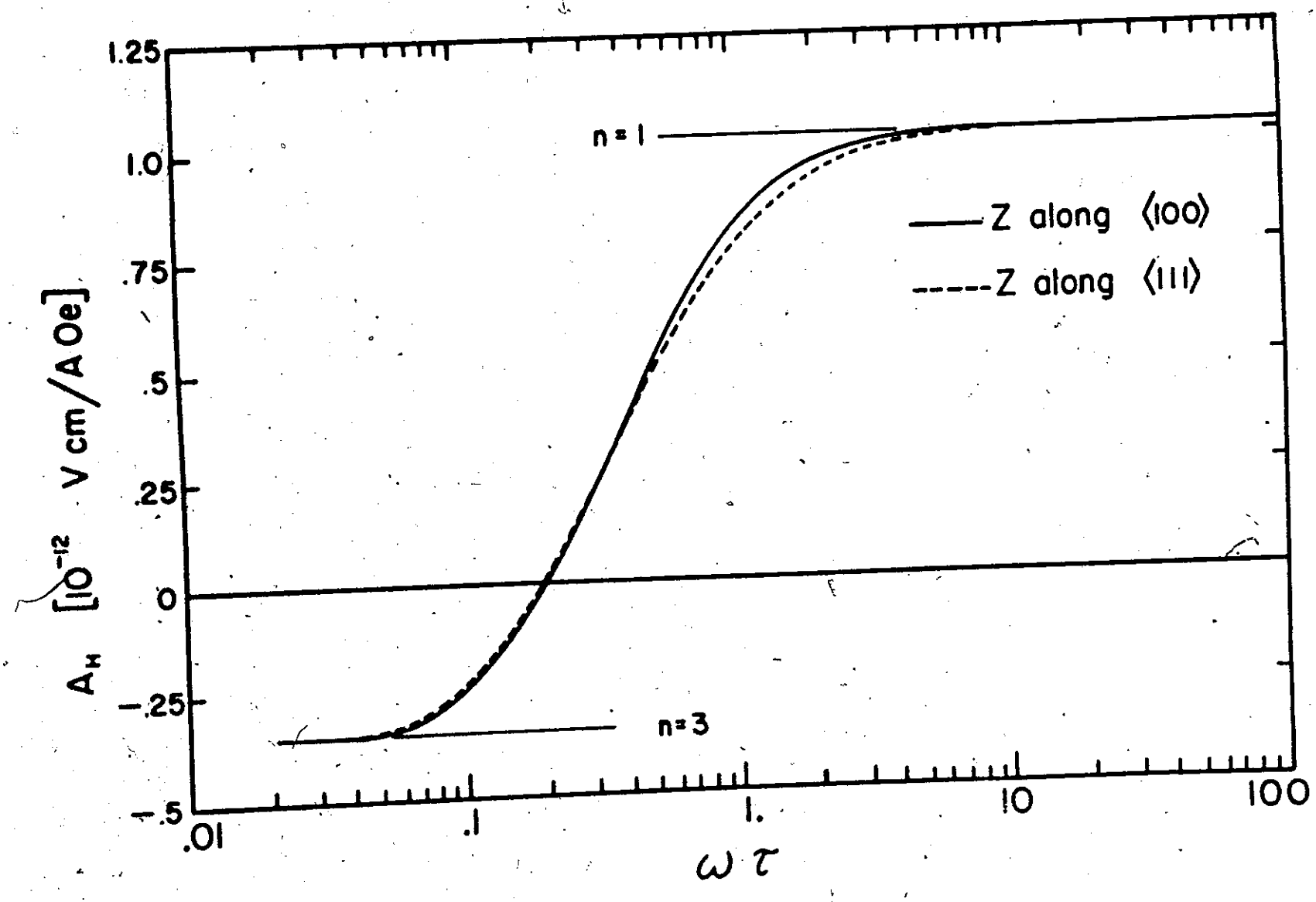
1.25
1.0
.75
.5
.25
0
−.25
−.5
A_H [10^{-12} V cm/A Oe]
n = 1
n = 3
Z along ⟨100⟩
Z along ⟨111⟩
.01
.1
1.
10
100
$\omega\tau$

Figure 10. The anisotropy of the Hall coefficient of aluminum, calculated for fields in the (011), (001) and ($\bar{1}$12) planes for different $\omega\tau$ values. The x-z plane is a mirror plane for the (011) and (001) planes with y along [011] and [001] respectively, so $\rho_{yx} = -\rho_{xy}$. This is not the case in the ($\bar{1}$12) plane so both ρ_{yx}/H and $-\rho_{xy}/H$ are plotted for the ($\bar{1}$12) plane.

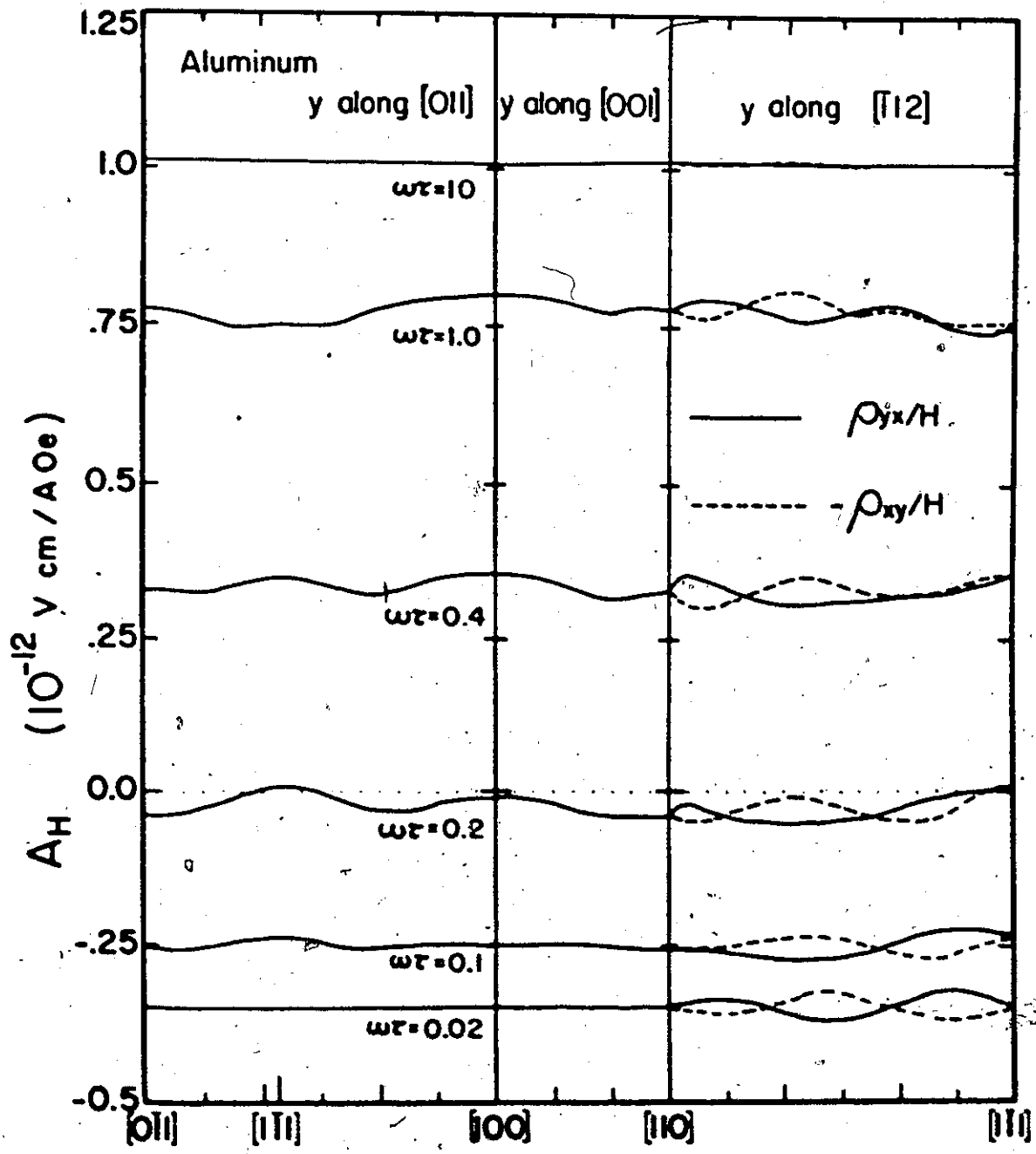
Aluminum
y along [011]
y along [001]
y along [112]
ωτ=10
ωτ=1.0
ωτ=0.4
ωτ=0.2
ωτ=0.1
ωτ=0.02
ρyx/H
ρxy/H
A_H (10^-12 V cm / A Oe)
1.25
1.0
.75
0.5
.25
0.0
-.25
-0.5
[011]
[1̄11]
[100]
[110]
[111]

nearly to three electrons per atom, if the even-field Hall terms are zero, or are cancelled by considering only the odd-field Hall coefficient, $A_H' = \frac{\rho_{yx}-\rho_{xy}}{2H}$. The anisotropy of A_H (as well as that of ρ_{xy}/H, for the (112) plane) is shown for selected values of $\omega\tau$ in Fig. 10. At $\omega\tau = 0.02$, the calculated A_H' corresponds to some 3% less than the expected free electron value of 3 electrons per atom. The difference between A_H and A_H', which is up to 7% at $\omega\tau = 0.02$, decreases as the field is increased; and in the high-field limit, the implied carrier concentration changes to one hole per atom on the basis of the nearly free electron Fermi surface volumes and is isotropic to within 1% in our calculations. It is also interesting to note that even at $\omega\tau = 10$, A_H is some 2% less than $1/H\sigma_{yx}$ due to the contribution of the transverse conductivity in the matrix inversion.

B.2 Transverse Terms

The transverse components, σ_{xx} and σ_{yy}, vary from σ_o in the low-field limit to a H^{-2} field dependence in the high-field region as seen in Fig. 3. The low-field asymptote of σ_{ii}/τ is 5.12×10^{19} $(\Omega\text{-cm-sec})^{-1}$ and is the same (within 3%) as that calculated from the zero-field conductivity, σ_o, using $\sigma_o/\tau = ne^2/m_o$ where n is the carrier density. The H^{-2} high field dependence is expected for any metal with no open orbits using the relaxation time approximation (Lifshitz et al, 1956-a).

The calculated field dependence of the transverse

magnetoresistances, $(\rho_{xx}-\rho_o)/\rho_o$ and $(\rho_{yy}-\rho_o)/\rho_o$, are shown in Fig. 11 by the dotted and dashed curves respectively. These magnetoresistances are shown at four selected field orientations. In each case there is a low-field linear magnetoresistance which originates with the artificially sharp cusps of the model Fermi surface, and the resultant discontinuities in $v(\theta)$ at Bragg reflections. These discontinuities make the usual (Ziman, 1964, p. 259) low-field Taylor expansion of eq. 7 inapplicable, and change the generally predicted low-field H^2 dependence to a linear dependence. This property of the low-field magnetoresistance can be used as a crude probe of the sharpness of Bragg reflections in nearly-free electron metals (Pippard 1964).

In the intermediate field region, the calculated transverse magnetoresistance rises towards a high-field saturation value (as expected for uncompensated metals with no open orbits) reaching within 1% of the saturation value by $\omega\tau = 6$. The anisotropies of the saturation transverse magnetoresistance is shown in Fig. 12 for field directions in the (100), (110) and (112) planes, and with y along [100], [110] and [112] respectively. These anisotropies arise from the anisotropy of the high-field transverse conductivities which is generated by the variation of the orbitally averaged mean of $v_x(\theta)$ and $v_y(\theta)$ times their second moments.

Alternatively, it is possible to discuss the high-field transverse magnetoresistance anisotropy in terms of

Figure 11. The magnetoresistance as a function of $\omega\tau$ for aluminum, calculated using the uniform relaxation time path integral over our modified single-OPW Fermi surface. The three magnetoresistance components $\frac{\rho_{xx}-\rho_o}{\rho_o}$, $\frac{\rho_{yy}-\rho_o}{\rho_o}$ and $\frac{\rho_{zz}-\rho_o}{\rho_o}$ are shown by the dotted, dashed and solid curves respectively. In Figure 11-a, the magnetoresistance is shown for the field along [110] and y along [001]; and for the field along $[1\bar{1}1]$ with y along $[\bar{1}12]$. In Figure 11-b, y is along [001]; and the transverse magnetoresistance components are plotted for z along [100] and z 25° from [100] towards [110]. The longitudinal magnetoresistance is plotted for z along [100] and at 5°, 10°, 15°, 20° and 25° from [100] towards [110].

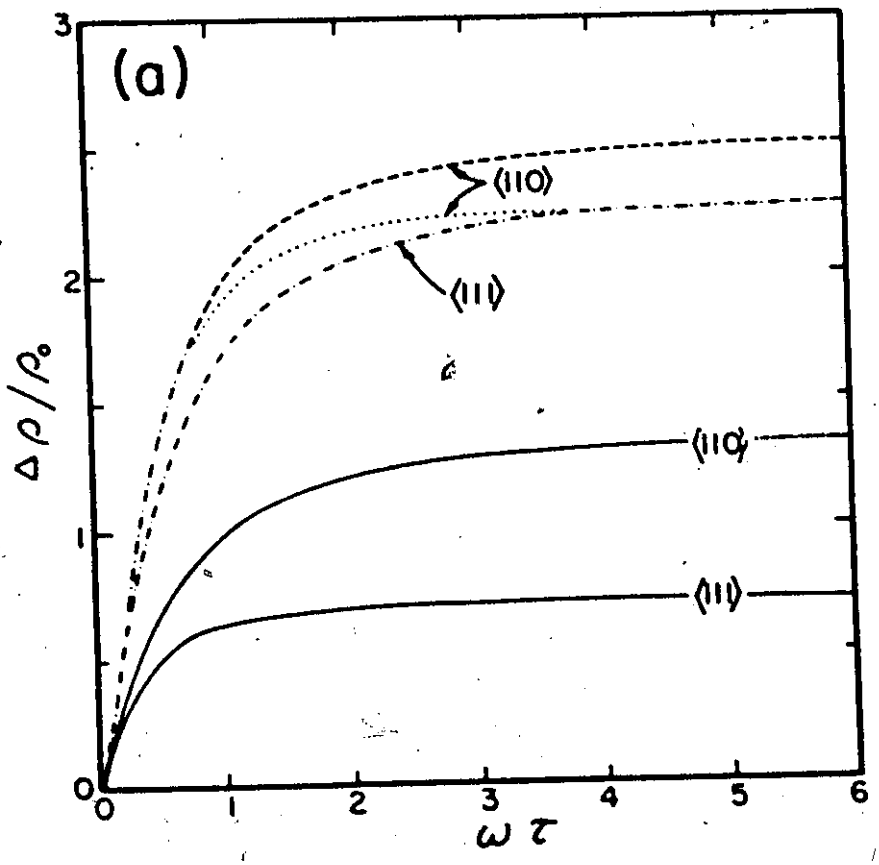
(a)
⟨110⟩
⟨111⟩
⟨110⟩
⟨111⟩
Δρ/ρ₀
ωτ
0
1
2
3
4
5
6

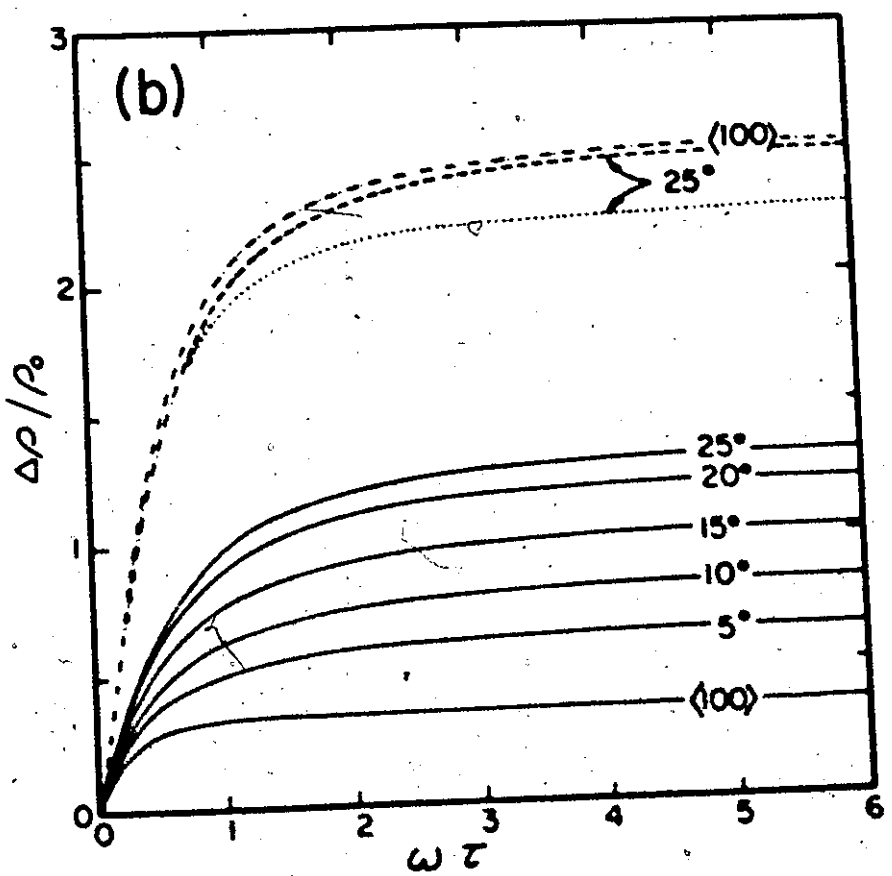
(b)
⟨100⟩
25°
25°
20°
15°
10°
5°
⟨100⟩
Δρ/ρ₀
ωτ
0
1
2
3
4
5
6

Figure 12. The anisotropy of the saturation (high-field) value of the three magnetoresistance components for fields in the (011), (001) and ($\bar{1}$12) planes. The lower solid curve is the saturation longitudinal magnetoresistance. The upper solid curve is the saturation transverse magnetoresistance, $\frac{\rho_{yy}-\rho_o}{\rho_o}$, which is to be compared with experimental magnetoresistance rotation diagrams for the current along [011], [001] and [$\bar{1}$12] directions, for fields rotated in the (011), (001) and ($\bar{1}$12) planes respectively. For completeness, the other saturation magnetoresistance component, $\frac{\rho_{xx}-\rho_o}{\rho_o}$, is shown by the dashed curve.

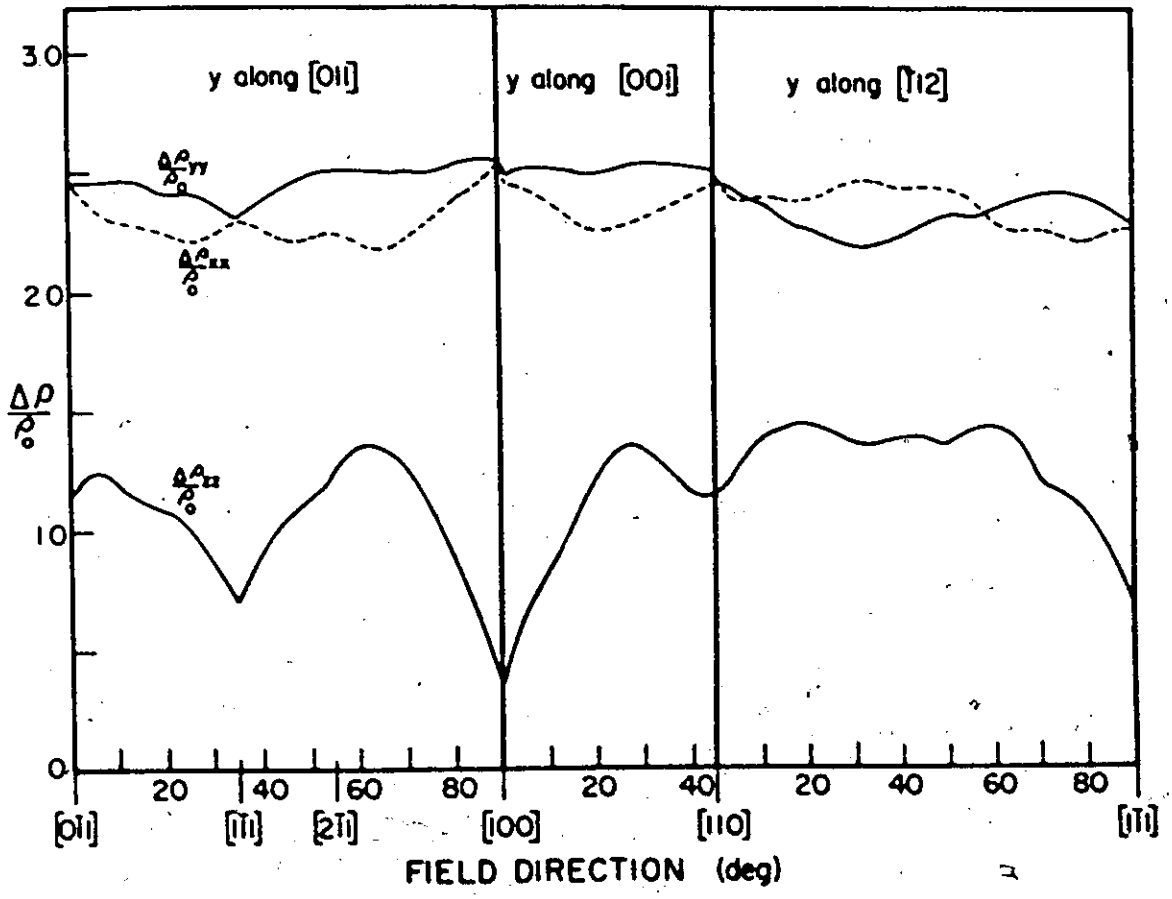
y along [011]
y along [001]
y along [$\bar{1}$12]
$\frac{\Delta\rho_{yy}}{\rho_0}$
$\frac{\Delta\rho_{xx}}{\rho_0}$
$\frac{\Delta\rho_{zz}}{\rho_0}$
$\frac{\Delta\rho}{\rho_0}$
3.0
2.0
1.0
0
20
40
60
80
20
40
20
40
60
80
[01$\bar{1}$]
[$\bar{1}$1$\bar{1}$]
[2$\bar{1}$1]
[100]
[110]
[1$\bar{1}$1]
FIELD DIRECTION (deg)

a simple geometric integral. The high-field transverse magnetoresistance of uncompensated metals with no open orbits depends on the k_z integral of $<(k_x-\bar{k}_x)^2>$ for ρ_{xx} and $<(k_y-\bar{k}_y)^2>$ for ρ_{yy} where $\bar{k}_x$ and $\bar{k}_y$ are the reciprocal space coordinates of each orbit's centroid, and the angular brackets denote an orbital integral (Wagner, 1972). Since the central orbits for all field directions in the xz plane share a common k_y, the asymmetry of ρ_{yy} (the component measured in 4-probe measurements) is expected to be somewhat smaller than the asymmetry of ρ_{xx} which has no common k_x value for the different field directions, and this may be seen in the (001) and (011) planes in Fig. 12. This central band of orbits on the second band hole surface, with their partial correlation in k_y, are large orbits and so contribute significantly to σ_{xx} and hence to ρ_{yy}. There is also an approximate inverse correlation between ρ_{xx} and ρ_{zz} which may be seen in Fig. 12. The tendency of ρ_{xx} to rise as ρ_{zz} falls originates with the constancy of $v_x^2 + v_z^2$ for each point on the Fermi surface for a fixed direction of y in the crystal.

B.3 Longitudinal Term

The computed longitudinal magnetoconductivity in aluminum decreases from the low-field limit of σ_o to a smaller, high field value which is highly anisotropic, as may be seen in Fig.13. This gives rise to large anisotropy in the intermediate and high-field magnetoresistivity which is shown in

Figure 13. A log-log plot of the longitudinal conductivity contributions versus $\omega\tau$ for various orbits on the second band hole surface, with the field along <111>. The extremal orbit at $k_z = 0$ (dashed orbit on the Fermi surface) has an $(\omega\tau)^{-2}$ field dependence in the high-field limit.

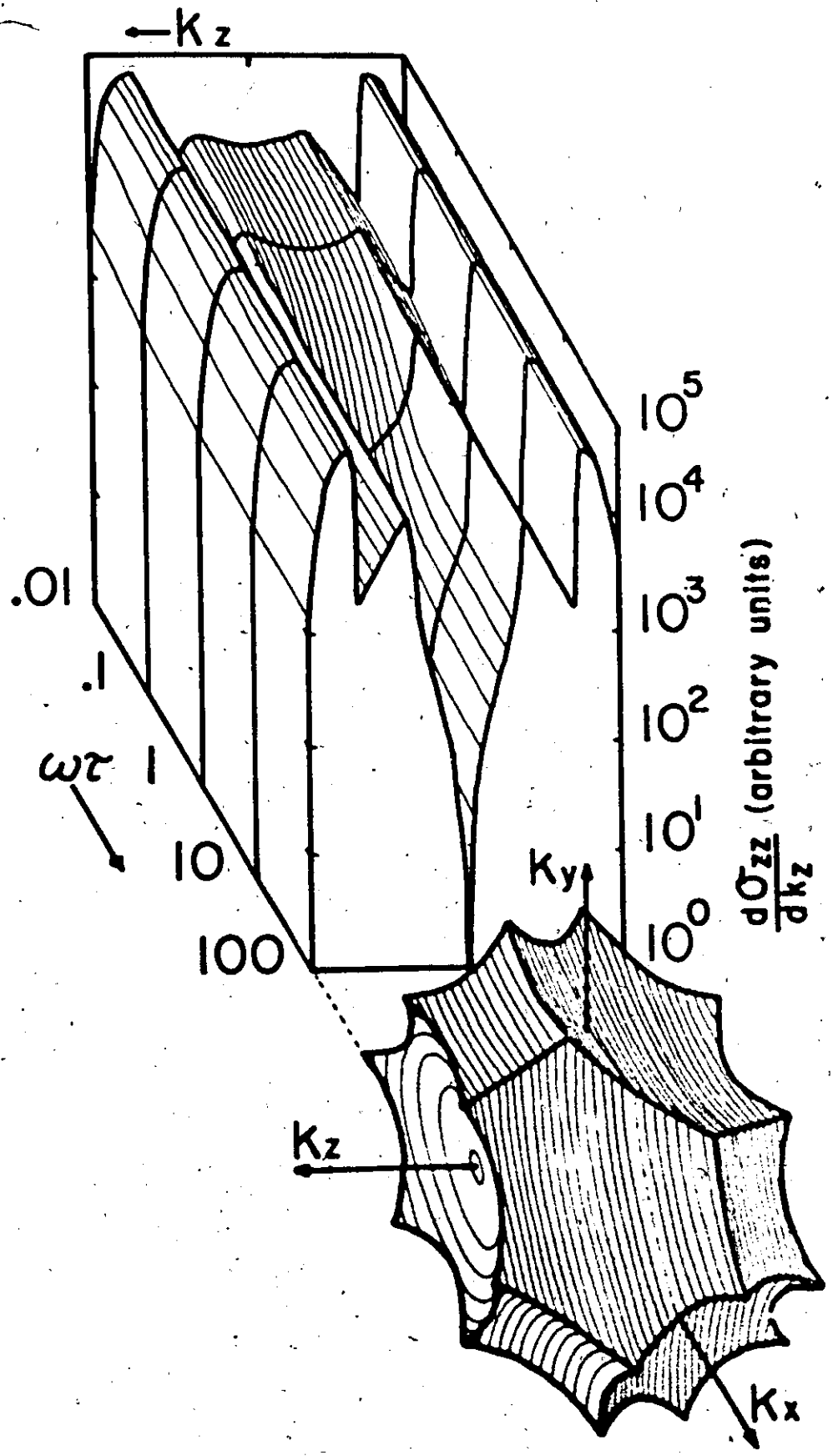
K_z
$\omega\tau$
.01
.1
1
10
100
10^5
10^4
10^3
10^2
10^1
10^0
$\frac{d\sigma_{zz}}{dk_z}$ (arbitrary units)
K_y
K_z
K_x

Fig. 7. The field dependence of the calculated longitudinal magnetoresistance $(\rho_{zz}-\rho_o)/\rho_o$ is shown in Fig. 11 by the solid curves, for several field orientations. There is a low-field linear magnetoresistance for the same reason as was discussed above for the transverse magnetoresistance. The anisotropy of the saturation longitudinal magnetoresistance is shown in Fig. 12 by the lower solid line, for magnetic fields in the (100), (110) and (112) planes. The higher the symmetry of the nearest symmetry direction of the magnetic field, the more rapidly the longitudinal magnetoresistance saturates and the lower that saturation value is.

The origin of this large high-field anisotropy is the variation with magnetic field direction of the mean of $\langle v_z \rangle$, the orbital average of $v_z(\theta)$. When $\langle v_z \rangle$ is zero for a particular orbit (as it is for extremal orbits), the longitudinal differential conductivity of that orbit will have a H^{-2} field dependence in the high field limit. This dependence is just the same as that of the transverse differential conductivities for closed orbits ($\langle v_x \rangle = \langle v_y \rangle = 0$). In general $\langle v_z \rangle$ for an orbit is non-zero and in this case the orbit's longitudinal differential conductivity will have the same field dependence as that of a transverse term with an open orbit. If $\langle v_z \rangle^2$ is small compared to $\langle v_z^2 \rangle$, σ_{zz} for this orbit may still have a H^{-2} region over a limited field range but in this case σ_{zz} will be asymptotically bounded above on the low-field side, and on the high-field side will be bounded below. The

ratio of these asymptotes will depend on the ratio $\langle v_z^2 \rangle$ to $\langle v_z \rangle^2$.

Free-electron like orbits (such as limit point orbits) will exhibit no variation in their differential longitudinal conductivity with field. Each of these three types of behaviour may be seen in Fig. 13, where the logarithms of $\frac{d\sigma_{zz}}{dk_z}$ and $\omega\tau$ are plotted as function of k_z for the second band hole surface, with the field in a <111> direction. The dotted line in Fig. 2 shows the differential longitudinal conductivity vs k_z for the second band hole surface at $\omega\tau = 100$. Note that there is a rather broad band of orbits around the central orbit which are contributing very little to σ_{zz}. The orbits which terminate in the limit point orbit contribute much more to σ_{zz}.

The actual value of the high-field saturation longitudinal magnetoresistance for a particular field direction depends on the degree of v_z orbital cancellation for the whole set of cyclotron orbits. The major effect of the crystal potential in real space is to Bragg reflect the carriers, changing the high-field helical spirals of a free electron gas (with no longitudinal magnetoresistance) to a set of helical arcs of varying pitch, with the average pitch less than for the free electron spirals. This reduces the z component of the mean free path at high fields as compared to the low-field mean free path, generating the longitudinal magnetoresistance. For higher symmetry field orientations,

more order is imposed on the orbital systematics of the $v_z(\theta)$'s of aluminum than for field directions far from symmetry. The higher the symmetry, the smaller the v_z cancellation and the saturation longitudinal magnetoresistance is expected to be smaller.

For z along [001] (refer to Fig. 1(b) and 1(c)), we can see that there is little cancellation of v_z for orbits on the single OPW hole surface. On the single-OPW hole surface in this direction the central band of extremal orbits which contribute nothing to the high-field σ_{zz} is vanishingly narrow, and the sharp cusp at the central orbit is an artificial feature. This point is discussed further in Chapter VI, in the section on the four-OPW calculations. For the [001] orientation, some 78% of the high-field longitudinal magnetoconductivity arises from the carriers on the hole surface, some 19% from the electrons on the electron toroid whose axis is along [001] and some 1.5% each is contributed by the two remaining toroids, which support only orbits with large v_z cancellation. The corresponding contributions to the low-field conductivity are ~~75%,~~ 17% and 4%. The electron orbits have small cyclotron masses and so reach the "high-field condition" at smaller values of $\omega\tau$ than the average hole orbit. Here the "high field condition" refers to a field region where the longitudinal magnetoconductivity of a particular orbit has either saturated or has become negligible

with respect to the total σ_{zz}. That is, a region where the field dependence of the contribution of a particular orbit to σ_{zz} is not affecting the field dependence of σ_{zz}. Even the large orbits on the second-band hole surface will reach this high-field condition at an $\omega\tau$ value that is four times smaller than might be naively thought, since the four-fold symmetry has reduced the periodicity of v_z by a factor of four, and it is this periodicity rather than the orbital periodicity that controls the field dependence of the contribution to σ_{zz}. Similarly, for z along other symmetry directions, we expect saturation of σ_{zz} to be more rapid than for z along crystallographic directions far from symmetry. The higher the symmetry of the field direction, the more rapid the saturation will tend to be. This tendency is somewhat complicated by the variation of the cyclotron frequencies of all orbits as the field orientation is changed, and by the fact that not all orbits around an n-fold symmetric axis have n-fold symmetry (e.g. most electron orbits for z along <001>).

These two observations on the role of symmetry in the saturation behaviour of σ_{zz} do not require exact symmetry to affect the orbital averages, and so we might expect the behaviour of σ_{zz} to vary slowly as we move away from the symmetry directions. That this is the case may be seen in Fig.11 and Fig.12.

B.4 Longitudinal-Transverse Terms

The longitudinal-transverse magnetoconductivity components (σ_{xz}, σ_{zx}, σ_{yz} and σ_{zy}) measure the tendency of an excitation of the electronic Fermi sea in a transverse (longitudinal) direction to propogate in a longitudinal (transverse) direction under the combined influence of the crystal potential and the magnetic field. That is, carriers are accelerated by the application of an electric field in, say, the x direction, and under the influence of the magnetic field and Bragg reflections, their path in real space will be such that in general there will be a net current component in the z direction. In general these terms have a H^{-1} field dependence in the high-field limit, for closed orbits. (With open orbits, the longitudinal-transverse magnetoconductivities can saturate at high fields.) With the magnetic field precisely along directions of two-fold or higher symmetry, the longitudinal-transverse terms are identically zero. Even slightly away from symmetry, our calculations show that this is not the case, as may be seen in Fig. 6(b) when the magnetic field is 0.1 degrees away from the four-fold [001] direction. If the x-z plane is a mirror plane, then by considering the path-integral expansion at high fields, for closed orbits it may be shown that the H^{-1} term of $\sigma_{xz}(\hat{H})$ must be zero. Thus in the (010) and ($\bar{1}$10) planes with y along [010] and [$\bar{1}$10] respectively, σ_{xz} and σ_{zx} (by the Onsager relation)

have H^{-2} dependences in the high-field limit. That this is a sufficient but not necessary condition for a H^{-2} dependence is illustrated in Fig. 6(f) where σ_{yz} has a H^{-2} field dependence up to $\omega\tau = 100$, although the y-z plane is far from a mirror plane. There has just been fortuitous cancellation of the H^{-1} contributions from the different orbits.

In the high-field regime, if σ_{xz} varies as H^{-2} and σ_{yz} varies as H^{-1}, then for an uncompensated metal such as aluminum, ρ_{yz} will vary as H^{-1} and ρ_{xz} will tend to a constant high-field value. If both σ_{xz} and σ_{yz} vary as H^{-1}, then both ρ_{xz} and ρ_{yz} will tend to a constant value which is up to 0.26 ρ_o. These types of behaviour are illustrated in Fig. 7.

The anisotropy of the saturation value of ρ_{xz} for fields in the (100), (110) and (112) planes is shown in Fig. 14 by the solid line, expressed as a fraction of the zero field resistivity ρ_o. The saturation value of ρ_{yz} is also shown in Fig. 14 for the (112) plane, the only non-mirror plane for which calculations were done; and so it is the only plane for which the calculated ρ_{yz} does not tend to zero in the high-field limit.

For each of the above cases, the behaviour of the index transpose of the σ_{ij} or ρ_{ij} longitudinal-transverse components may be inferred from the Onsager relation, $\sigma_{ij}(\vec{H}) = \sigma_{ji}(-\vec{H})$ and $\rho_{ij}(\vec{H}) = \rho_{ji}(-\vec{H})$, and the field dependence and sign of σ_{ji} and ρ_{ji}.

Figure 14. The calculated anisotropy of the high-field saturation value of the longitudinal-transverse resistivity of aluminum, for fields in the (011), (001) and ($\bar{1}$12) planes. Since the x-z plane is a mirror plane for y along [011] and along [001], ρ_{yz} tends to zero (as H^{-1}) in the high-field limit for these two planes. The ($\bar{1}$12) plane is not a mirror plane so that in that plane both ρ_{xz}/ρ_o and ρ_{yz}/ρ_o are plotted. In the high-field limit, where ρ_{xz} and/or ρ_{yz} saturate $\rho_{xz} = \rho_{zx}$ and/or $\rho_{yz} = \rho_{zy}$.

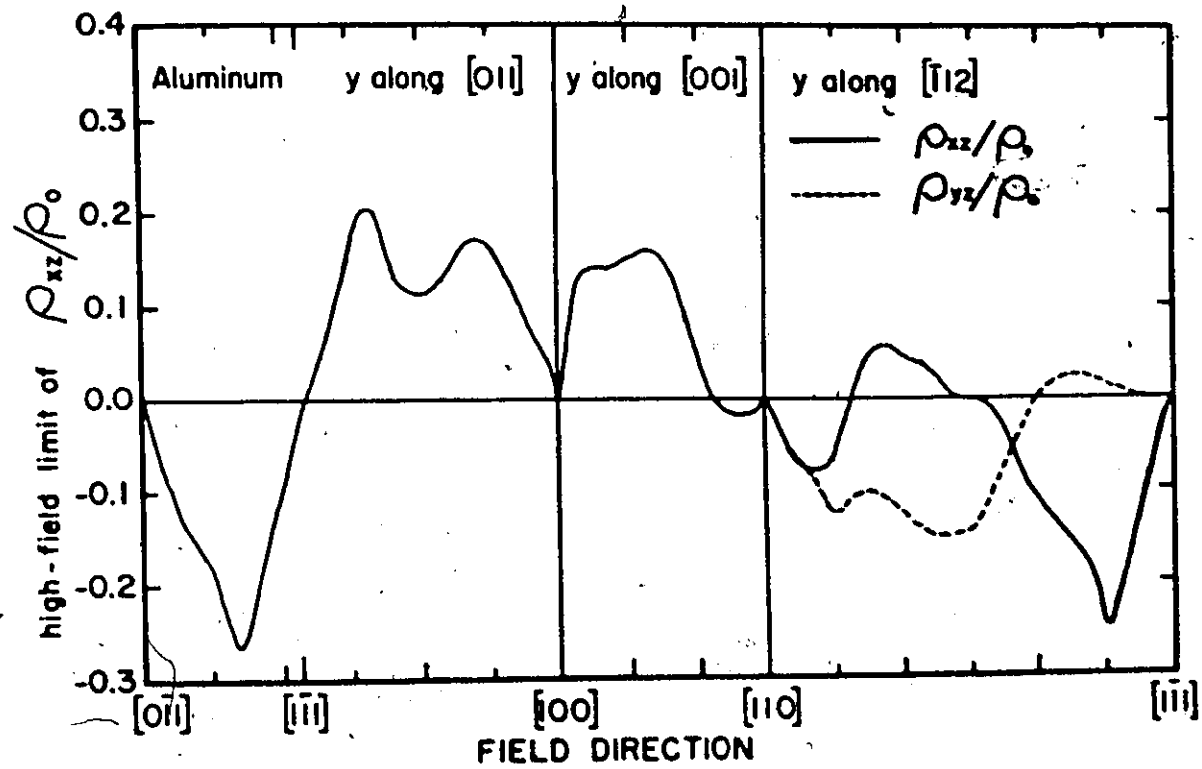
Aluminum
y along [011]
y along [001]
y along [$\bar{1}$12]
ρ_{xz}/ρ_o
ρ_{yz}/ρ_o
high-field limit of ρ_{xz}/ρ_o
0.4
0.3
0.2
0.1
0.0
-0.1
-0.2
-0.3
[01$\bar{1}$]
[1$\bar{1}$1]
[100]
[110]
[1$\bar{1}$1]
FIELD DIRECTION

It is also appropriate here to note the effects of neglecting the longitudinal-transverse conductivity components in the matrix inversion to obtain the resistivity tensor. In our aluminum calculations, these effects were found to be small for all magnetoresistivity components, at all fields and for all field directions investigated (that is, at 5° intervals in the (100), (110) and ($1\bar{1}2$) planes). The determinant of the conductivity matrix is altered by up to ±0.2% near $\omega\tau = 1$, with this discrepancy tending to zero in both the low-field and high-field limits. The error in the approximate determinant affects all the resistivity components, and is the only change in the longitudinal component. The approximate determinant affects the Hall terms most at intermediate fields, while neglecting the longitudinal-transverse terms in the Hall cofactors also changes the low-field Hall coefficient by up to 0.14% at $\omega\tau = 0.02$. The high-field saturation value of the transverse magnetoresistivity may be up to 0.8% too small if the longitudinal-transverse terms are neglected.

C. Comparison with Induced Torque Measurements

In this section we discuss the induced torque method and the agreement between our experiments and theory.

The induced torque technique for obtaining information on the galvanomagnetic properties of metals has proved to be a useful adjunct to conventional four-probe experiments. The

chief attractions of this technique are its leadless nature and the attendant ease with which it can probe the galvanomagnetic properties of a single sample with the magnetic field in any crystallographic orientation. In these experiments, a monocrystalline spherical sample is suspended from a nulling torque transducer in a magnetic field, which is rotating about the torque transducer axis with an angular velocity Ω. This induces eddy currents in the sample which in turn produce a retarding torque which is measured by the torque magnetometer. The torque is an involved, but exactly known, function of the resistivity tensor $\overleftrightarrow{\rho}$. If we define a rotating coordinate system such that $\vec{B} = B\hat{z}$ and $\vec{\Omega} = \Omega\hat{y}$, and assume that $\vec{B}$ is constant throughout the sample, then to first order in Ω, the induced torque is

$$N_y = \frac{4\pi R^5 \Omega B^2}{15c^2} \left[(\mathrm{tr}\overleftrightarrow{\rho})\, \overleftrightarrow{I} - \overleftrightarrow{\rho}^t \right]^{-1} \qquad [14]$$

where R is the sample radius (Visscher and Falicov, 1970). If the longitudinal-transverse terms are neglected, the explicit expression in terms of the resistivity components is

$$N_y = \frac{4\pi R^5 \Omega B^2}{15c^2} \; \frac{(\rho_{xx}+\rho_{zz})}{(\rho_{xx}+\rho_{zz})(\rho_{yy}+\rho_{zz})-\rho_{xy}\rho_{yx}} \qquad [15]$$

Neglecting the longitudinal-transverse magnetoconductivity elements decreases the calculated torque by up to 0.5%, so that although eq. [14] was used for the quantitative purposes,

Figure 15. Torque rotation diagrams in the (001) plane of aluminum at 1.5 K. For each magnetic field, except 20 kOe, the torque is shown for both directions of rotation.

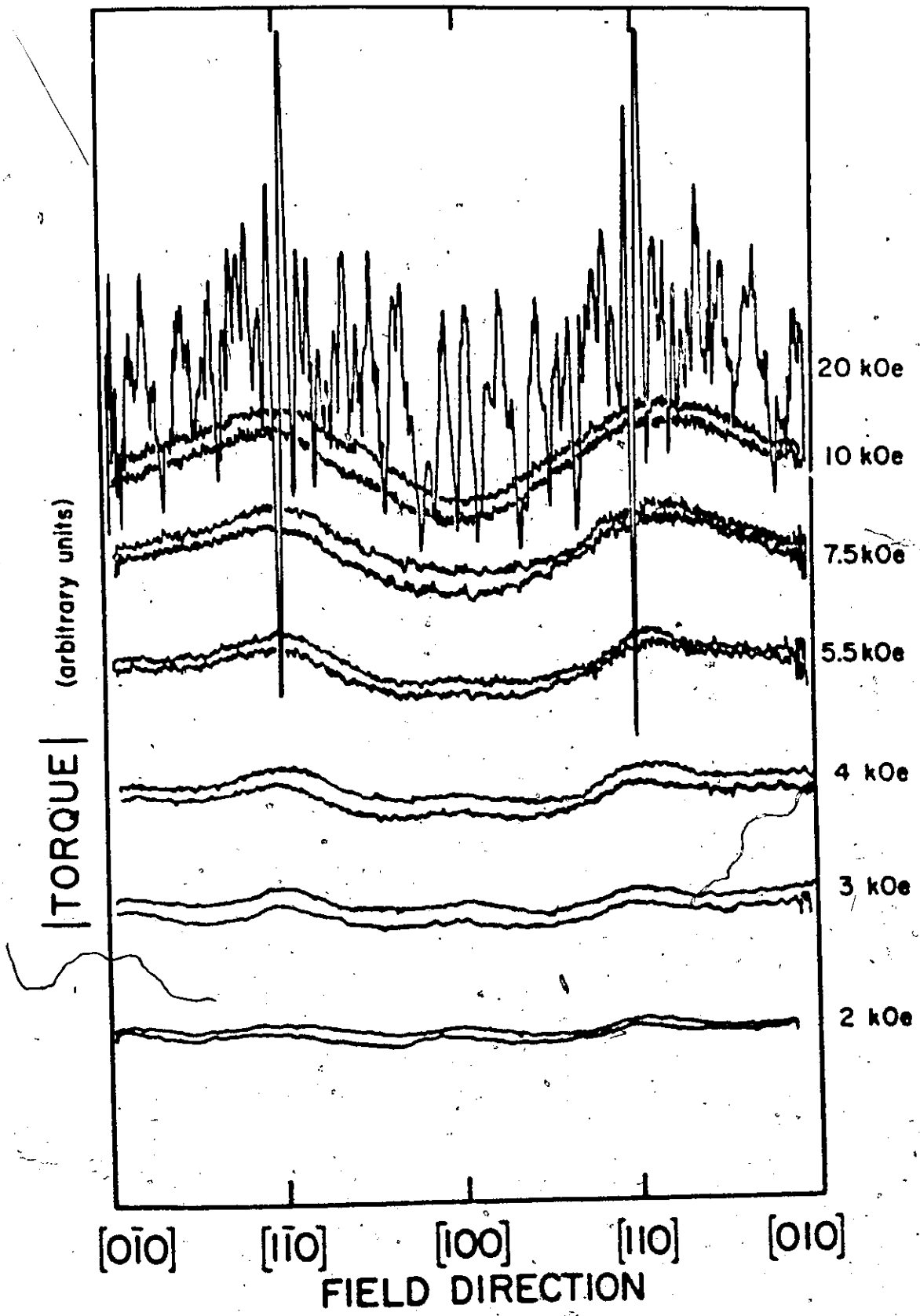
20 kOe
10 kOe
7.5 kOe
5.5 kOe
4 kOe
3 kOe
2 kOe
|TORQUE| (arbitrary units)
[0$\bar{1}$0]
[1$\bar{1}$0]
[100]
[110]
[010]
FIELD DIRECTION

the approximate expression [15] can give a very good qualitative picture of the field dependence of the induced torque.

A typical set of torque rotation diagrams for aluminum at 1.5 K is shown in Fig. 15. Here the field was rotated in a (010) plane at 40°/min. The sample was a 5.8 mm diameter sphere (with asphericity less than 1%) spark-cut from a nominal 5-9's purity single crystal. The induced component of the total torque, for this and other spheres, was obtained by digitally recording the total torque in both rotation directions and selecting the component which is odd in Ω. The even-Ω torques are generally small, except at the higher fields, where the de Haas-van Alphen torque oscillations become important. The broad minima in the high-field induced torque evident in Fig.15 at <100> directions were also observed as the field was rotated through <100> directions in the (110) plane. Similar minima were seen at <111> directions in the (110) and (112) rotation planes. These high-field induced torque minima were also found in spheres which were spark-cut from single crystals that had been strained along a low-symmetry axis by 1%, 5% and 8%. These minima persisted as the temperature was raised from 1.2 K up to 25 K, where the minima gradually disappeared as the increased phonon scattering removed the sample from the high-field condition. The induced torque tended towards high-field saturation for all

field orientations, and showed no evidence of open orbits induced by magnetic breakdown in fields up to 20 kOe. There was no evidence of linear magnetoresistance up to $\omega\tau = 7$.

The computed magnetoresistivity tensor was used with eq. [14] to obtain theoretical induced torque at field directions in (100), (110) and (112) planes, for which extensive experimental data were available (Holroyd et al 1973). The theoretical induced torque was fitted to our induced torque data using two parameters which scaled $\omega\tau$ and the torque magnitude independently. The fitting was carried out for each sample plane, simultaneously fitting the complete set of measured fields (typically 0.5 or 1.0 kOe intervals over the range 0 to 20 kOe), with the data and theory sampled at 5° intervals. The fitted theory is shown in Figs. 16-18 for the (100), (110) and (112) planes of sample 1 (unstrained, nominal 5-9's purity aluminum at 4.2 K). The points are experimental data, graphed for selected fields and orientations, and the solid lines are the corresponding theoretical fits. The two parameter torque model fits both the field dependence and the anisotropy of the experimental induced torque. At symmetry directions the low-field torque maxima as well as the high-field torque minima are reproduced. The origin of these anisotropies may be understood by considering the approximate induced torque, given by [15]. The induced torque

Figure 16. The experimental specific induced torque (that is, the induced torque normalized by the sample size and rotation speed using eq. [14] and theoretical fit in the (100) plane of sample 1. The points are the experimental values, shown for field rotations at selected fields (left) and the field dependence at selected orientations (right). Only selected values are plotted since all of our data could not be clearly shown on one such diagram. The solid lines are the two-parameter least-squares fit to the complete set of all 36 field rotations. The theory to which these data were fitted is the exact induced torque expression of eq. [14] using the resistivity tensor function of H calculated using the uniform relaxation time path-integral over our modified single-OPW Fermi surface.

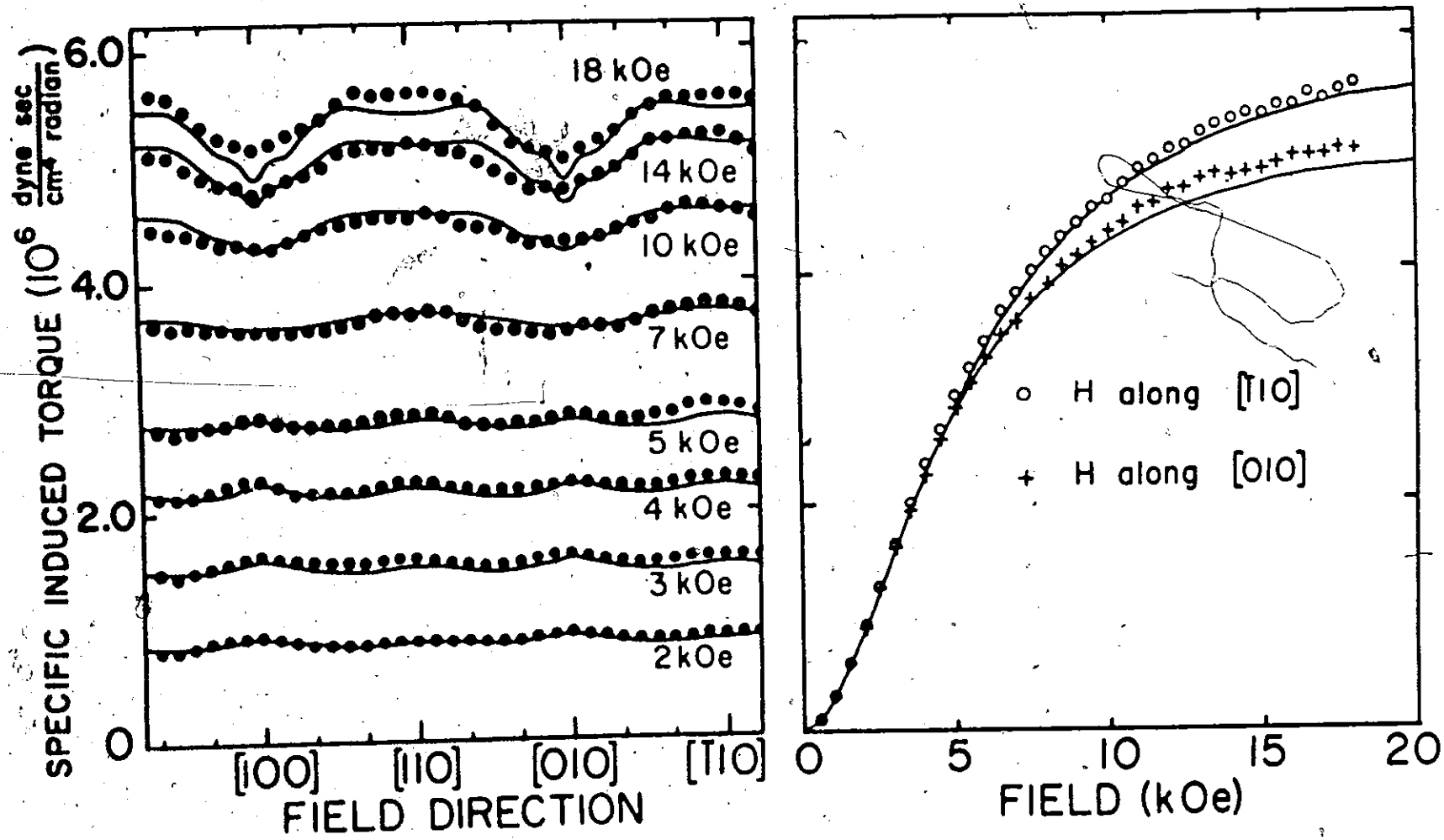
SPECIFIC INDUCED TORQUE (10^6 dyne sec / cm^4 radian)
6.0
4.0
2.0
0
18 kOe
14 kOe
10 kOe
7 kOe
5 kOe
4 kOe
3 kOe
2 kOe
[100]
[110]
[010]
[$\bar{1}$10]
FIELD DIRECTION
0
5
10
15
20
FIELD (kOe)
H along [$\bar{1}$10]
H along [010]

Figure 17. The experimental specific induced torque and theoretical fit in the (110) plane of sample 1. The points are experimental field rotations at selected fields (left) and the field dependence at selected field orientations (right). The solid lines are the two parameter least-squares fit of our theory to the data.

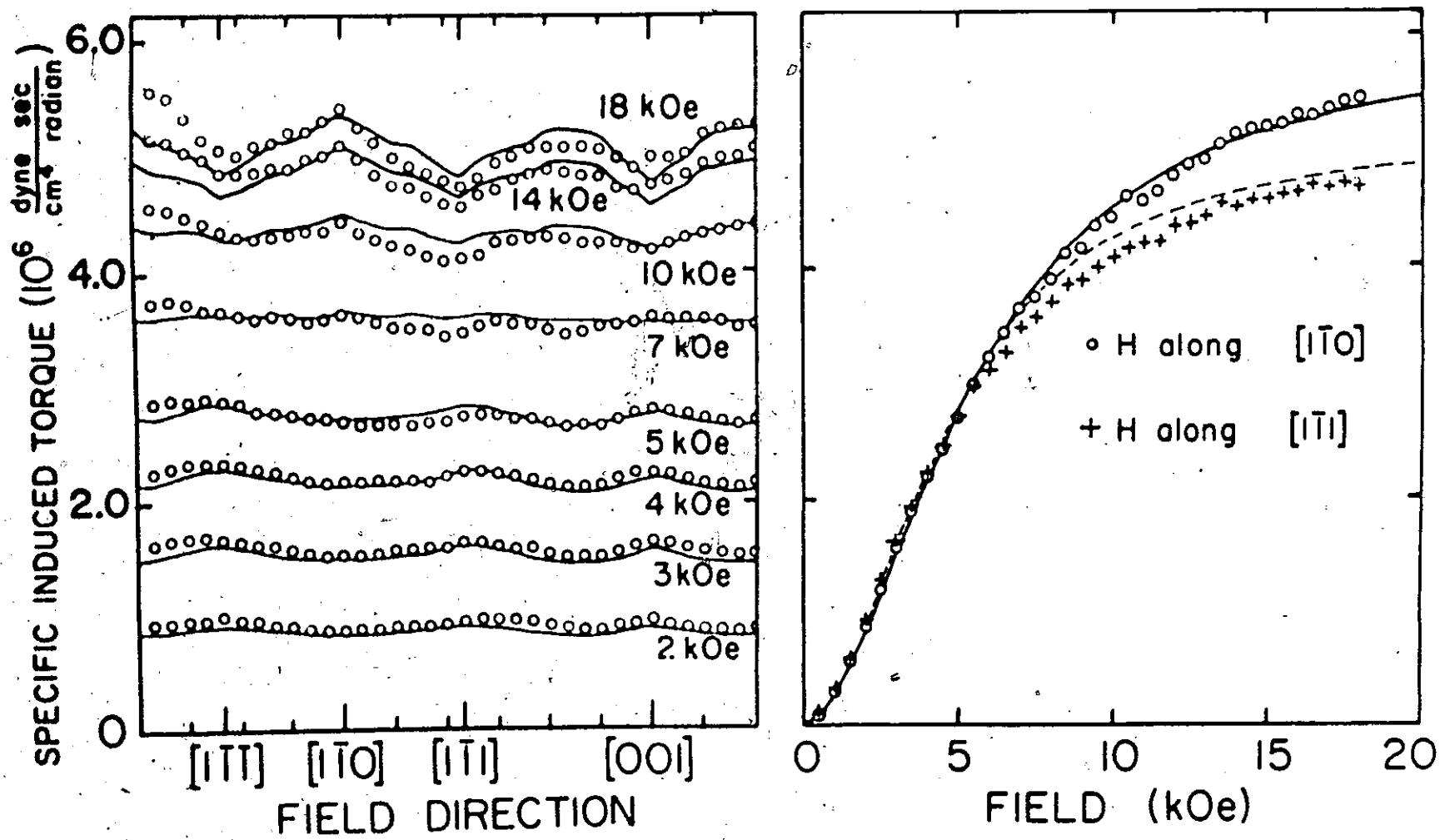
SPECIFIC INDUCED TORQUE (10^6 $\frac{dyne\ sec}{cm^4\ radian}$)
6.0
4.0
2.0
0
18 kOe
14 kOe
10 kOe
7 kOe
5 kOe
4 kOe
3 kOe
2 kOe
[1TT]
[1T0]
[1T1]
[001]
FIELD DIRECTION
0
5
10
15
20
FIELD (kOe)
o H along [1T0]
+ H along [1T1]

Figure 18. The experimental specific induced torque and theoretical fit in the (112) plane of sample 1. The points are the experimental field rotations at selected fields (left) and the field dependence at selected field orientations (right). The solid lines are the two parameter least squares fit of our theory to data.

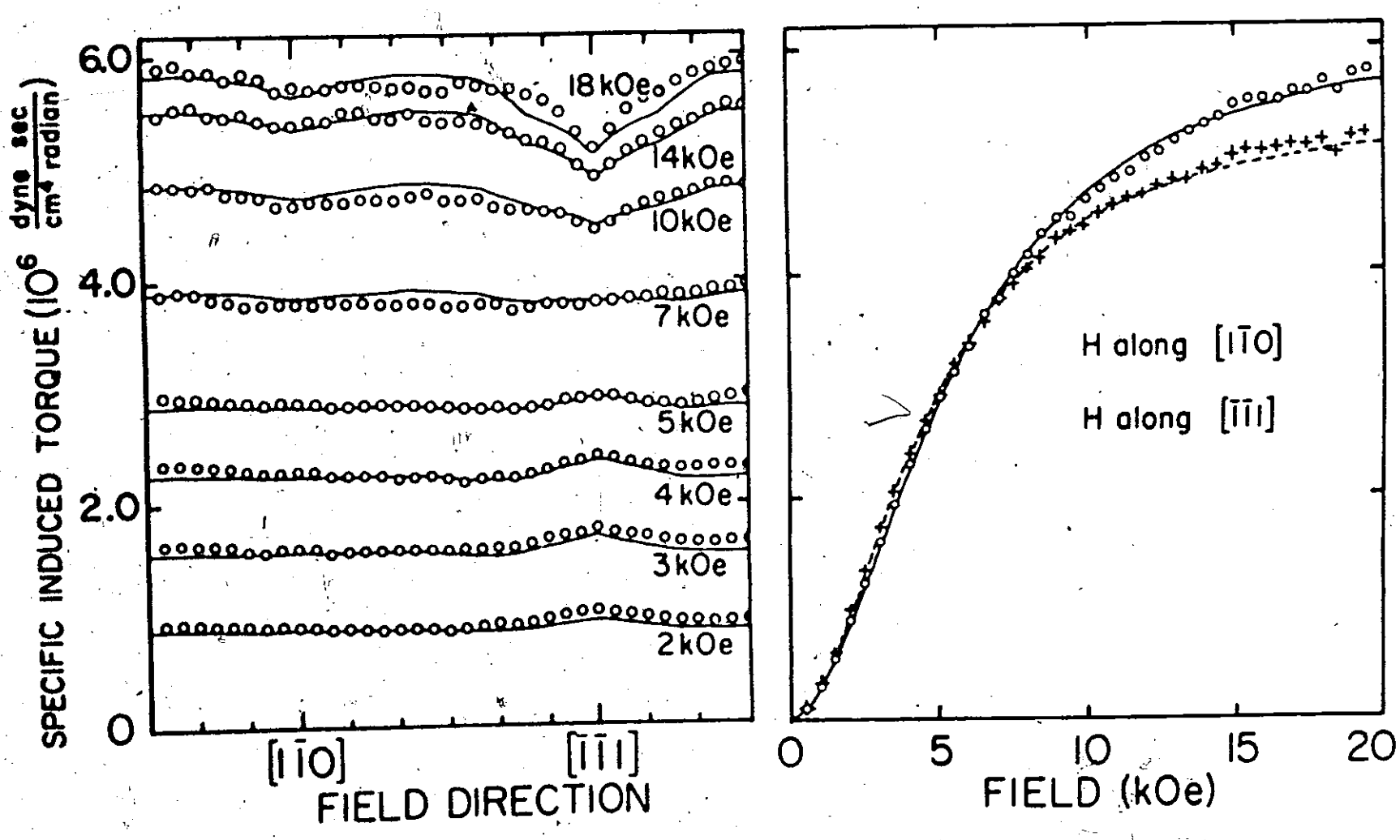
SPECIFIC INDUCED TORQUE (10^6 dyne sec / cm^4 radian)
6.0
4.0
2.0
0
18 kOe
14 kOe
10 kOe
7 kOe
5 kOe
4 kOe
3 kOe
2 kOe
[1$\bar{1}$0]
[$\bar{1}\bar{1}$1]
FIELD DIRECTION
H along [1$\bar{1}$0]
H along [$\bar{1}\bar{1}$1]
0
5
10
15
20
FIELD (kOe)

minima at <100> and <111> field directions arise from the ρ_{zz} minima in the high-field region where the Hall terms dominate the denominator of Eq. [15]. In lower fields, where the ρ_{zz} minima still exist, but where the Hall term contribution to the denominator is small, the same ρ_{zz} minima generate torque maxima. The main effect of the much smaller, calculated transverse magnetoresistance anisotropy is to partially counteract the effect of the ρ_{zz} anisotropy; in particular it tends to equalize the induced torque minima at <100> and <111> directions.

The two fitting parameters provide a measure of the experimental deviation from the theoretical Kohler plots calculated by the path-integral method. The field fitting parameter yields a value of $\omega\tau$ for each field, so that we can extract a relaxation time from the fitted value of this parameter for each plane of data. This relaxation time τ (the bare relaxation time, in the absence of the electron-phonon interaction) and the fitted $\omega\tau$ values determine the absolute theoretical resistivity components at each field, since we have calculated $\tau\rho_{ij}(\omega\tau)$ using the path-integral method. The resistivity components in turn determine the specific induced torque (the induced torque normalized by dividing the induced torque by the product of the angular rotation rate and the fifth power of the sample radius). Thus the field dependence of the induced torque in its rise to saturation together with our calculations determines a

theoretical specific induced torque amplitude which may be compared with experiment.

Our two parameter fits of theory to experiment have root mean square deviations of less than 2.5% of the maximum torque in each plane, for every sample. The fits were consistently best in the (100) plane, where the average deviation was 1.6%; and worst in the (110) plane (2.3% average deviation). The (112) planes had an average deviation of 1.8%.

The two fitting parameters were completely consistent for the three measured planes of each sample. They varied by less than 3% for the three planes, in every sample. The relaxation times which were derived from the fitted field scaling parameter values were within 10% of the mean value for all planes of all samples, including those strained by up to 8%. The mean value of τ was 1.9×10^{-11} sec.

The ratios of the predicted to measured induced torque were also consistent. Although uncertainties in the torque magnetometer calibration and sample radius generate a 10% uncertainty in the absolute amplitude of the induced torque, the ratio varied by less than 15% from sample to sample, with less than 2% variations from plane to plane in any one sample.

The average ratio of measured to predicted torque amplitude was 1.3. We do not feel that this is a systematic error in the magnetometer calibration, but a real discrepancy between the theoretical and experimental resistivities. We conclude that the theoretical high-field value of $(\rho_{xx}+\rho_{zz})$

is some 30% too small in our simple calculations. Path-integral calculations using the four-OPW Fermi surface (Chapter VI) predict a high-field value of $(\rho_{xx}+\rho_{zz})$ which is 15% larger than the SOPW calculations, mostly due to changes in ρ_{zz}.

Path-integral calculations assume that the scattering is catastrophic (as defined on page 13), and this approximation in our calculations is the most probable cause of the discrepancies.

D. Discussion and Comparison with Other Measurements

In this section, the results of our path-integral calculations are compared to previous calculations and to experiments other than induced torque. The limitations of the calculations, and the consequences of some extensions of the simplest path-integral model are discussed for each type of galvanomagnetic component.

D.1 Hall Terms

The isotropic relaxation time approximation gives a field dependence of the Hall coefficient which is in good agreement with the extensive aluminum Hall effect data at intermediate and high fields (Borovik 1952; Forsvoll and Holwech 1965; Amundsen and Seeberg 1968). Feder and Lothe (1965) calculated the field dependence of the Hall coefficient with the magnetic field along <100>, and obtained results that are similar to ours for that direction. Ashcroft (1969) has

also calculated the field dependence of the Hall coefficient in aluminum in the low to intermediate field regime. The magnetic field at the zero crossing point depends on the relaxation time anisotropy and the k_z distribution of $\omega_c\tau$.

The measured high-field value of A_H corresponds to 1.00±.01 holes per atom, and is isotropic to within 1%. This is reproduced by our calculations, as would be expected by simply considering the Fermi surface volumes of the electrons and holes. This good agreement is due in part to the Hall conductivity independence from the scattering mechanism in uncompensated metals, and in part to the orbital averaging of τ. The effects of relaxation time anisotropy are discussed further in Chapter VI.

D.2 Transverse Terms

For an uncompensated metal with no open orbits, the path-integral magnetoresistance saturates at high fields. Our isotropic relaxation time calculations of the transverse saturation magnetoresistance give values of $\Delta\rho/\rho_o$ which vary from 2.28 to 2.68 depending on the crystallographic orientation. Our value of 2.67 with z along <100> is not in good agreement with the value of 2.97 obtained by Feder and Lothe in their kinetic calculation, although both calculations use the same physical assumptions.

The experimental results do not generally show saturation but rather a high-field linear magnetoresistance

of varying slope (Kesternich and Ullmaier 1971), with higher purity (i.e. higher residual resistance ratio) samples giving generally larger slopes. No evidence of any linear magnetoresistance was seen in our induced torque experiments, since these experiments did not probe to high enough values of $\omega\tau$. We define a pseudo-saturation value of the transverse magnetoresistance as that high-field magnetoresistance value where the magnetoresistance curvature with field approaches zero. In most, but not all experiments, this magnetoresistance value, just before the linear term becomes apparent, falls in the range 1.5 to 2.0 (Kesternich and Ullmaier 1971; Balcombe and Parker 1970; Chiang et al, 1969; Borovik and Volotskaya 1965; Balcombe 1963; Volotskaya 1962; Ficket 1971; Balcombe and Parker 1970); which is well below our calculated values and consistent with our induced torque measurements.

The origins of the linear magnetoresistance are discussed in Chapter IV.

D.3 Longitudinal Terms

The experimental longitudinal magnetoresistance is smaller than the experimental transverse magnetoresistance, as is predicted by our path integral calculations. The experimental "saturation" values are generally larger than our calculated values (Balcombe and Parker 1970; Fickett 1971; Lutes and Clayton 1965), and the longitudinal magnetoresistance also shows a linear magnetoresistance which cannot

be predicted by the simple path-integral theory.

The anisotropy of the longitudinal magnetoresistance is difficult to measure using the conventional four-probe technique, since this entails correlating the magnetoresistance from different samples. The leadless induced torque technique circumvents this difficulty, and permits us to probe the galvanomagnetic properties of a given sample with the field along any crystallographic direction. We draw the major corroboration of our calculated anisotropy (see Fig. 12) of the high-field longitudinal magnetoresistivity of aluminum from the agreement between the calculated and measured induced torque.

The calculated longitudinal magnetoresistance agrees quite well with previous calculated values for H along <100>. Pippard (1964) estimated a saturation value of $\frac{\Delta\rho_{zz}}{\rho_o}$ of 0.35, Feder and Lothe obtained a value of 0.31, while our calculated value is 0.33. Each of these calculations results from the calculation of the conductivity using a nearly free electron Fermi surface (no rounding at the zone boundaries) and a uniform relaxation time.

The fact that the band of orbits near any extremal orbit contributes but little to the longitudinal conductivity means that the use of central orbits (Lutes and Clayton 1965) for interpreting size-effect data on longitudinal magnetoresistance can be quite misleading.

D.4 Longitudinal-Transverse Terms

Heretofore little has been done about the longitudinal transverse terms either experimentally or theoretically. The largely academic interest in them is in knowing the size of the error introduced by neglecting them. Although our calculated longitudinal-transverse resistivity can be as large as 16% of ρ_o, the effects on the usually measured properties (the Hall coefficient, the transverse resistivity, and the induced torque) are small (less than 0.001%, 0.8% and 0.5% respectively at $\omega\tau = 100$). The effects of the longitudinal-transverse terms on the transverse resistivity and induced torques are largest in the high-field regime, where they very slightly modify the saturation values. The largest changes in the Hall coefficient occur at low to intermediate fields. It is smaller (less than 0.2% change in the low-field limit) than the effects on the other components. The largest changes in the longitudinal magnetoresistivity occur at intermediate fields ($\omega\tau \sim 1$) where there is a change of up to ±0.2% in the determinant of the conductivity matrix, which is the only place the longitudinal-transverse conductivity components enter the expression for the longitudinal resistivity.

CHAPTER IV

INDUCED TORQUE IN HIGH-PURITY ALUMINUM

A. Introduction

The excellent reproducibility of previous induced torque experiments (Holroyd et al, 1973) in 5-9's single-crystal aluminum, combined with the inherent advantages of being able to investigate the galvanomagnetic anisotropy of samples using a probeless method, encouraged us to extend the low-field, 5-9's purity induced torque data to appreciably higher $\omega\tau$. The four-probe experiments (Volotskaya 1963; Borovik and Volotskaya 1965; Chiang et al 1969; Balcombe 1963; Kesternich and Ullmaier 1971) which have been done on high purity aluminum show an alarming degree of irreproducibility, with transverse magnetoresistance which does not (usually) saturate but rather exhibits a linear or quasi-linear increase with field in the high-field regime. The linear term is reported to be largest for <110> magnetic field directions, where the dimensionless slope S, where $S = \frac{\Delta\rho}{\rho_o \omega\tau}$, is as large as 5×10^{-2} (Kesternich and Ullmaier, 1971) or even as large as 0.1 (Borovik and Volotskaya, 1965). Any such linear transverse magnetoresistance would be evident in an induced torque experiment (on a spherical sample) as a linear increase of induced torque

with field, as may be seen by inspecting Eq. [15], the approximate expression for induced torque. Using the exact expression, Eq. [14], leads to the same conclusion.

There are additional difficulties which arise in induced torque experiments in higher conductivity samples: for uncompensated metals the high-field saturation torque decreases as $\frac{1}{\tau}$, while the de Haas-van Alphen torque oscillations increase in size; the coupled mechanical-helicon oscillations (Delaney and Pippard, 1971) also increase dramatically with sample purity and with sample size. The experimental remedies of these two difficulties are to some extent mutually exclusive: the most obvious cure for the former difficulty is an increase in sample radius since the induced torque increases as R^5 while the de Haas-van Alphen torque increases only as R^3, but the larger samples that this would suggest generates coupled mechanical-helicon oscillations which are even more troublesome than the de Haas-van Alphen torque.

B. Sample Preparation

The high-purity samples were cast as spheres rather than cutting spheres from a single crystal by spark erosion as had been done for the 5-9's aluminum. The monocrystalline spheres were grown under high vacuum in high-purity graphite moulds using a modified Bridgman technique, using the apparatus shown in Fig. 19. The moulds were cleaned by

Figure 19. Apparatus for growing mono-crystalline spheres of aluminum.

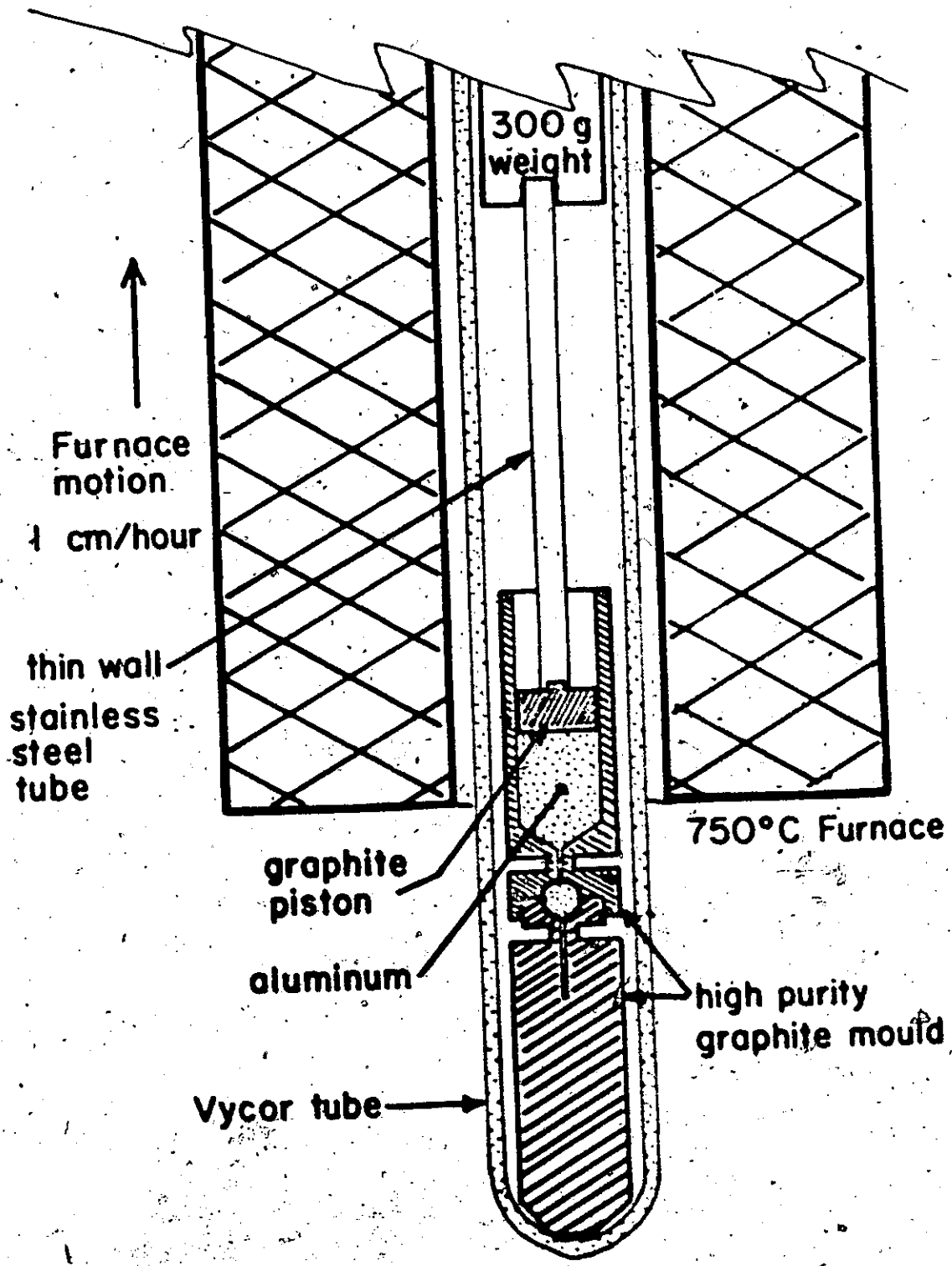
300 g
weight
Furnace
motion
1 cm/hour
thin wall
stainless
steel
tube
750°C Furnace
graphite
piston
aluminum
high purity
graphite mould
Vycor tube

first soaking in acid and subsequently baking them under high vacuum at 1300 K. This process also removed the layer of loose carbon which acts as a release agent in unbaked moulds, and so a thin layer of loose carbon was deposited in two hemispherical cavities from an oxygen-poor bunsen burner flame. The mould was again baked under vacuum at 1300 K. The reservoir was filled with aluminum, and the piston fitted in place. (It was necessary to use aluminum chunks rather than a single piece, since the latter melted so rapidly that the ensuing collapse would squirt the molten aluminum around the piston.) With a 300 gm weight ($\sim 3\times10^5$ dynes/cm^2 pressure) the molten aluminum filled the 0.030 inch access hole and starting tube, and did not pass the piston which had a clearance of up to 0.004 inches with the reservoir. The furnace, at a temperature of 750°C, was raised at the rate of approximately 1 cm per hour. The heat flow was controlled by the necks in the mould at the top and bottom of the spherical cavity, and a (low thermal conductivity) thin-wall stainless steel tube supporting the weight. These heat flow controls were necessary to ensure that the starting tube would be the first part to freeze, and the access hole would be the last. These were checked respectively by examining the crystal orientation of the sphere and the starting tube, and checking the exterior for external

voids and the density for interior voids. Providing that pressure was maintained in the reservoir (that is, barring leaks) the samples grown in this manner were invariably void-free single crystals, usually with a <100> growth axis (although <111> growth axes were also observed). The fill tube was cut as far from the sample as possible with a jeweller's saw and the mould separated. If the mould had been properly carbonized, the differential contraction of the graphite and aluminum allowed the mould and the sample to fall apart. To remove the starting and fill tips, the samples were heavily etched in a concentrated aqueous solution of NaOH, or heavily electropolished, using Heidenreich's electrolyte (Heidenreich, 1949), to a smooth finish. The samples were then carefully checked for asphericity, and oriented to within 0.5° by back-reflection Laue X-ray diffraction.

The best results (in the sense of the highest $\omega\tau$ values combined with the smallest spurious torques) were obtained with a $\frac{3}{16}$ inch diameter sphere grown from 6-9's grade aluminum obtained from Cominco. This sample was electropolished to a mirror-like sphere with a mean diameter of 0.180 inch, with deviations from sphericity that were less than ±3%. The sample was oriented and mounted in a Kel-F holder using Glyptal cement. The sample holder was friction fitted and glued to a 2 mm diameter quartz rod, and the oriented

sample glued in place with a <100> axis within 1° of the axis of the quartz rod. The orientation X-ray photographs showed a mosaic spread of approximately 1° - about twice the smallest which we obtained in this manner for any sample. (Aluminum is notorious for its inherently large mosaic spread (Gilman, 1963). The rod was suspended in a fixed dewar from a nulling torque transducer with an electrically variable compliance (Vanderkooy and Datars, 1967). The compliance was increased until the nulling system could effectively damp the coupled mechanical-helicon oscillations. A fifteen inch Varian iron-core electromagnet was used with a one inch gap to obtain fields up to 29 kOe. It could be rotated at angular rotation rates (Ω) of up to 45 degrees per minute. For each field, the torque was recorded as a function of angle for both senses of magnet rotation. The two torques at each angle were subtracted one from the other. This gives the induced torque and should be free of the de Haas-van Alphen torque which is independent of the sense of Ω.

C. Results

The induced torque at intermediate fields showed the same anisotropy as did the lower purity samples. The <110> and <100> directions are the directions of particular interest, and the field dependence of the induced torque for fields in these directions are shown in Fig. 20. The <110> directions are of interest since with the magnetic field

along a <110> direction the four-probe measurements find the largest linear term in the transverse magnetoresistance. The expectedly large linear field dependence of the induced torque is absent. The dimensionless slope, $S = \frac{\Delta\rho/\rho}{\omega_o\tau}$, is less than 10^{-3} at <110>, compared to four probe measurements at <110> of S = 0.05 and S = 0.1 (Kesternich and Ullmaier 1971, and Borovik and Volotskaya 1965). In all orientations the induced torque follows the predictions of the path-integral calculations, except for a narrow angular region (±3°) around <100> directions. The field dependence of the <100> directions is also shown in Fig. 20, where the linear-like term with $S=7\pm1\times10^{-3}$ in these orientations may be seen. Where the de Haas-van Alphen oscillations of torque are fortuitously quiescent near <100>, at 26 kOe, the <100> anomaly may be seen clearly on the rotation diagram in Fig. 21. The anomaly looks suspiciously like a small open orbit peak in the induced torque. Balcombe (1970) has suggested magnetic breakdown for fields along <100> in aluminum, to explain his four-probe magnetoresistance data for fields up to 60 kOe. In the field regime where the probability of magnetic breakdown is quite different from 0.0 or 1.0, there is an open orbit character (or extended orbit character) to the network of orbits undergoing magnetic breakdown which could generate just such an anomaly around <100>.

Figure 20. The field dependence of the induced torque in high-purity aluminum in the (001) plane, for fields in the <100> and <110> directions. The two <100> directions have been averaged as have the two <110> directions. The lines result from the two parameter fit to these data - the same procedure as was used for the lower purity aluminum data (Figure 16).

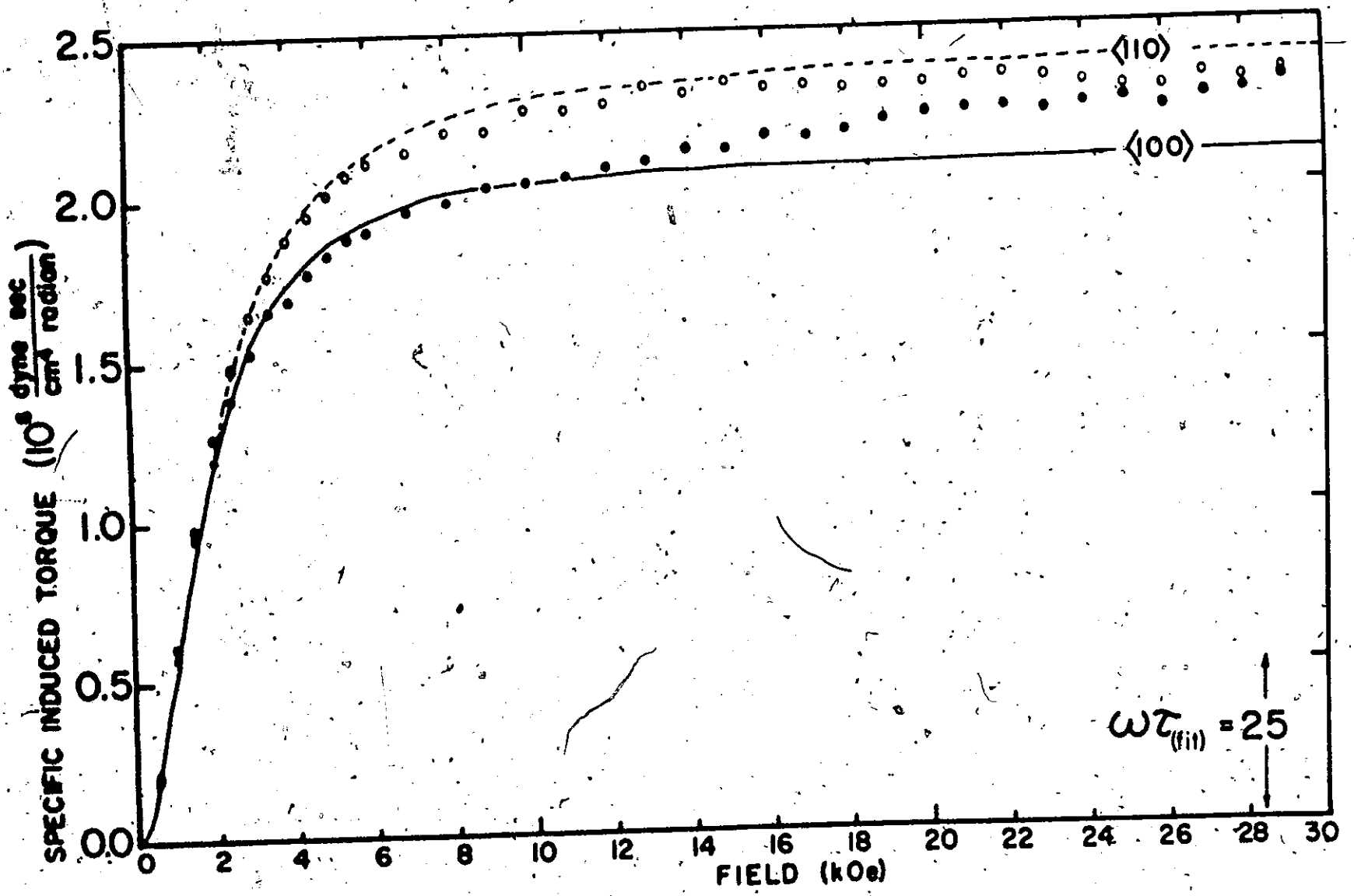
SPECIFIC INDUCED TORQUE ($10^6 \frac{\text{dyne sec}}{\text{cm}^3 \text{ radian}}$)
2.5
2.0
1.5
1.0
0.5
0.0
0
2
4
6
8
10
12
14
16
18
20
22
24
26
28
30
FIELD (kOe)
⟨110⟩
⟨100⟩
$\omega\tau_{(fil)} = 25$

Figure 21. The torque rotation diagrams for high-purity aluminum at 4.2 K, in a magnetic field of 26 kOe, rotating at 31°/min. The sample radius is 2.33±.06 mm. The offset of the upper curves is twice the induced torque. In the lower curves this offset has been reduced to show the increase in induced torque near the <100> field directions.

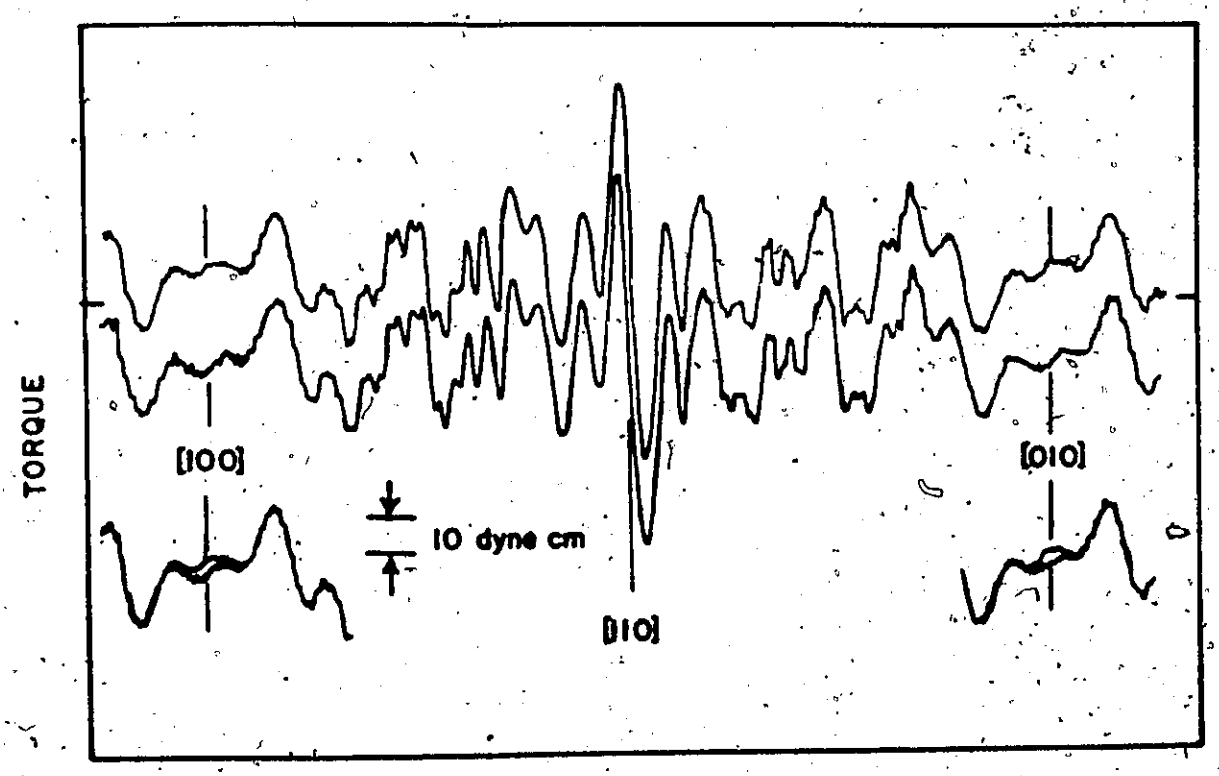
TORQUE
[100]
10 dyne cm
[110]
[010]

The lines in Fig. 20 are 2-parameter fits of the single-OPW, uniform relaxation time path integral magnetoconductivity calculations. The theory does not include magnetic breakdown in the <100> direction, and has difficulty in fitting this direction. The fitted value of τ, the relaxation time derived from the $\omega\tau$ scaling was 5.0×10^{-11} sec, and the predicted induced torque amplitude (from the value of τ) and the fitted amplitude scale factor agreed to within 35%, with the predicted amplitude being too small, as was the case for the 5-9's aluminum data.

Other samples, grown in a similar manner, exhibited lower relaxation times, but they also showed no evidence of a linear term to the induced torque except near the <100> directions.

This search for a linear term to the induced torque which could be correlated with the four probe linear transverse magnetoresistance gave persistently negative results. With the exception of the <100> orientation, the induced torque in high-purity aluminum could be understood for fields in the (100) plane using the simple path-integral theory. The <100> anomaly was not considered to have sufficient information (only its slope) to unambiguously determine whether or not magnetic breakdown was responsible, and so path-integral calculations invoking magnetic breakdown in aluminum were not attempted. Other possible origins of linear magnetoresistance are discussed in Chapter VI.

CHAPTER V

MAGNETOCONDUCTIVITY OF INDIUM

A. Introduction

In this chapter, we discuss the field dependence and anisotropy of the magnetoresistivity tensor components of indium as calculated by the uniform relaxation time path-integral over a nearly free-electron Fermi surface. The results are compared with the calculations for aluminum, and with the experimental results of indium. It was not possible to compare the theoretical and measured induced torque, as was done for aluminum. Despite a concerted effort to grow single-crystal spheres of indium for induced torque experiments, using techniques similar to those described in Chapter IV, all such samples were either polycrystalline or too badly twinned for the measured induced torque anisotropy to be useable as a test of the calculated galvanomagnetic properties of indium.

The comparison of these calculations with those of aluminum is based on the similarity of the basic Fermi surface topology of indium and aluminum: the first zone of each metal is full; the second band hole surfaces are very similar to the re-mapped segments of the free electron Fermi sphere; the third band electron surfaces are ring-like structures

which differ significantly from the free-electron constructions; and the fourth zone is empty. Neither metal has been found to support open orbits in fields below 18 kOe.

Despite these similarities, there are differences due to the different crystal classes of the two metals. Indium is face centered tetragonal (fct) with c/a = 1.0831 at low temperatures (Barett, 1962), and aluminum is face centered cubic. The Brillouin zone of indium may be generated from the Brillouin zone of aluminum by compressing the latter's zone by some 8% along [001], the four-fold axis. This distortion changes the symmetry of what would have otherwise been equivalent crystallographic directions in the two metals, while loosely preserving the similarities in shape between their Fermi surfaces. The different symmetries are reflected in the galvanomagnetic properties of the two metals.

The Fermi surface which was used for these calculations was the single-OPW surface of indium, with the second band hole surface modified near W to exclude open orbits, as shown in Fig. 5 (in Chapter II). The galvanomagnetic consequences of leaving the open orbit band in place may be seen in Fig. 4, and since these dramatic effects have not been observed, we have used the disconnected Fermi surface to represent the hole surface. The electron surface that was used is a composite of the third and fourth band single-OPW Fermi surfaces. It consisted of a ring with its axis along [001] and, disconnected from it, two half-rings along each of [100]

and [010], as shown in Fig. 5. The major deficiency of this model is the sharp cusp which exists at any Bragg reflection.

The uniform relaxation time path-integral over this Fermi surface was done in the manner described in Chapter II, and the field dependence of the magnetoresistivity tensor components were determined as described for aluminum in Chapter III. The field dependences were calculated for fields in the (100), (001) and (110) planes of indium. The (100) and (001) planes, which are equivalent for fcc aluminum, are not equivalent for fct indium.

B. Calculated Galvanomagnetic Properties

B.1 Hall Terms

The calculated anisotropy of the Hall coefficient, $A_H = \rho_{yx}/H$, for fields in the (100), (001) and (110) planes, is shown in Fig. 22 for $\omega\tau$ values of 0.02, 0.1, 0.2, 0.4, 1.0 and 10. These three xz planes are all mirror planes, so that the irreducible even-field Hall terms are zero, and there is no ambiguity in the Hall coefficient since $\rho_{xy} = -\rho_{yx}$, by the Onsager relation. The calculated Hall coefficient is isotropic in both the low-field and high-field limits, but exhibits considerable anisotropy at intermediate fields. The field dependence of the Hall coefficient is shown in Fig. 23 for fields along <100> and <001>. The low-field Hall coefficient implies a carrier concentration of three electrons per atom (within 2% at $\omega\tau = 0.02$), while in the high-field limit the implied carrier concentration is within 1% of one hole per atom.

Figure 22. The calculated anisotropy of the Hall coefficient, $A_H = \rho_{yx}/H$, of fct indium. The anisotropy is shown in the (010), (001) and $(1\bar{1}0)$ mirror planes, for different values of $\omega\tau$.

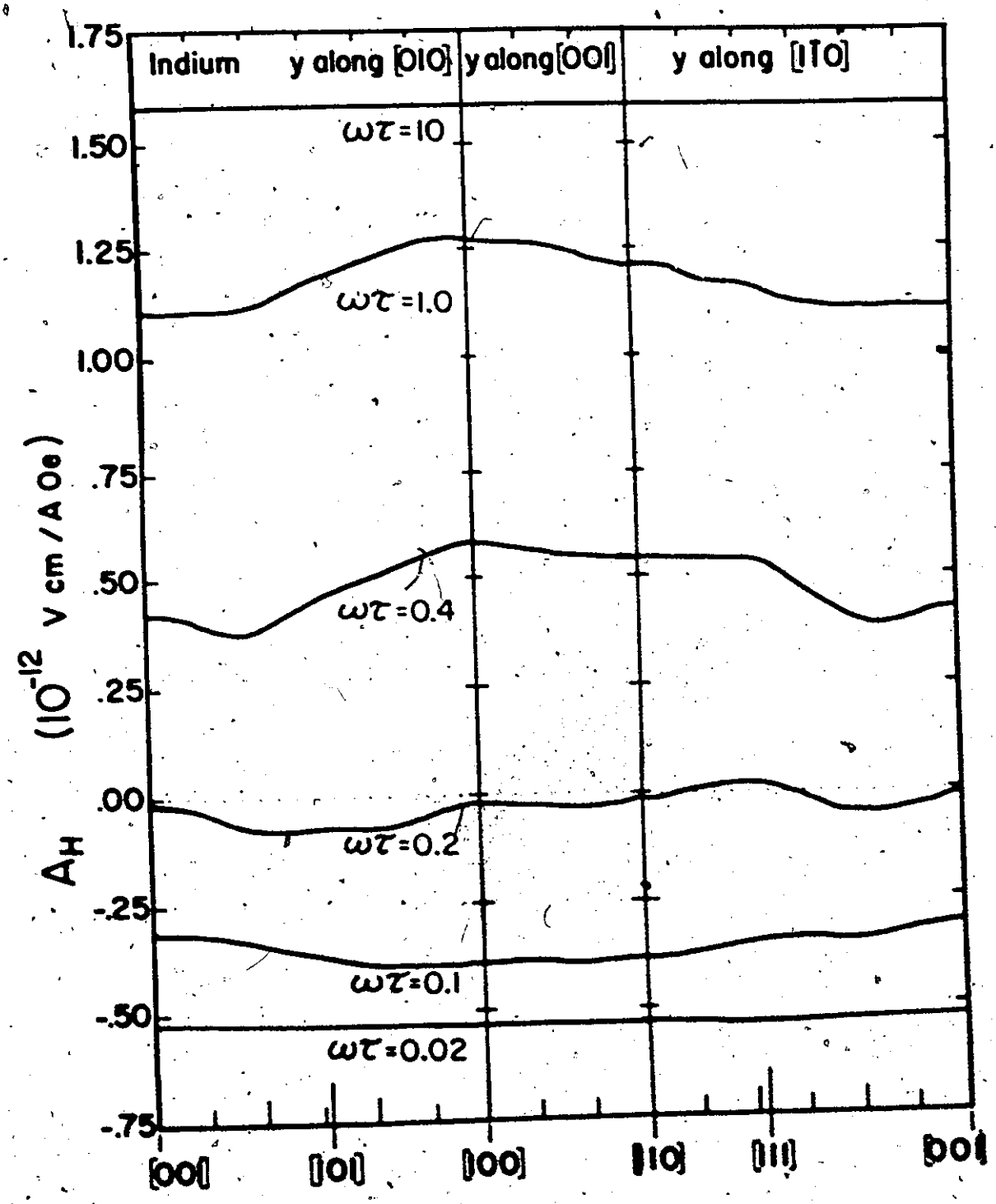
Indium
y along [010]
y along [001]
y along [1$\bar{1}$0]
$\omega\tau$=10
$\omega\tau$=1.0
$\omega\tau$=0.4
$\omega\tau$=0.2
$\omega\tau$=0.1
$\omega\tau$=0.02
1.75
1.50
1.25
1.00
.75
.50
.25
.00
-.25
-.50
-.75
A_H (10^{-12} V cm / A Oe)
[001]
[101]
[100]
[110]
[111]
[001]

Figure 23. The calculated field dependence of the Hall coefficient of indium for fields along the four-fold axis (<001>) and along a pseudo-four fold axis (<100>).

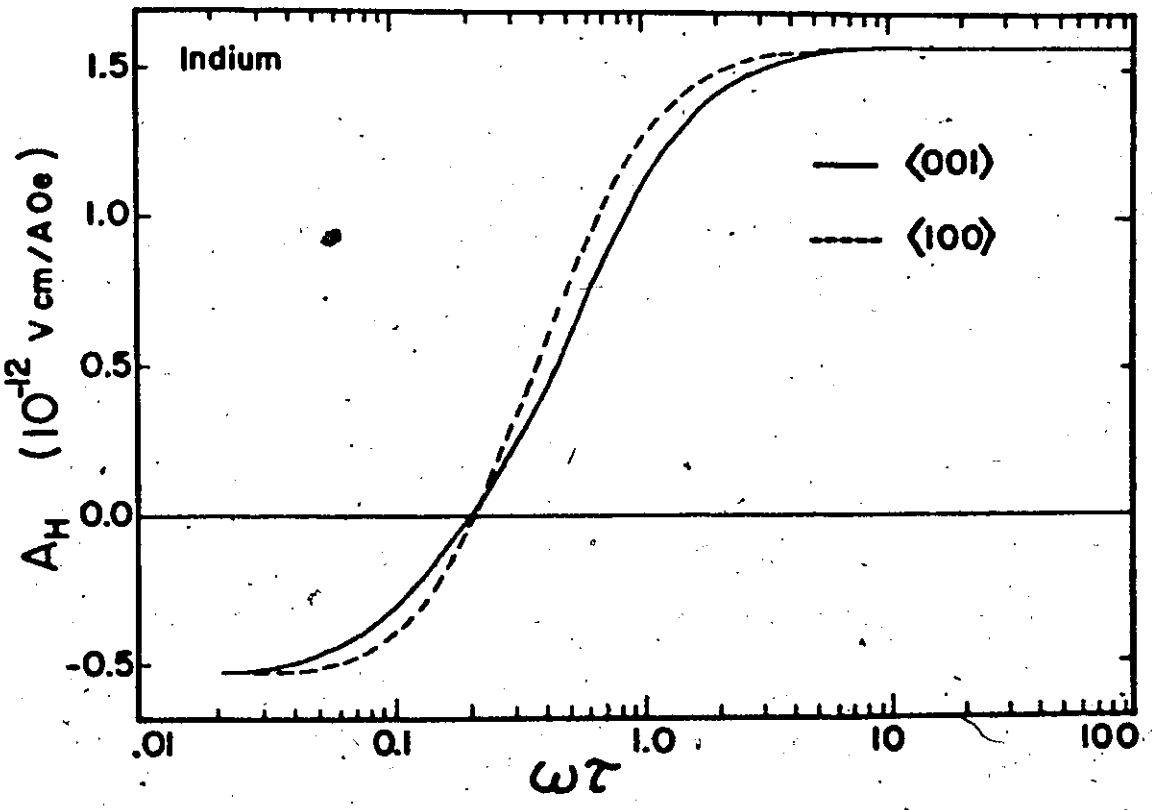
Indium
⟨001⟩
⟨100⟩
1.5
1.0
0.5
0.0
-0.5
A_H (10^{-12} V cm/A Oe)
.01
0.1
1.0
10
100
$\omega\tau$

B.2 Transverse Terms

The calculated zero-field resistivity, ρ_o, is isotropic even though indium is not cubic. This is the case because our Fermi surface model is a virtually complete (though re-mapped) sphere, and the relaxation time and Fermi velocity are uniform over this sphere. The anisotropy of ρ_o for other conductivity models of indium is discussed in Chapter VI. The isotropic ρ_o is (to within 0.3%) equal to $m_o/(ne^2\tau)$, where n is the carrier density, and for indium at low temperatures $\rho_o\tau = 3.03\times10^{-20}$ Ω cm sec.

The field dependence of the calculated transverse magnetoresistances, $(\rho_{xx}-\rho_o)/\rho_o$ and $(\rho_{yy}-\rho_o)/\rho_o$, are shown in Fig. 24-a by the dotted and dashed lines respectively, for selected field orientations. There is again a linear low field magnetoresistance. At an $\omega\tau$ value of 6, the transverse magnetoresistance has reached to within 1% of the high-field saturation value. The calculated anisotropy of the high-field transverse saturation magnetoresistance of indium is shown in Fig. 25-a by the upper curves.

B.3 Longitudinal Term

The field dependence of the calculated longitudinal magnetoresistance of indium, $(\rho_{zz}-\rho_o)/\rho_o$, is shown by the solid lines in Fig. 24-a for selected field orientations, and the anisotropy of the saturation value is shown in Fig. 25-a by the lower solid curve, for field orientations in the (010), (001) and (110) planes.

Figure 24. Calculated magnetoresistance as a function of $\omega\tau$ for indium (Figure 24-a) and aluminum (Figure 24-b), for selected field directions. The solid curves are the field dependences of the longitudinal magnetoresistance for field directions specified in the angular brackets, and for a magnetic field direction in the $(1\bar{1}0)$ plane 25° from [001]. The dashed curves give the field dependence of $(\rho_{yy}-\rho_o)/\rho_o$ for fields along the symmetry directions specified, with y along [010], [001] and $[1\bar{1}0]$ directions for fields along [001], [110] and [111] axes respectively. The transverse magnetoresistance component $(\rho_{xx}-\rho_o)/\rho_o$ is shown for the same field directions, graphed as the dotted line.

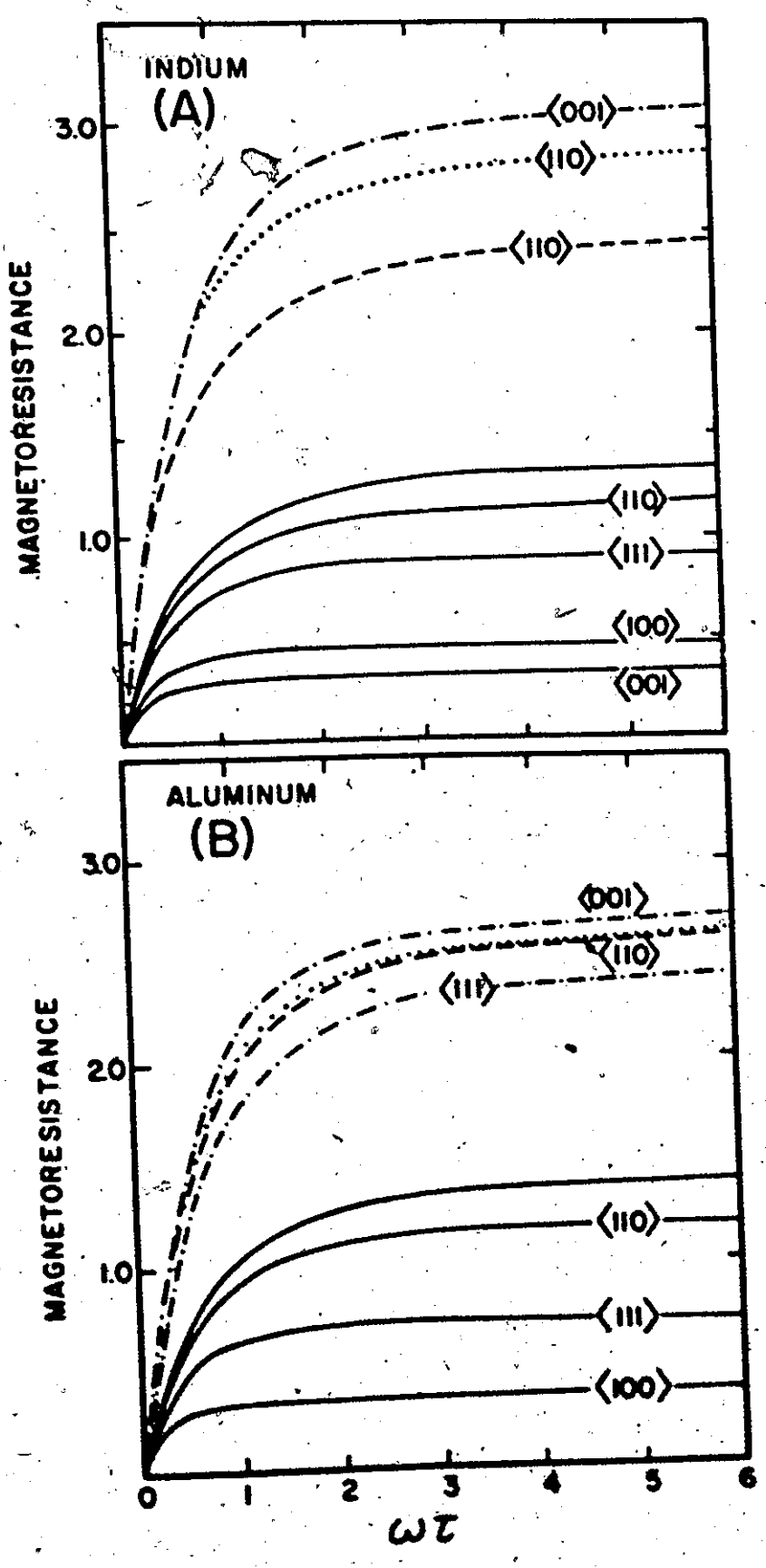
INDIUM
(A)
MAGNETORESISTANCE
3.0
2.0
1.0
⟨001⟩
⟨110⟩
⟨110⟩
⟨110⟩
⟨111⟩
⟨100⟩
⟨001⟩
ALUMINUM
(B)
MAGNETORESISTANCE
3.0
2.0
1.0
⟨001⟩
⟨110⟩
⟨111⟩
⟨110⟩
⟨111⟩
⟨100⟩
0
1
2
3
4
5
6
ωτ

Figure 25. Anisotropy of the calculated saturation (high-field) value of the three magnetoresistance components for indium (Figure 25-a) and aluminum (Figure 25-b), with the magnetic field in the (010), (001) and $(1\bar{1}0)$ planes. The lower solid curve in each graph is the saturation longitudinal magnetoresistance. The upper solid curve is the saturation transverse magnetoresistance $(\rho_{yy}-\rho_o)/\rho_o$, which is to be compared with experimental magnetoresistance rotation diagrams for currents along [010], [001] and $[1\bar{1}0]$ directions, for fields rotated in (010), (001) and $(1\bar{1}0)$ planes, respectively. For completeness, the other transverse magnetoresistance component $(\rho_{xx}-\rho_o)/\rho_o$, is shown by the dashed curve. Equivalent planes (010) and (001) of aluminum are both shown to facilitate comparison with indium.

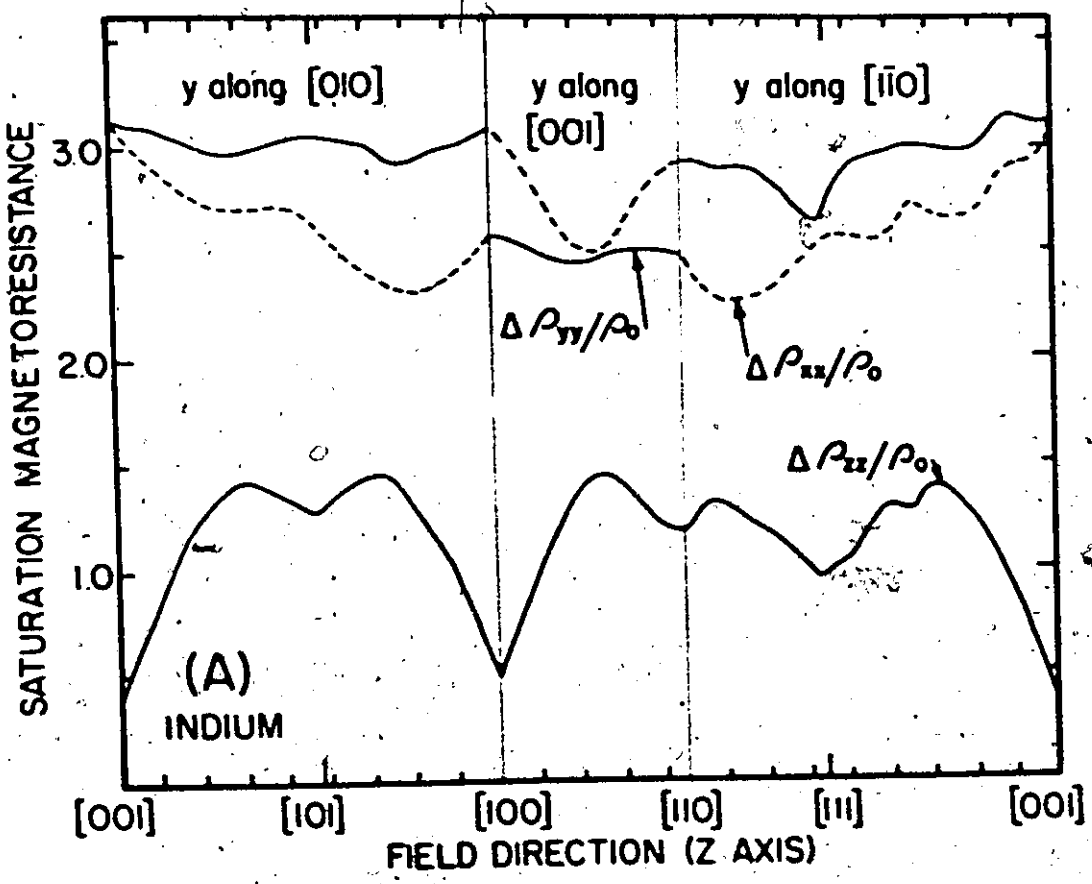
y along [010]
y along [001]
y along [1̄10]
SATURATION MAGNETORESISTANCE
3.0
2.0
1.0
Δρyy/ρo
Δρxx/ρo
Δρzz/ρo
(A)
INDIUM
[001]
[101]
[100]
[110]
[111]
[001]
FIELD DIRECTION (Z AXIS)

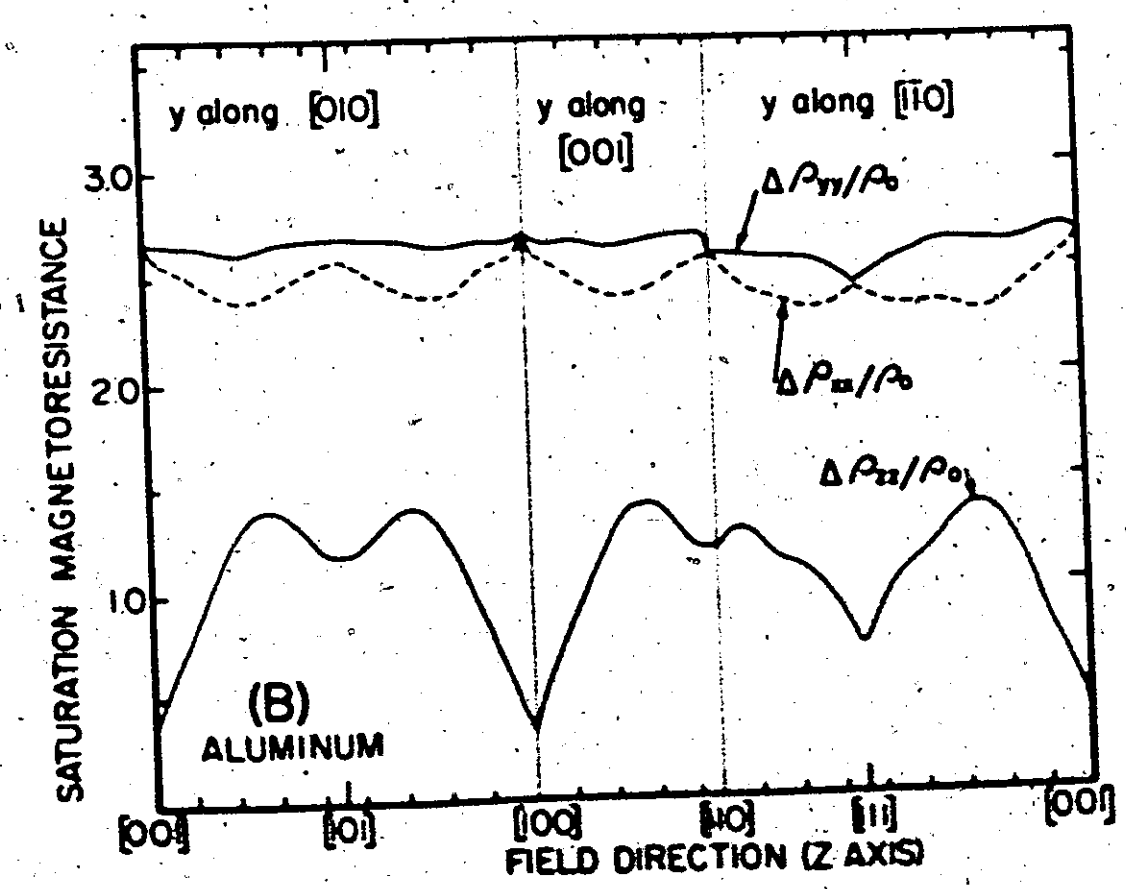
y along [010]
y along [001]
y along [1̄10]
SATURATION MAGNETORESISTANCE
3.0
2.0
1.0
Δρyy/ρo
Δρxx/ρo
Δρzz/ρo
(B)
ALUMINUM
[001]
[101]
[100]
[110]
[111]
[001]
FIELD DIRECTION (Z AXIS)

B.4 Longitudinal-Transverse Terms

The longitudinal-transverse terms (ρ_{xz}, ρ_{zx}, ρ_{yz} and ρ_{zy}) are zero for field orientations along symmetry directions of two-fold or higher symmetry. In the three planes we have calculated, only ρ_{xz} and ρ_{zx} saturate in the high-field limit. For all these calculations, the x-z plane is a mirror plane, so that ρ_{yz} and ρ_{zy} have H^{-1} field dependence in the high-field limit. The calculated anisotropy of the high-field saturation value of ρ_{xz}/ρ_o is shown in Fig. 26.

C. Discussion and Comparison with Experiment

C.1 Hall Terms

The general behaviour of the Hall coefficient of indium parallels that calculated for aluminum. For both metals there are low-field and high-field limits which are isotropic. Because of the different atomic densities of the two metals, the calculated Hall coefficients have different values, but in each case the low-field asymptote corresponds to three electrons per atom (within 2%) and the high-field value to one hole per atom (within 1%). The intermediate-field anisotropy of the Hall coefficient is larger for indium than it is for aluminum, as may be seen by comparing equivalent (and pseudo-equivalent) planes of Fig. 22 (indium) and Fig. 10 (aluminum). The larger anisotropy of A_H for indium arises from the larger anisotropy of the k_z distribution of $\omega_c\tau$ for indium compared to aluminum.

Figure 26. The calculated anisotropy of the high-field saturation value of the longitudinal-transverse resistivity of indium, for fields in the (010), (001) and $(1\bar{1}0)$ planes of indium. The planes are all mirror planes so that ρ_{yz} and ρ_{zy} tend to zero as H^{-1} in the high-field limit. The plotted longitudinal-transverse term ρ_{xz}, is equal to ρ_{zx} in the high-field limit.

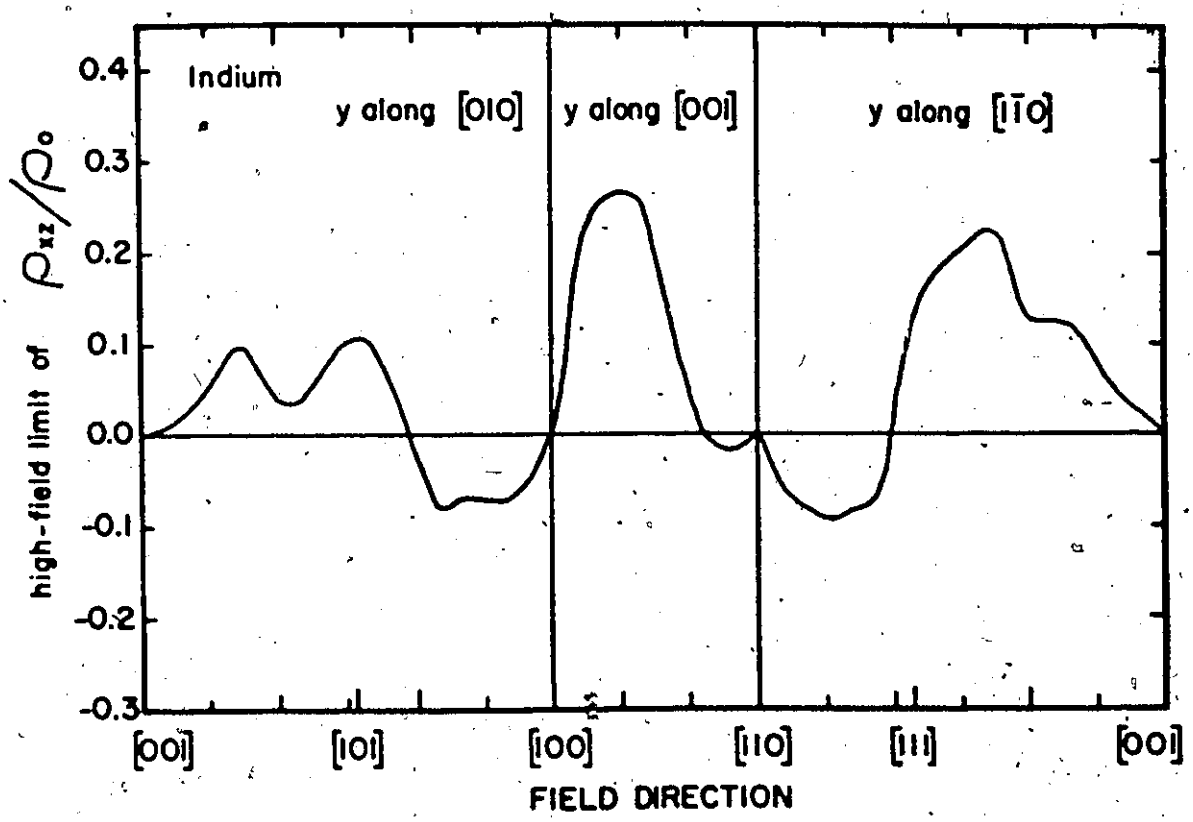
Indium
y along [010]
y along [001]
y along [1$\bar{1}$0]
high-field limit of ρ_{xz}/ρ_0
0.4
0.3
0.2
0.1
0.0
-0.1
-0.2
-0.3
[001]
[101]
[100]
[110]
[111]
[001]
FIELD DIRECTION

The predicted high-field Hall coefficient of indium is 1.577×10^{-12} V cm A^{-1} Oe^{-1}, which is in good agreement with the measured values. Amundsen (1966) measured A_H as 1.58×10^{-12} V cm A^{-1} Oe^{-1} with an uncertainty of 1.5%. Garland and Bowers (1969) found the high-field Hall coefficient to be isotropic within 1%, as theory predicts.

The change in sign of the Hall coefficient of indium has been experimentally observed in single-crystal indium by Garland (1969). His data are compared with our calculations in Fig. 27. Garland's data may be arbitrarily scaled in the abscissa for each sample (corresponding to a choice of τ for each sample), and Garland's ordinate axis calibration error is "of the order of 10%". There is good qualitative agreement, but the field dependence of the theory is too rapid for $\omega\tau < 0.2$, and too slow for $\omega\tau \sim 0.5$. The anisotropy that is evident in Garland's data at the lowest fields cannot be explained by the (re-mapped) spherical Fermi surface. This anisotropy might be due, in part, to the apparent absence of the "α-arms" in indium, as will be discussed in Chapter VI. While this can account for the low-field anisotropy, Garland's low-field asymptotic value for A_H for fields along [100] is more negative than the re-mapped sphere would predict, and discarding the α-arms would accentuate this discrepancy.

C.2 Transverse Terms

The field dependence of the transverse magnetoresistance calculated for indium and aluminum are quite similar in general

Figure 27. The field dependence of the calculated and experimental Hall coefficient of indium. The experimental data are the helicon data of Garland (1969).

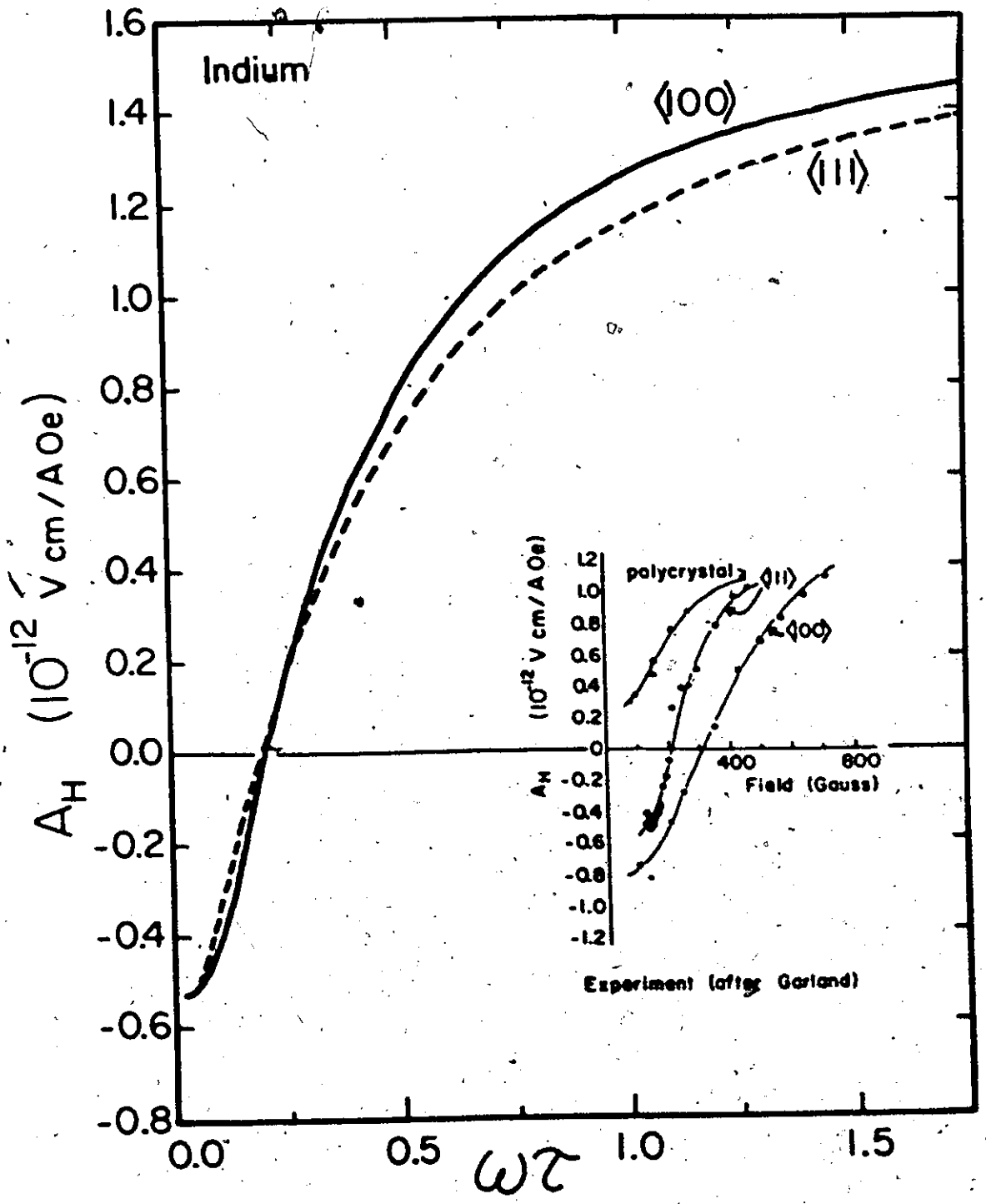
Indium
⟨100⟩
⟨111⟩
A_H (10^{-12} V cm/A Oe)
$\omega\tau$
1.6
1.4
1.2
1.0
0.8
0.6
0.4
0.2
0.0
-0.2
-0.4
-0.6
-0.8
0.0
0.5
1.0
1.5
polycrystal
⟨111⟩
⟨100⟩
(10^{-12} V cm/A Oe)
A_H
Field (Gauss)
400
800
Experiment (after Garland)

form, as may be seen by comparing Fig. 24-a with Fig. 24-b. The major differences are in the high-field saturation magnetoresistance, whose anisotropy is shown by the upper curves in Figs. 25-a and 25-b for the (010), (001) and (110) planes of both metals. The saturation value of the calculated transverse magnetoresistance tends to be larger for indium than for aluminum, and the anisotropy of the transverse magnetoresistance is appreciably larger for indium than it is for aluminum. This may be understood best by considering a high-field approximation for uncompensated metals with no open orbits: ρ_{xx} is proportional to the k_z integral of $\langle(k_x-\bar{k}_x)^2\rangle$ and ρ_{yy} depends in the same way on $\langle(k_y-\bar{k}_y)^2\rangle$, where $\bar{k}_x$ and $\bar{k}_y$ are the reciprocal space coordinates of the orbit centroids, and the angular brackets denote an orbit integral (Wagner, 1972). Only the large orbits (those on the second band hole surfaces) need be considered. The third band electrons contribute less than 2% to the high-field transverse conductivity, due to the small orbit size. This approximation also ignores the effects due to the anisotropy of the longitudinal-transverse terms (less than a 1% error).

Since the integrals of $\langle(k_x-\bar{k}_x)^2\rangle$ and $\langle(k_y-\bar{k}_y)^2\rangle$ over the second band hole surface of indium are generally larger than the same integrals for aluminum, the saturation transverse magnetoresistance is generally larger for indium. The compression of the second band hole surface of indium is some 8% along (001). Compared to aluminum its transverse saturation

magnetoresistance exhibits larger anisotropy. With k_y along (001), ρ_{yy} is a minimum in the high-field limit, due to the smaller k_y extent of the orbits.

The high-field anisotropy of ρ_{yy}, shown by the upper solid line in Figs. 25-a and 25-b, is less than the calculated anisotropy of ρ_{xx} in each plane. The central orbits for all field directions in the x-z plane share a common k_y, while there is no common k_x value for the different field directions, since the x axis rotates with the z axis. This central band of orbits on the second band hole surface, with their partial correlation in k_y, are large orbits and so contribute significantly to σ_{xx} and hence to ρ_{yy}. The partial correlation in k_y, and the lack of any such correlation in k_x, would lead us to expect the anisotropy of ρ_{yy} to be less than the anisotropy of ρ_{xx}, as is the case.

It is the anisotropy of ρ_{yy} which is measured in conventional four-probe measurements of magnetoresistance. We expect the anisotropy to be smallest in planes where there is the most correlation in k_y; that is for y directions where the Fermi surface around $k_x = k_z = 0$ is most nearly flat. Garland's four-probe measurements show this, as may be seen in Fig. 28. The smallest anisotropy in ρ_{yy} was found for the (111) plane, where there is the largest "plateau" on the second band hole surface around $k_x = k_z = 0$; the next smallest anisotropy he found was in the (100) plane which has a smaller plateau; and the largest anisotropy was found for a

Figure 28. The experimental, four-probe anisotropy of the transverse magnetoresistance, $(\rho_{yy}-\rho_o)/\rho_o$, after Garland and Bowers, (1969). (a) y 10° from [110]; (b) y within 1° of [100]; (c) within 1° of [111].

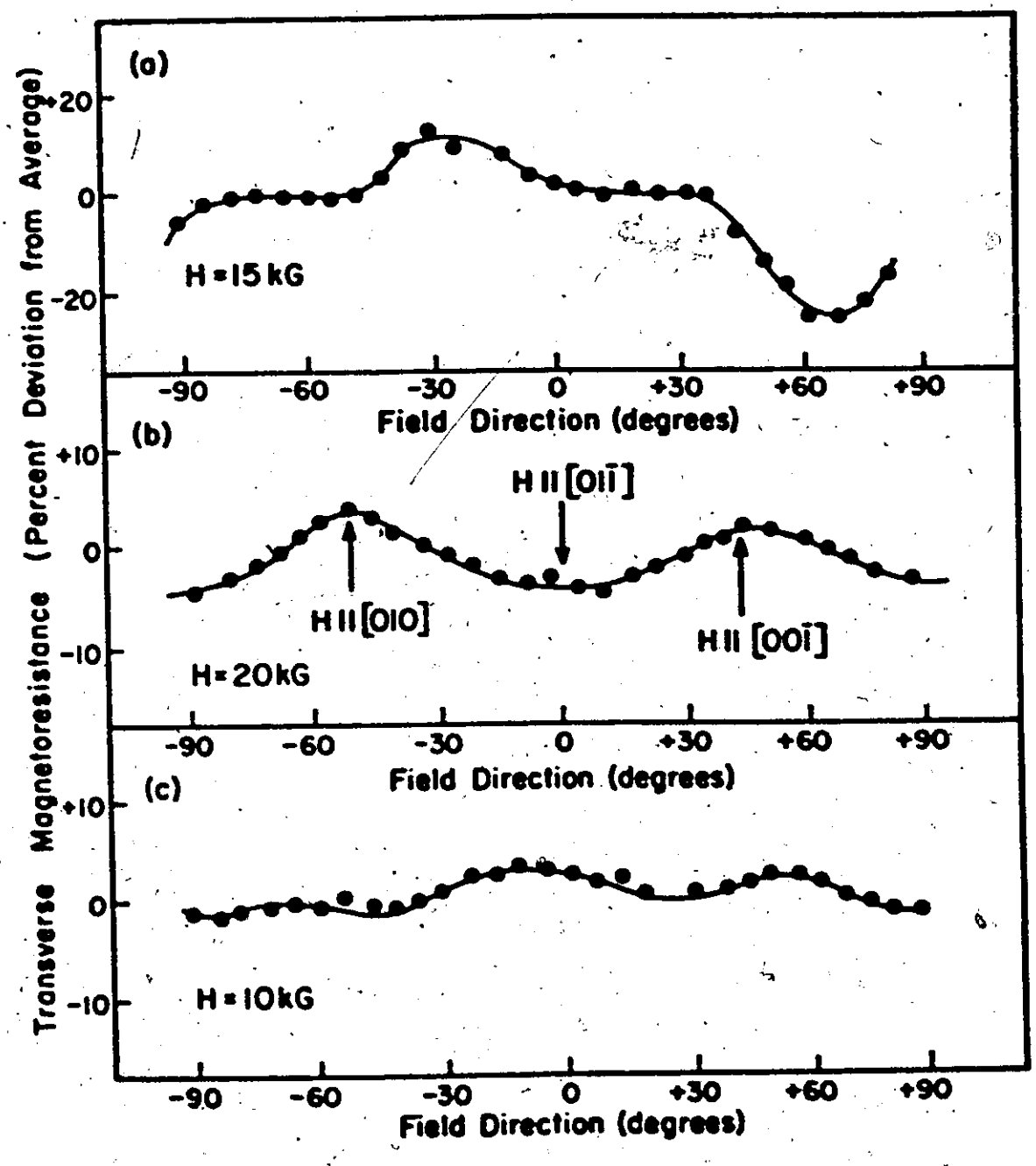
(a)
H = 15 kG
+20
0
-20
-90
-60
-30
0
+30
+60
+90
Field Direction (degrees)
(b)
H ∥ [01$\bar{1}$]
H ∥ [010]
H ∥ [00$\bar{1}$]
H = 20 kG
+10
0
-10
-90
-60
-30
0
+30
+60
+90
Field Direction (degrees)
(c)
H = 10 kG
+10
0
-10
-90
-60
-30
0
+30
+60
+90
Field Direction (degrees)
Transverse Magnetoresistance (Percent Deviation from Average)

plane whose normal was some 10° from the [110] direction, which has no plateau. Garland's measured anisotropy in the (100) plane is larger than is our calculated anisotropy. There are peaks at [010] and [001] in both experiment and calculation, but ρ_{yy} is measured to be larger for fields along [010] than along [001], while the calculations predict the converse. The experimental minimum in ρ_{yy} which is evident in Fig. 28-b for fields near [011] is not reproduced well by our calculations. The comparison of the (110) calculation (Fig. 25-a) to the experiment (Fig. 28-a) cannot be a quantitative one due to the 10° difference in alignment.

A comparison of the calculated high-field magnetoresistance values with experiment is complicated by the existence of linear magnetoresistance in the high-field limit of most four-probe measurements on indium, just as was found for most four-probe measurements on aluminum. This is a serious discrepancy which has occasioned a wide variety of explanations. Since it seems possible with adequate care to eliminate the high-field linear magnetoresistance in potassium (Babiskin and Siebenmann, 1971) and aluminum (preceding chapter), it is likely that the high-field linear magnetoresistance is not an intrinsic effect, but is related to the microstructure of the sample - that is, structure that is small compared to the mean free path, but not small compared to a high-field cyclotron orbit. If the linear magnetoresistance term is subtracted from the data, Garland's and Bowers' (1969) high-field magnetoresistance values range from 1.5 to 2.0 for polycrystalline samples. The theory predicts saturation mag-

netoresistance values of from 2.3 to 3.1, depending on crystal orientation. This is in much better agreement with the single-crystal data of Gaidukov (1965) which show high-field values (less the "linear" terms) of from 2.0 to 2.5. The measurements are systematically lower than our simple theory predicts.

C.3 Longitudinal Term

The calculated field dependences of the longitudinal magnetoresistance of indium and aluminum are much the same. The higher the symmetry of the magnetic field axis, the faster ρ_{zz} saturates, as may be seen by comparing the solid curves of Fig. 24. With the field along a four-fold axis (<001>) in aluminum or indium, ρ_{zz} saturates at the lowest fields. At the pseudo-four-fold axis in indium, ρ_{zz} saturates at somewhat higher fields, but at lower fields than for the <111>, three-fold axis in aluminum. For fields along the pseudo-three-fold <111> of indium, along the two-fold <110>, and far from symmetry, ρ_{zz} saturates at progressively higher fields. This variation in the rate of saturation occurs because the saturation condition is determined by the periodicity of $v_z(\theta)$. If an orbit has n-fold symmetry, the v_z period is a factor of 1/n times as large as the cyclotron period. Most (but not all) cyclotron orbits with the field along an n-fold symmetry axis have n-fold symmetry in indium and aluminum, so that ρ_{zz} in such a direction will saturate at fields that are roughly n times smaller than the saturation field far from any symmetry axis. The cross-correlation of

the indium and aluminum results is possible because of the similarity of $v_z(\theta,k_z)$ on their Fermi surfaces.

A more noticeable feature of the longitudinal magnetoresistance anisotropy is the very large variation in the saturation value of ρ_{zz}, for both indium and aluminum. It varies from 0.3 to 1.5, with the lowest values for fields along high symmetry directions. The saturation magnetoresistance gets progressively larger as one reduces the symmetry of the nearest symmetry axis to the field direction. The magnetoresistance minima result from the more nearly free-electron nature of the longitudinal component of the Fermi velocity on cyclotron orbits around the higher symmetry direction in the crystals. Away from symmetry directions in these two metals, more orbits undergo Bragg reflections which change (or reverse) the z component of carrier velocity. These reflections reduce the z component of the mean free path (a kinky spiral) in the high-field limit, and thus increase the saturation value of ρ_{zz}. For the purposes of checking these predictions, no satisfactory data on indium exist. Garland's and Bowers' (1969) data on polycrystalline samples show high-field longitudinal magnetoresistance values that range from 0.4 to 1.2.

The calculated saturation values of ρ_{xx} and ρ_{zz} exhibit an interesting, but very approximate inverse correlation, which may be seen in Fig. 25. The tendency of ρ_{xx}

to rise as ρ_{zz} falls originates with the constancy of $v_x^2 + v_z^2$ for each point on the Fermi surface, for a fixed direction of y in the crystal.

C.4 Longitudinal-Transverse Terms

The calculated longitudinal-transverse terms of indium and aluminum show limited similarities, as may be seen by comparing Fig. 26 with Fig. 14. Note that the two graphs are not plotted for the same planes. The longitudinal-transverse conductivity tensor components of indium are everywhere small enough, for practical purposes, to be neglected in the matrix inversion to obtain the resistivity tensor, as they were for the case of aluminum. Also as they were in the case of aluminum, they remain experimentally unmeasured.

CHAPTER VI

EXTENSIONS OF THE SIMPLE THEORY

In this chapter we present and discuss the calculated galvanomagnetic consequences of relaxation time anisotropy and of more realistic Fermi surfaces. We also discuss the anisotropy of the transverse high-field linear magnetoresistance, and show that the reported anisotropy of aluminum cannot be accounted for by an orbital conductivity enhancement at high fields.

A. Relaxation Time Anisotropy

The effects of relaxation time anisotropy are illustrated by allowing different relaxation times for the electron and hole bands. We express the field dependences of the galvanomagnetic properties as a function of $\omega\tau_h$, where τ_h is the relaxation time on the hole surface; and as a function of the free parameter τ_e/τ_h, where τ_e is the relaxation time on the electron surface.

A.1 Indium

In Fig. 29 the field dependence of the Hall coefficient of indium with the field along <100>, measured at different temperatures (Garland, 1969), is compared with the calculated

Figure 29. The field dependence of the path-integral calculations of the Hall coefficient of indium, for different ratios of the relaxation time on the electron surface (τ_e) to that on the hole surface (τ_h), compared with the measurements of Garland (1969). Both experiment and calculations are for fields in <100> directions. The Fermi surface used for the calculations was the complete, re-mapped single-OPW sphere.

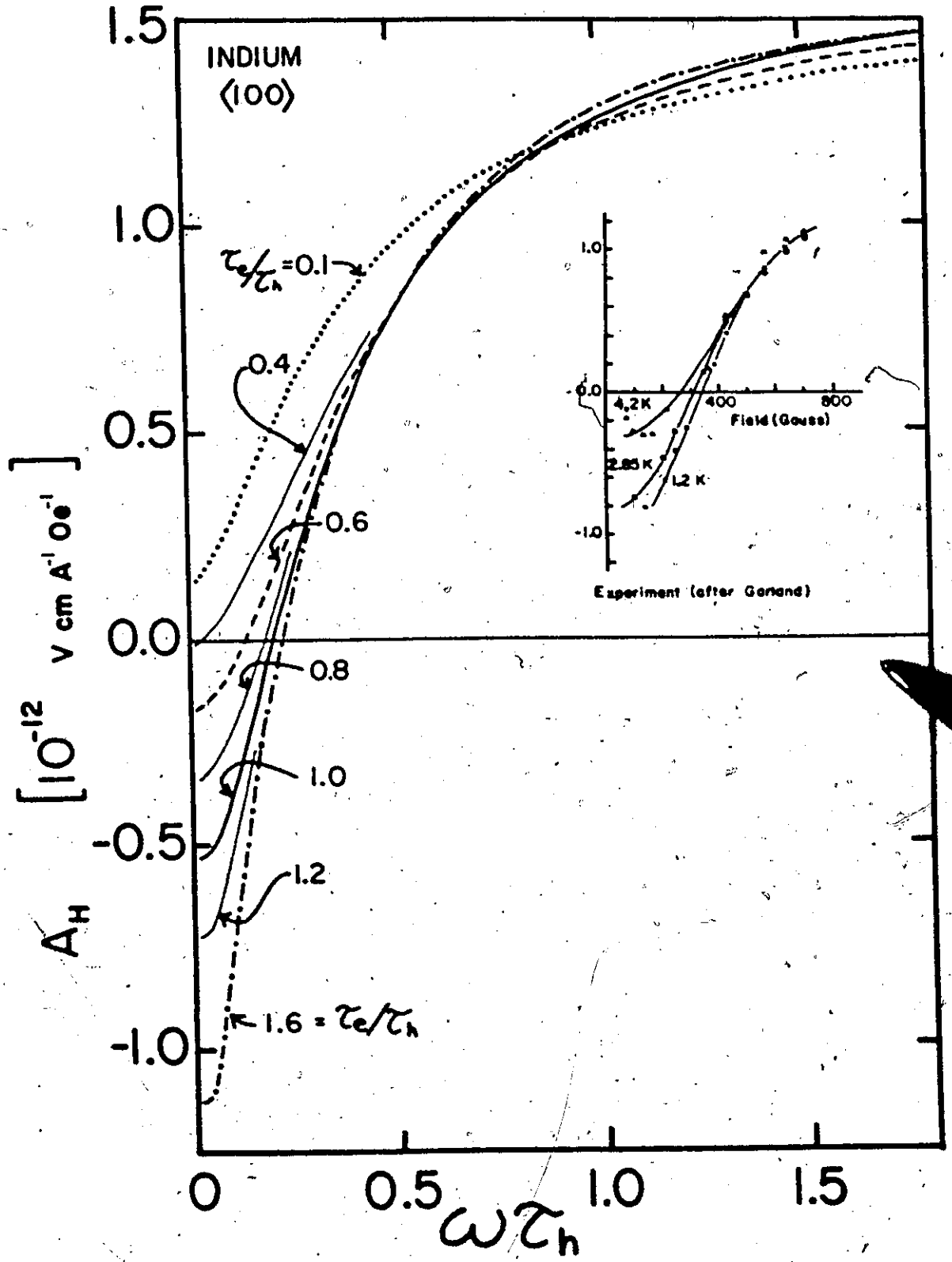
INDIUM
⟨100⟩
τ_e/τ_h=0.1
0.4
0.6
0.8
1.0
1.2
1.6 = τ_e/τ_h
A_H [10^{-12} V cm A^{-1} Oe^{-1}]
$\omega\tau_h$
1.5
1.0
0.5
0.0
-0.5
-1.0
0
0.5
1.0
1.5
4.2K
2.85K
1.2K
400
800
Field (Gauss)
Experiment (after Gerhand)

field dependence for different values of τ_e/τ_h. The parameter τ_e/τ_h has to be about 1.3 to explain the measured low-field value of A_H at 1.2 K, but then the functional form of the field dependence is incorrect. If the functional form is fitted at 1.2 K, then $\tau_e/\tau_h = 0.6$ (which is the value that Ashcroft (1969) estimated from Garland's data from the zero-crossing field); but then the low-field value of A_H is incorrect. Furthermore, the nearly free-electron model we have used has too many electrons, and the use of a more realistic Fermi surface would only compound this discrepancy, as is discussed in the next section.

Despite the difficulty in reconciling our theory with the low-field value of Garland's measurements (which depends on the helicon theory of Chambers and Jones (1962), and has a calibration error which Garland quotes as being "of the order of 10%"), it is possible qualitatively to explain the rapid temperature dependence of the low-field measurements. The scattering rate, $1/\tau$, is the sum of the zero temperature scattering rate ($1/\tau^*$) and the phonon scattering rate, which is a function of temperature. Castaing and Goy (1973) found that, for indium from T = 1 to 4 K, the phonon scattering rate on the electron surface increases much more rapidly with temperature than does the scattering on the hole surface, so that τ_e/τ_h decreases with temperature. Whether or not this reduction in τ_e/τ_h reduces the zero-crossing field of the Hall

coefficient (as Garland has observed), depends on the relative temperature dependence of τ_e and τ_h. The relative temperature dependences which Castaing and Goy quote (cyclotron resonance measurements) do not reproduce Garland's data when coupled with our calculations, even allowing the ratio τ_e/τ_h to be a free parameter. This may be due to differences in the average temperature dependences of the transport relaxation times, τ_e and τ_h, from the orbital cyclotron resonance relaxation time measurements, or the breakdown of the relaxation time approximation, or shortcomings in our Fermi surface model.

The assumption of different relaxation times for the two bands also affects the zero-field resistivity of indium, making it anisotropic. The anisotropy is rather small, amounting to 2% in our nearly free-electron model, assuming $\tau_e/\tau_h = 0.6$, and 5% if the electron conductivity is entirely neglected.

A.2 Aluminum

The variation of τ_e/τ_h for cubic aluminum can produce no such zero-field anisotropy, but there is a change in the low-field Hall coefficient as τ_e/τ_h is varied. The relaxation time anisotropy affects all the resistivity tensor components most in the low-field limit. The results of calculations using $\tau_e/\tau_h = 0.6$ are compared with the $\tau_e/\tau_h = 1.0$ results in Table I. Both the low-field and high-

Table I

Ratio of results for aluminum using $\tau_e/\tau_h = 0.6$ to the results using $\tau_e/\tau_h = 1.0$

	<100>	<110>	<111>
ρ_o	1.11	1.11	1.11
ρ_{xx}(as $\omega\tau\to\infty$)	1.012	1.008	1.012
ρ_{yy}(as $\omega\tau\to\infty$)	1.012	1.007	1.012
ρ_{zz}(as $\omega\tau\to\infty$)	1.085	1.080	1.082
$\rho_{xy}(\omega\tau_h = .02)$	0.337	0.344	0.335
$\omega\tau_h$ where $A_H = 0$	0.74	0.72	0.71

field limits are tabulated for fields along <100>, <110>, and <111> directions.

The four-probe Hall effect measurements of Borovik (1952), and Forsvoll and Holwech (1965), are compared in Fig. 30 with the nearly free-electron calculated field dependences of A_H for both $\tau_e/\tau_h = 1.0$ and $\tau_e/\tau_h = 0.6$. The room temperature data are close to the calculations using $\tau_e/\tau_h = 1.0$, and the 4.2 K data are close to the calculations which use $\tau_e/\tau_h = 0.6$, the value suggested by previous work (Lück, 1966). Intermediate temperatures (78 K) may be explained by assuming intermediate values of τ_e/τ_h.

The decrease in magnitude of the (negative) low-field Hall coefficient when τ_e/τ_h is reduced from 1.0 to 0.6 results from the scaling of the electron contribution to σ_{xy} by a factor of 0.6, and from the scaling of the $\omega\tau_h$ of the peak of the electron contribution by a factor of $(0.6)^{-1}$. Together, these changes scale the low-field limit of A_H by a factor that is slightly less than $(0.6)^2$. A simple two-band spherical parabolic model can reproduce this behaviour fully, at the expense of adding free parameters.

The experimental differences in the Hall coefficient from sample to sample, that are evident at intermediate fields in Fig. 30, may be due in part to different (average) crystal orientations of the different samples, or due to a breakdown of Kohler's rule - (i.e. the zero-field resistivity and the Hall resistivity being scaled by different "relaxation

Figure 30. The calculated and experimental Hall coefficient of aluminum. The (unoriented) experimental data are those of Forsvoll and Holwech (1965). The calculations are for fields along <100>, with a uniform relaxation time and for $\tau_e/\tau_h = 0.6$. The experimental field axis is scaled by the ratio of the Debye temperature (428 K) resistivity to the zero-temperature resistivity, ρ_θ/ρ_o.

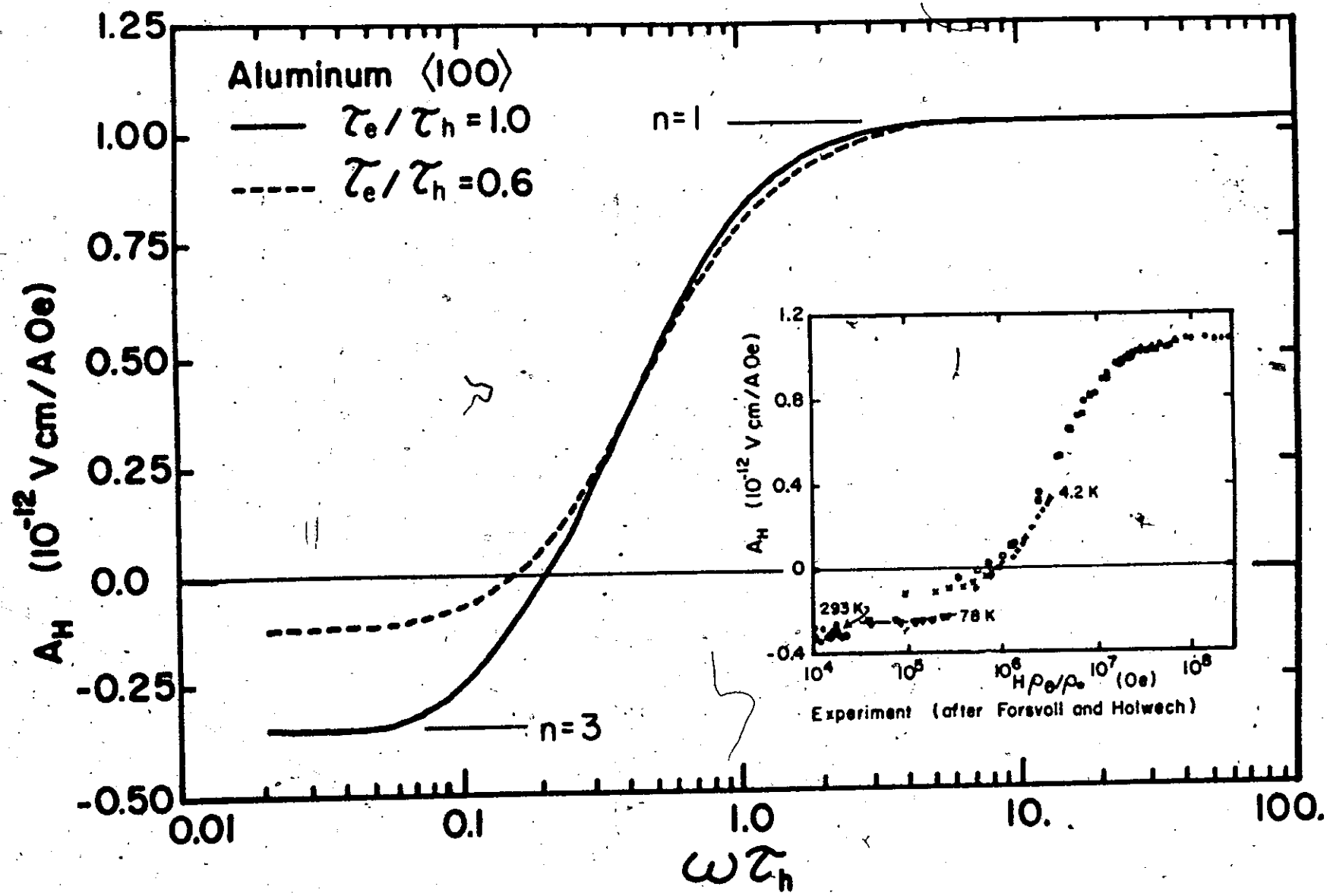
Aluminum ⟨100⟩
$\tau_e/\tau_h = 1.0$
$\tau_e/\tau_h = 0.6$
n=1
n=3
A_H (10^{-12} V cm/A Oe)
$\omega\tau_h$
1.25
1.00
0.75
0.50
0.25
0.0
-0.25
-0.50
0.01
0.1
1.0
10.
100.
1.2
0.8
0.4
0
-0.4
4.2 K
293 K
78 K
10^4
10^5
10^6
10^7
10^8
$H\rho_e/\rho_0$ (Oe)
Experiment (after Forsvoll and Holwech)

times", as is predicted by a more complete treatment of scattering than the catastrophic scattering approximation we have used, see Richards (1972-b) for example). The changes with temperature are larger than the sample to sample variations.

The zero-field resistivity is increased by some 11% by substituting $\tau_e/\tau_h = 0.6$ for the uniform relaxation time assumption. Since this same substitution only increases the high-field values of ρ_{xx} and ρ_{yy} by about 1%, the saturation magnetoresistance is reduced by somewhat more than 10%. This just reflects the fact that the electrons are much more effective carriers in the low-field limit than they are in the high-field limit, where their small orbit size, and thus small values of $<(k_x-\bar{k}_x)^2>$ and $<(k_y-\bar{k}_y)^2>$ make them ineffective transverse carriers. The reduction of the saturation magnetoresistance by this assumption brings the theory more nearly into agreement with experiment, with the major exception of the commonly observed high-field linear magnetoresistance, which will be discussed at some length later in this chapter.

The high-field saturation value of the longitudinal magnetoresistance decreases by some 4% with the substitution of $\tau_e/\tau_h = 0.6$ for a uniform relaxation time; that is, the high-field magnetoresistivity has increased, but not as much as ρ_o (refer to Table 1 for details).

B. Better Fermi Surface Models

The Fermi surface models we have used for all the calculations discussed thus far have suffered from the defect of having sharp cusps in the vicinity of Bragg reflections. The crystal potential rounds these sharp cusps, so that experiments do not show the linear low-field magnetoresistance which are present in our calculations. This does not sound particularly serious unless it is realized that the high-field calculations should be very nearly correct, and that this linear low-field magnetoresistance is an extra conductivity due to the cusps (or due to the discontinuities in $v(\theta)$ in the conventional low-field expansion (Ziman (1964), pg. 259). To demonstrate both the shortcomings and successes of our single-OPW Fermi surface models, we have calculated the <001> field dependence of the path-integral magnetoconductivity tensor using Ashcroft's (1963) four-OPW pseudopotential Fermi surface model of aluminum.

B.1 Indium Without α-Arms

Before comparing the results of the single-OPW and four-OPW Fermi surfaces of aluminum, let us examine the consequences of a much simpler modification of the single-OPW Fermi surface of indium. The third band electron surface of indium apparently does not include any pieces associated with the single-OPW "α-arms" (Mina and Khaikin, 1965). The α-arms are the third-band electron tubes oriented along <011>

directions. Mina and Khaikin found no evidence of the α-arms in their cyclotron resonance experiments, but only evidence of the third band ring (β arms, along <110> directions).

We have constructed a single-OPW Fermi surface model for indium without the α-arms, and have calculated the field dependence of the path-integral conductivity tensor component of this model for fields along <001>, <100>, <110> and <111> directions. The low-field resistivities, for currents along <100> and <001> directions ($\dot{\rho}_{<100>}$ and $\dot{\rho}_{<001>}$, respectively) are larger than the isotropic ρ_o which was calculated using the complete single-OPW Fermi surface. The low-field values of ρ_{xx}, ρ_{yy} and ρ_{zz} which are given in Table II are all derivable from $\dot{\rho}_{<100>}\tau$ and $\dot{\rho}_{<001>}\tau$, which are 3.56×10^{-20} Ω cm sec and 3.20×10^{-20} Ω cm sec respectively. That is, the resistivity is lower along the four-fold axis than it is perpendicular to the four-fold axis.

The low-field Hall coefficient shows considerable anisotropy, as may be seen in Table II and Fig. 31. The anisotropy of Garland's (1969) data, which are also shown in Fig. 27, is consistent with the calculations, but the vertical scale of his low-field data is not in agreement with our calculations. His data are for different samples, and so different horizontal scaling (different τ's) may

Table II

The galvanomagnetic effects of deleting the α-arms of In

field direction	<001>	<100>	<110>	<111>	
y-direction	[010]	[001]	[001]	[110]	
$\rho_o\tau$	3.03×10^{-20}	3.03×10^{-20}	3.03×10^{-20}	3.03×10^{-20}	Ω-cm-sec
$\rho^{\bullet}_{xx}$	3.56×10^{-20}	3.56×10^{-20}	3.56×10^{-20}	3.31×10^{-20}	Ω-cm-sec
$\rho^{\bullet}_{yy}$	3.56×10^{-20}	3.20×10^{-20}	3.20×10^{-20}	3.56×10^{-20}	Ω-cm-sec
$\rho^{\bullet}_{xx}$	3.20×10^{-20}	3.56×10^{-20}	3.56×10^{-20}	3.45×10^{-20}	Ω-cm-sec
$A_H(\omega\tau=.02)$	$-.0092\times10^{-12}$	$-.3299\times10^{-12}$	$-.3533\times10^{-12}$	-2.574×10^{-12}	$V\ cm\ A^{-1}Oe^{-1}$

High-field limit ratio of resistivity components of the calculations without the α arms to the calculations with α arms.

ρ_{xx}	.958	.952	.959	.949
ρ_{yy}	.958	.940	.955	.956
ρ_{zz}	1.014	1.181	1.056	1.101
ρ_{xy}	.980	.978	.980	.979

Figure 31. The uniform relaxation time path-integral Hall coefficient of indium without the single-OPW α arms, compared with experiment (after Garland, 1969). The orientations in this figure specify field directions.

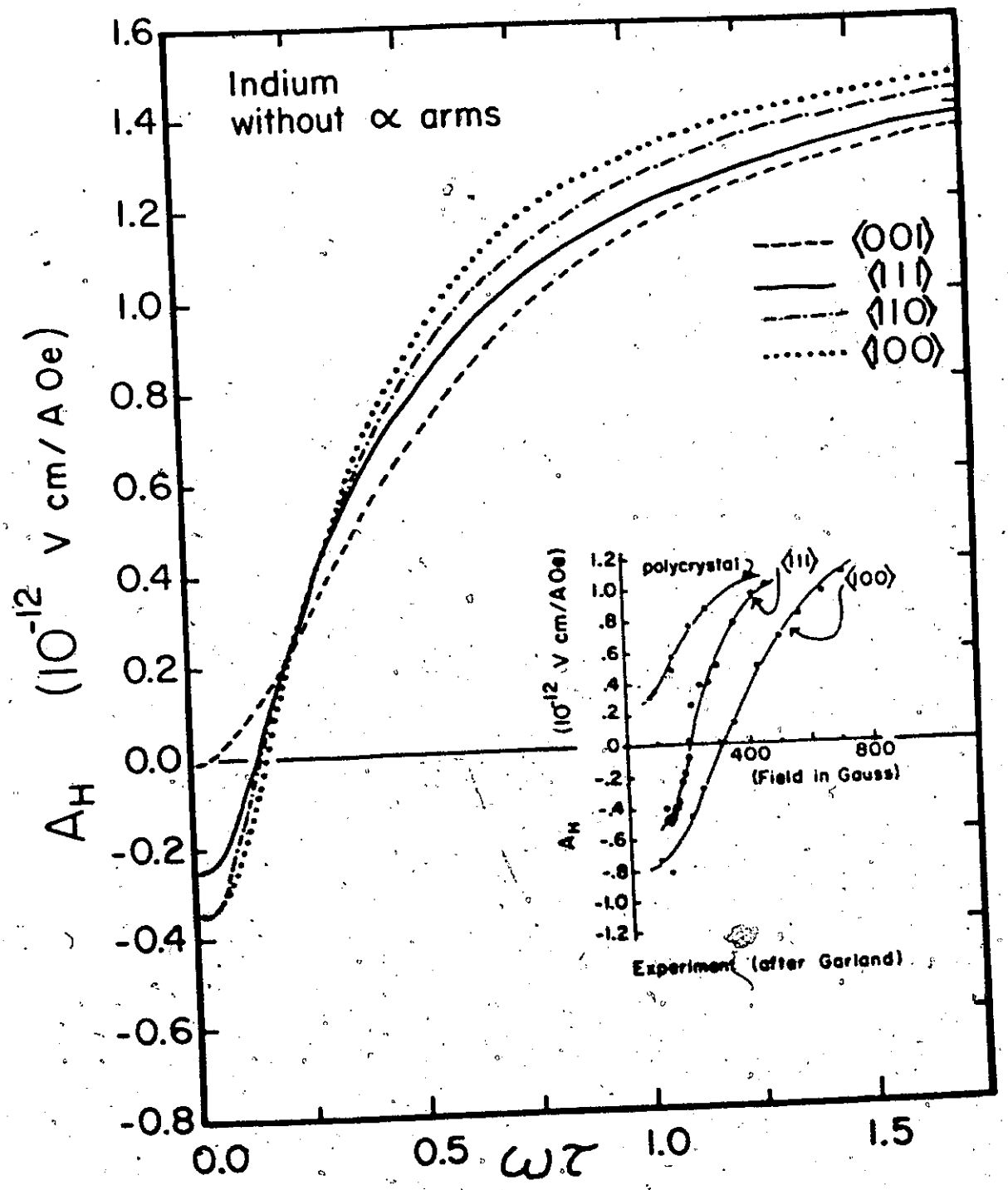
Indium
without α arms
⟨001⟩
⟨111⟩
⟨110⟩
⟨100⟩
A_H (10^{-12} V cm/A Oe)
$\omega\tau$
1.6
1.4
1.2
1.0
0.8
0.6
0.4
0.2
0.0
-0.2
-0.4
-0.6
-0.8
0.0
0.5
1.0
1.5
polycrystal
⟨111⟩
⟨100⟩
(10^{-12} V cm/A Oe)
A_H
400
800
(Field in Gauss)
Experiment (after Garland)

be chosen for the two samples. This points out the desirability of measuring the anisotropy of the galvanomagnetic properties of a single sample, since with such measurements it should be possible to sort out the effects of Fermi surface anisotropy and the effects of relaxation time anisotropy. In our calculations, the former has generated low-field anisotropy in the Hall coefficient, while the latter scales the low-field Hall coefficient uniformly, as was discussed in the previous section.

The high-field galvanomagnetic properties are not changed much by neglecting the α-arms. The major change is in the high-field Hall coefficient, which is decreased by about 2% for all field orientations. This is effectively a 2% increase in the net hole concentration. The change in the Hall term accounts for 4% of the 4 to 6% change in the high-field transverse resistivity. The change in ρ_{zz} in the high-field limit is quite anisotropic, being largest for directions where the z component of the carrier velocity is most nearly free-electron-like on the α arms.

B.2 Aluminum - Four-OPW Model

The improved Fermi surface model which was used for aluminum was Ashcroft's (1963) four-OPW pseudopotential model. The basis states for the wavefunction expansion are the plane waves, $\exp(i(\vec{k} - \vec{q}_j)\cdot\vec{r})$, orthogonalized to the ion cores. The four values of the reciprocal lattice vectors

$\vec{g}_j$ (giving the four plane waves orthogonalized to the core states) are (000), (002), (111), and $(1\bar{1}1)$ in units of $2\pi/2a$. for $\vec{k}$'s in the two irreducible $1/48^{th}$'s of the Brillouin zone which are closest to these reciprocal lattice vectors. Solving the energy eigenvalue problem resulting from the four-OPW expansion of the Schrodinger equation is equivalent to solving for the eigenvalues of a four plane wave expansion with a different potential. This is the pseudopotential, which incorporates the orthogonalization condition, and is a weaker potential than the original potential. A great computational simplification is achieved if the pseudopotential is assumed to be a true (or "local") potential, as Ashcroft has done. In this case the energy eigenvalue problem reduces to solving the secular equation:

$$\mathrm{Det}\ ((T_{\vec{g}i}-E)\delta_{ij} + V(\vec{g}_i-\vec{g}_j)) = 0 \qquad [16]$$

where $T_{\vec{g}i} = \frac{\hbar^2}{2m}(\vec{k}-\vec{g}_i)^2$ is the kinetic energy, and $V(\vec{g}_i-\vec{g}_j)$ is the $(\vec{g}_i-\vec{g}_j)$ Fourier component of the potential. Since $V(0)$ may be incorporated into E, the explicit secular equation is

$$\begin{vmatrix} \frac{\hbar^2}{2m}\vec{k}^2-E & V(002) & V(111) & V(111) \\ V(002) & \frac{\hbar^2}{2m}(\vec{k}-(002)2\pi/a)^2-E & V(111) & V(111) \\ V(111) & V(111) & \frac{\hbar^2}{2m}(\vec{k}-(111)2\pi/a)^2-E & V(002) \\ V(1\bar{1}1) & V(111) & V(002) & \frac{\hbar^2}{2m}(\vec{k}-(1\bar{1}1)2\pi/a)^2-E \end{vmatrix} = 0$$

[17]

There are three parameters for the four-OPW Fermi surface: V(002), V(111) and E_F, the Fermi energy. Ashcroft (1963) fitted these three parameters with de Haas-van Alphen effect data, and the condition that the Fermi surface volume in the extended zone scheme correspond to three electrons per atom (which he found to be nearly equivalent to the condition that the cyclotron mass be normalized to the single-OPW cyclotron mass). These values which we have used are $V_{(100)} = .0855$, $V_{(111)} = .0281$ and $E_F = 0.4280$ in atomic units.

Although the band structure which is determined using the pseudopotential with four OPW's has not converged (that is, taking the same pseudopotential form and more OPW's results in an appreciably different band structure), the four-OPW model with the three parameters (2 pseudopotential parameters and the Fermi energy) as fitted by Ashcroft (1963) has been rather successful in accounting for the measured properties of aluminum (Greissen and Sorbello, 1972). Although there is still a line of contact between the second and third bands near the W point of the zone, the sharp cusps of the single-OPW model have otherwise been rounded off, without introducing too large a computational burden for our purposes. To reduce the computational burden as much as possible, full use was made of the rotational and mirror symmetry of the orbits. The path-integrals were evaluated in terms of the analytic arc integrals described in Chapter II, with the arc

parameters $v_\perp$, v_z, $k_\perp$, and angles α and β determined numerically from the four-OPW band structure. The larger orbits each required the evaluation of about 30 arcs (for the irreducible one-eighth of the orbit) to obtain convergence of the path integrals in the low-field limit. The single-OPW model required only 2 arcs to describe the equivalent one-eighth of the orbit, although this orbit symmetry was not utilized. Although the four-OPW model (for the field along <001>) nominally required less than twice the computer time that the single-OPW model required; much more human intervention was required for the four-OPW model, to guide the arcs around lines of contact, to follow the electron and hole orbits in the proper sense, and to choose the best numerical step sizes for the different orbits. Thus only the <001> direction was evaluated for the four-OPW model.

Calculations of σ_{xx} ($\sigma_{xx}=\sigma_{yy}$), σ_{xy} and σ_{zz} are compared for the single-OPW and four-OPW models in Fig. 32. In the high field limit σ_{xx} and σ_{xy} of the two models agree very well. The major differences are in the low-field limit of the conductivity, the low to intermediate field dependences, and in the high-field value of σ_{zz}. A similar comparison of the resistivity components of the two models is given in Fig. 33.

The calculated zero field resistivity, ρ_o, is larger for the four-OPW model than for the single-OPW model;

Figure 32. The uniform relaxation time path-integral conductivity of aluminum, for the field along <100>. The dashed lines are the conductivity components calculated using the single-OPW Fermi surface, and the solid lines are the four-OPW calculations.

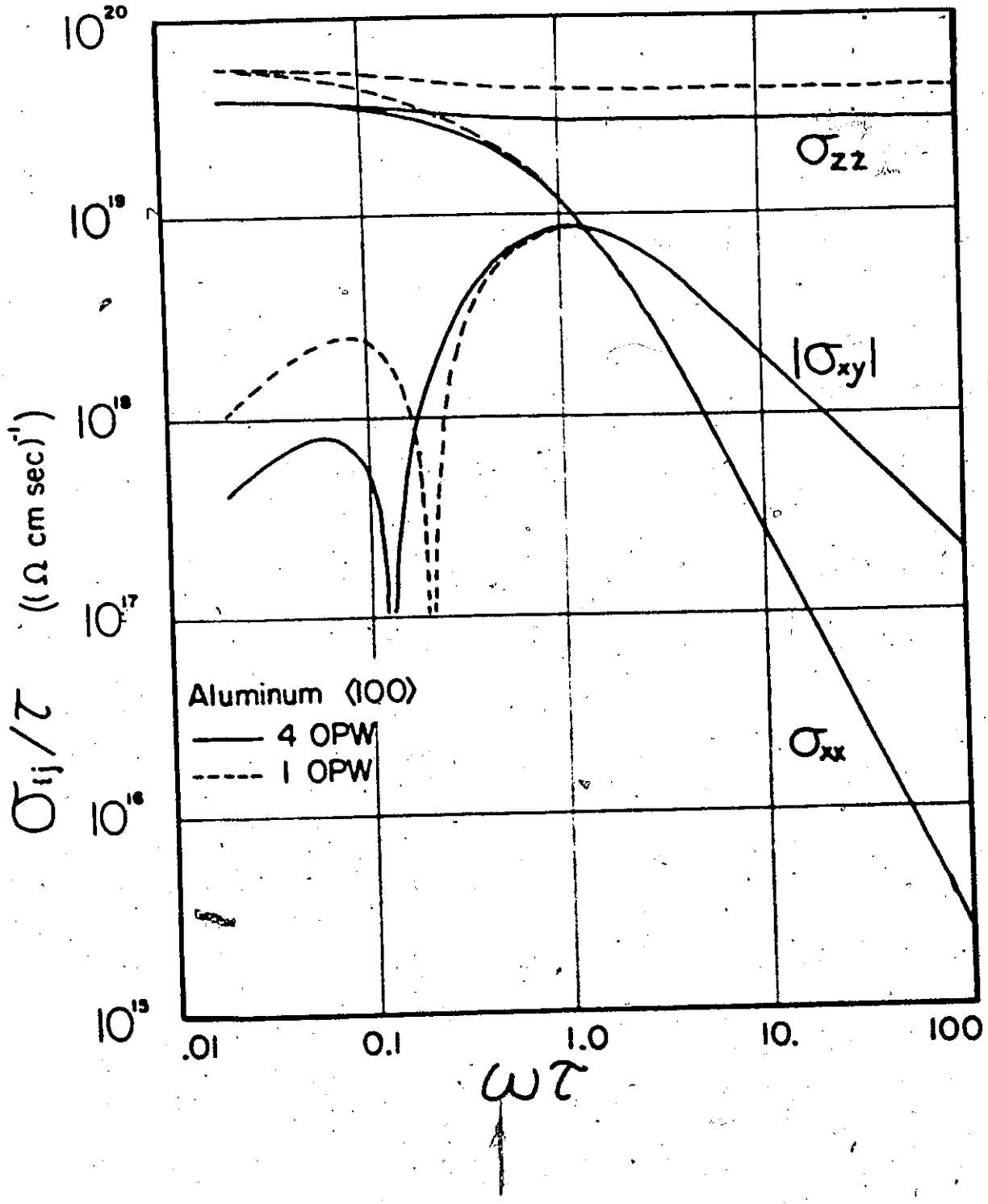
10^{20}
10^{19}
10^{18}
10^{17}
10^{16}
10^{15}
σ_{ij}/τ ((Ω cm sec)$^{-1}$)
σ_{zz}
$|\sigma_{xy}|$
σ_{xx}
Aluminum ⟨100⟩
4 OPW
1 OPW
.01
0.1
1.0
10.
100
$\omega\tau$

Figure 33. A comparison of the field dependence of the single-OPW (dashed line) and four-OPW (solid line) resistivity components of aluminum, calculated for the field along <100> using the uniform relaxation time path-integral.

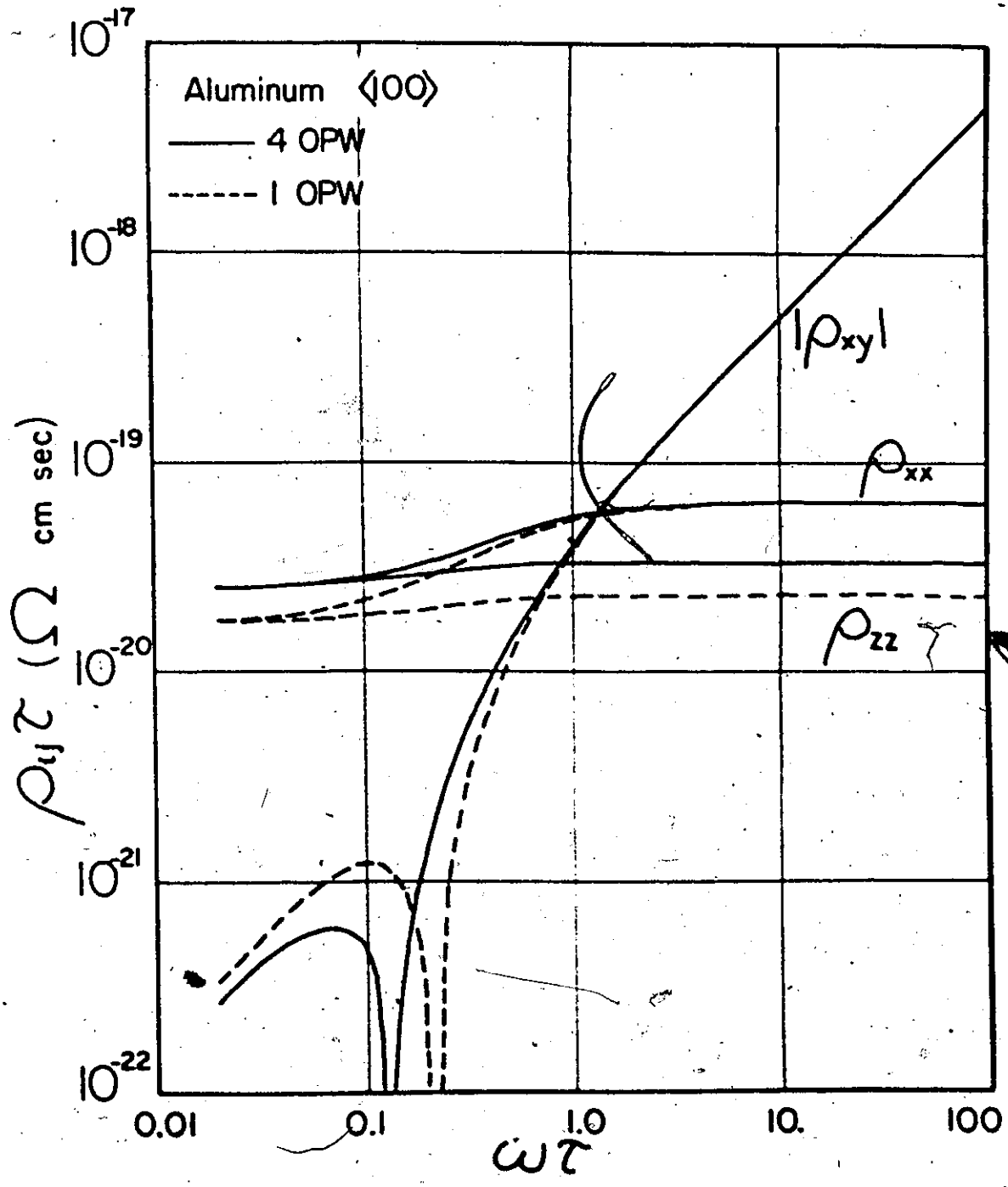
Aluminum ⟨100⟩
4 OPW
1 OPW
10^{-17}
10^{-18}
10^{-19}
10^{-20}
10^{-21}
10^{-22}
$\rho_{ij}\tau$ (Ω cm sec)
$|\rho_{xy}|$
ρ_{xx}
ρ_{zz}
0.01
0.1
1.0
10.
100
$\omega\tau$

$\rho_o\tau = 2.91\times10^{-20}$ Ω cm sec for the four-OPW model, compared with $\rho_o\tau = 1.95\times10^{-20}$ Ω cm sec for the single-OPW model. This resistivity increase reflects the smaller surface area, and smaller Fermi velocity (near Bragg reflections) of the four-OPW model. (Recall that ρ_o may be expressed as a surface integral of $v_F\tau$.) The smaller Fermi velocity affects ρ_{zz} almost equally in all fields - the ratio of the ρ_{zz}'s of the two models are 1.53 in the low-field limit, and 1.45 in the high-field limit. The longitudinal magnetoresistances of the two models are plotted as the lower curves in Fig. 34. The lower four-OPW value is due mainly to the rounding of the Fermi surface cusps, which generates a smaller longitudinal conductivity for the third zone electrons and the central band of orbits on the four-OPW hole surface. The electron orbits are smaller, with the Fermi velocity smaller than the free electron Fermi velocity, and the central band of orbits on the hole surface of aluminum with the field along <100> has v_z values that, due to the geometrical rounding, are much smaller than the corresponding v_z values on the single-OPW surface, for fields along <100>. The <100> direction is a singular direction in the single-OPW model, since it is only in this direction where $\langle v_z \rangle$ is non-zero for the central hole orbits. The <100> direction is not singular in this sense in the four-OPW model.

Figure 34. A comparison of the single-OPW (dashed lines) and four-OPW (solid lines) magnetoresistance calculated for aluminum.

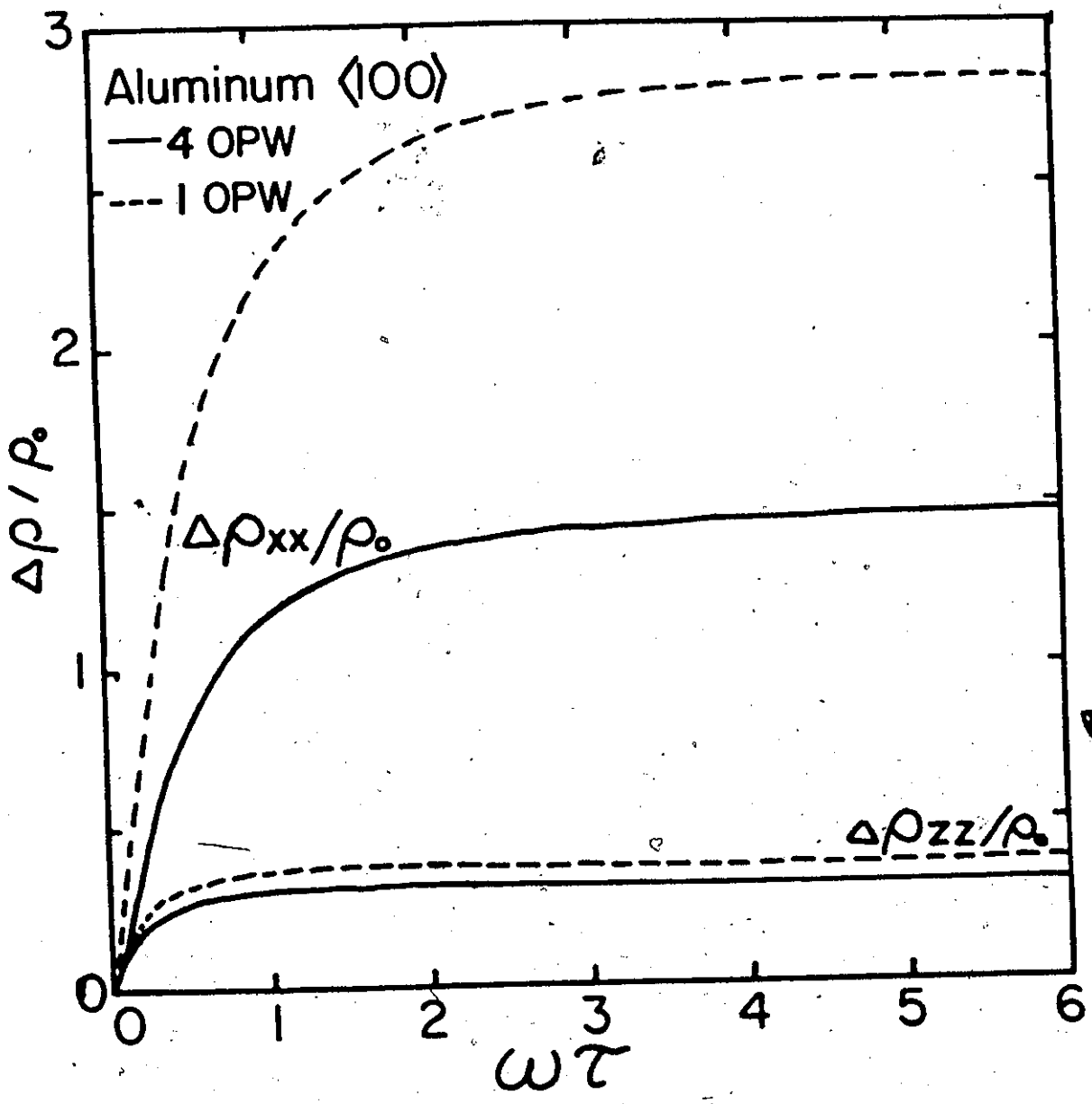
Aluminum ⟨100⟩
—4 OPW
---1 OPW
Δρxx/ρo
Δρzz/ρo
Δρ/ρo
ωτ
0
1
2
3
4
5
6

The change in ρ_o also affects the transverse magnetoresistance, whose field dependences are also compared in Fig. 34, but in this case because there is only a small change in the high-field transverse resistivity, the four-OPW transverse saturation magnetoresistance is much smaller than the single-OPW magnetoresistance (1.42 compared to 2.83).

The Hall coefficients of the two calculations are compared in Fig. 35. In the high-field limit, the rounding of the electron and hole bands may be seen to be equal in volume - the Hall coefficients both correspond to one hole per atom. In the low-field limit, where the electrons are dominating the Hall conductivity, the effect of the reduction in size of the electron pieces of the Fermi surface may be seen. The four-OPW low-field Hall coefficient is less negative than that of the single-OPW model. Qualitatively, this has the same effect as the reduction of the electron relaxation time, which was discussed in a previous section. To distinguish between these two mechanisms would probably require reliance on the measured anisotropy of the Hall coefficient within one sample.

The changes introduced in $\rho_{ij}(H)$ by including the effects of the crystal potential have brought the transverse magnetoresistance and low-field Hall coefficient closer to

Figure 35. A comparison of the single-OPW (dashed line) and four-OPW (solid line) Hall coefficient of aluminum, calculated using the uniform relaxation time path-integral, for fields along <100>.

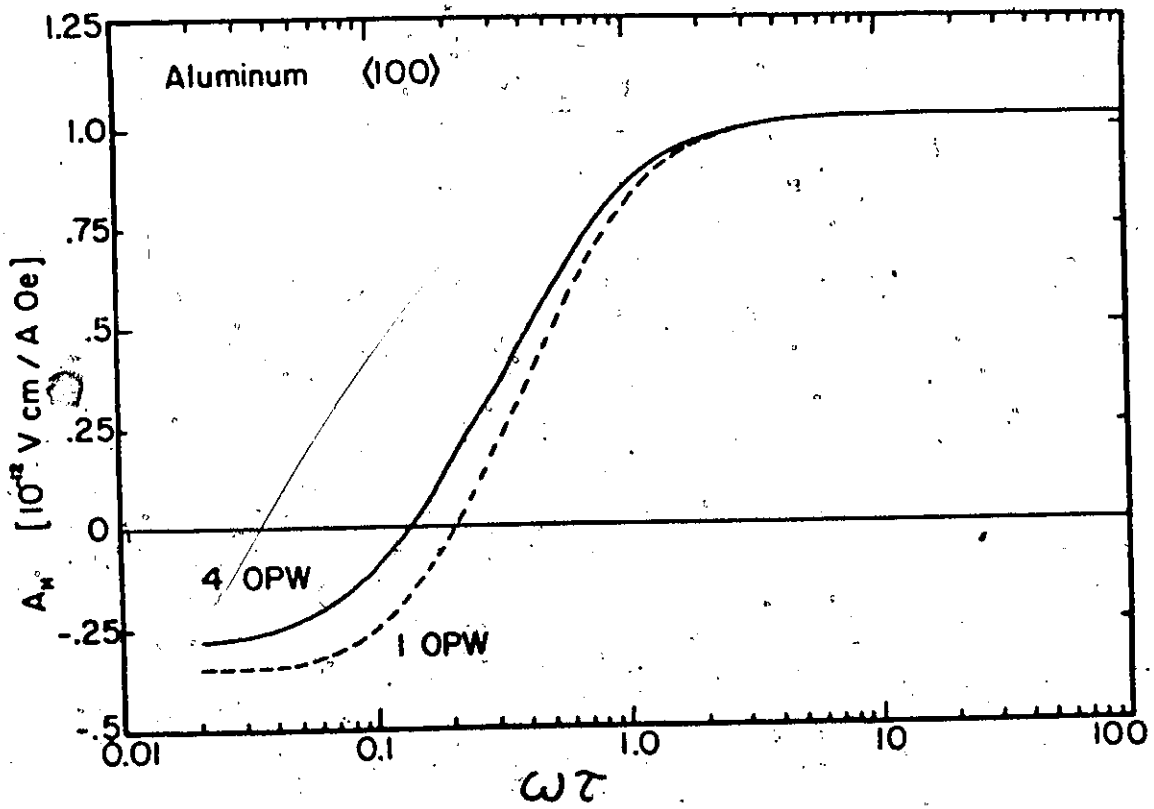
Aluminum ⟨100⟩
1.25
1.0
.75
.5
.25
0
-.25
-.5
A_H [10^{-12} V cm / A Oe]
4 OPW
1 OPW
0.01
0.1
1.0
10
100
$\omega\tau$

the experimental results.

C. Linear High-field Transverse Magnetoresistance

The linear high-field magnetoresistance which is observed in uncompensated metals with no open orbits (Kesternich and Ullmaier (1971), for Al; Garland (1969), for In; Babiskin and Siebemann (1971), for K) cannot be accounted for on the basis of the simple Lifshitz theory of galvanomagnetic properties. The linear component is quite sensitive to sample preparation and crystal defects. The purpose of this section is not to review all theories of the linear magnetoresistance, but to examine the anisotropy of the transverse linear term predicted by one class of theories and compare it to the observed anisotropy, for aluminum.

The observed high-field transverse linear magnetoresistance indicates that the transverse conductivities have been enhanced from a H^{-2} dependence to a H^{-1}, or rather a $|H^{-1}|$ dependence. This transverse conductivity enhancement may be viewed as a magnetically enhanced scattering, or a magnetic reduction of the relaxation time. It should be noted that the enhanced scattering time increases the high-field transverse conductivity because it is caused by, rather than relaxed by, scattering.

The observed anisotropy of the high-field linear magnetoresistance slope offers a tantalizing clue as to its origin. This slope is largest for fields along <110> as

is shown in Fig. 36 (Kesternich and Ullmaier 1971) - the axis of the electron "cylinders". If the transverse conductivity enhancement were an orbital enhancement of the form of $(1+\omega_c t)$ (where t is a free parameter) might not the smaller masses along <110> give rise to the larger linear magnetoresistance? Since our calculations can check such a hypothesis, we proceeded to do so.

Richards (1972-a) has predicted just such an enhancement in the high-field regime where the effects of Landau level quantization become important. The Shubnikov-de Haas effect is just such an effect, usually attributed to an oscillatory (in 1/H) relaxation time which arises from the oscillatory density of states which is available as the final states of scattering events. Richards proposes that the oscillatory density of states must <u>also</u> be included explicitly in the integration over energy. He concludes that pure diffusive scattering (small angle scattering that is mainly scattering <u>within</u> a Landau level) will enhance the semiclassical transverse conductivity of an orbit by a factor F,

$$F = 1. + 2/(\exp(2X_D)-1) \qquad [18]$$

where $X_D = \frac{2\pi^2 k_B}{\hbar\omega_c} T_D$, and T_D is the Dingle temperature. This is approximately of the form, for small X_D, of $(1 + \frac{\omega_c \tau_\Gamma}{\pi})$,

where τ_Γ is the Landau level lifetime. To see if Richards' (1971) prediction of an intrinsic linear magnetoresistance could account for the observed anisotropy, we applied an enhancement of the form of Eq. [18] to the path-integral transverse conductivities of each orbit, where ω_c is the cyclotron frequency of the orbit, and τ_Γ/τ is an adjustable parameter which is proportional to the Landau level lifetime in Richards' theory. If the linear magnetoresistance were generated by any such orbital enhancement of the semiclassical path-integral transverse conductivities, we would expect some value of τ_Γ/τ would reproduce both the slope and the anisotropy of the slope of the linear magnetoresistance. This was not found to be the case, as may be seen in Fig. 36. The observed maximum in slope with the field along <110> was not reproduced, and so we conclude that the linear magnetoresistance in aluminum is not a simple orbital enhancement of the transverse conductivities. The linear term in Richards' theory also seems to become apparent at higher fields than is found experimentally. There are of course other theories of the linear magnetoresistance (for a summary, see Falicov and Smith 1972), but these theories cannot be checked directly by our calculations.

The fact that, with care, it is possible to prepare potassium (Babiskin and Siebenmann, 1969, 1971) and aluminum (Chapter IV) which exhibit little or no linear magnetoresis-

Figure 36. A comparison of the anisotropy of the linear magnetoresistance of aluminum measured by Kesternich and Ullmaier (1971) and the predictions of Richards' (1972-a) theory. The measured and calculated field dependences are shown for fields along <110> and along <111>, with the current along <112>. Note there is an offset of the two calculated sets of curves. The calculations are for different ratios of Landau level lifetime (τ_Γ) to the transport lifetime on the hole surface (τ_h). The calculations assume $\tau_e/\tau_h = 0.6$, and used the single-OPW Fermi surface of aluminum.

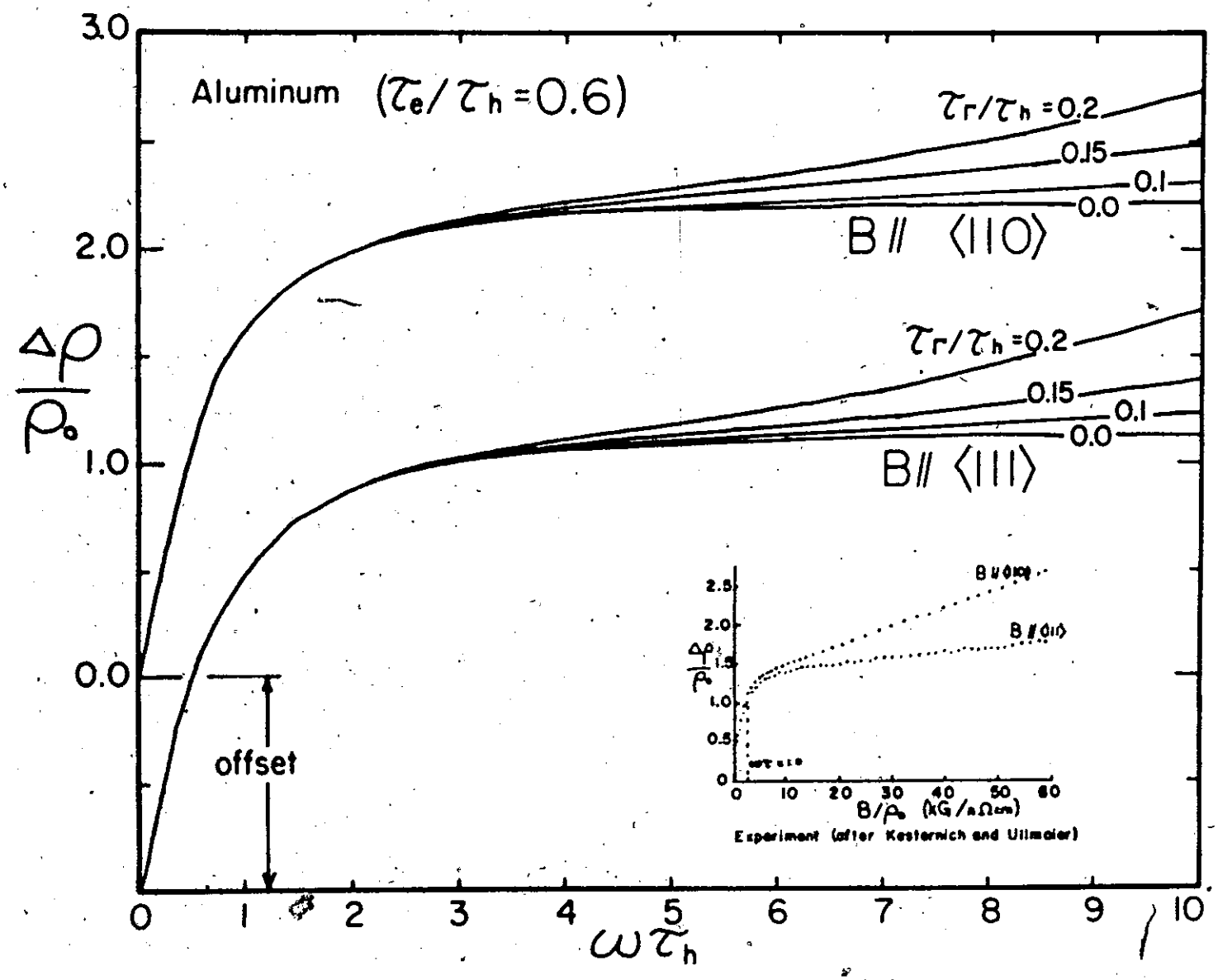
Aluminum (τ_e/τ_h = 0.6)
τ_r/τ_h = 0.2
0.15
0.1
0.0
B // ⟨110⟩
τ_r/τ_h = 0.2
0.15
0.1
0.0
B // ⟨111⟩
offset
$\Delta\rho/\rho_0$
$\omega\tau_h$
3.0
2.0
1.0
0.0
0
1
2
3
4
5
6
7
8
9
10
B // ⟨100⟩
B // ⟨111⟩
B/ρ_0 (kG/nΩcm)
Experiment (after Kesternich and Ullmaier)

tance suggests that this behaviour is not intrinsic, but rather is related to the defect structure of a sample. These sample inhomogeneities may make the diffusive term important in the Boltzmann transport equation (Eq. [3]). The important structure for these effects would be microstructure that is small compared to the zero-field mean free path, but not small compared to a high-field cyclotron orbit diameter. Such structure would only affect the low-field properties in an average way which could be adequately treated theoretically assuming a homogeneous sample. In the high-field limit, current streamlining (or diffusion) would result, as Babiskin and Siebenmann (1969,1971) have proposed. There does appear to be a correlation between small orbits and large linear magnetoresistance in those samples which exhibit this effect. The longitudinal magnetoresistance has a larger "linear" term than have the transverse terms in potassium (Simpson, 1973) where the smallest orbits (in both real and reciprocal space) are limit point orbits which contribute most strongly to the longitudinal conductivity. In aluminum, the largest linear term is generally observed for fields along <110> (Kesternich and Ullmaier (1971), Borovik and Volotskaya (1965)), which is an axis of two electron "tubes". It is difficult to explain this correlation using any homogeneous transport theory -

wherein we expect the high-field magnetoresistance to be but little affected by such small orbits with small values of $<(k_x-\bar{k}_x)^2>$ and $<(k_y-\bar{k}_y)^2>$.

These observations qualitatively seem to fit the ideas of Babiskin and Siebenmann about the origin of the linear magnetoresistance, outlined above, and strengthen their concept of a "macroscopic magnetoresistance" attributable to the current distribution, with magnetic field, over dimensions greater than the mean free path (a kinky helix whose mean radius decreases as the field increases). The resulting macroscopic current redistribution would cause the current streamlines to be pinched, increasing the apparent magnetoresistance approximately linearly as the pinching increased with field.

An unequivocal resolution of the cause of the observed linear magnetoresistance lies probably in a very careful characterization of the experimental samples (to ensure that the homogeneity condition is satisfied, or to specify the inhomogeneities if it is not), combined with anisotropy measurements of the magnetoresistance slope. Calculations of the anisotropy, as we have done for Richards' theory, can then eliminate some theories, which otherwise have no real test, since fitting only the slope with one adjustable parameter (as most proposed theories have) cannot be very convincing in itself.

CHAPTER VII

CONCLUSIONS

The anisotropy of the field dependence of the semi-classical magnetoresistivity tensor of crystalline metals provides a powerful test of transport theories. The goal of charge transport theories, the prediction of the tensor function $\overleftrightarrow{\rho}(\vec{H})$ in terms of the independently measured Fermi surface parameters, should be focussed more on the anisotropy than on the field dependence for the field in only one orientation. This approach requires reliable experimental methods of measuring the anisotropy, and requires more computational effort on the part of the theorist, but the rewards are much greater. Not only is it a more complete and more rigorous test, but the extensive nature of this comparison permits even a simple theory to show not only its deficiencies, but also the ways in which it agrees with experiment. In this latter respect, the anisotropy is a more forgiving kind of comparison than the very intensive comparison for only one field orientation, since even if the theory accurately accounts

for only that part of the conductivity which generates most of the anisotropy, there will be some measure of agreement. Even if there are no open or extended orbits on the Fermi surface, the Bragg reflections of the carriers can generate very considerable anisotropy in the theoretical $\overleftrightarrow{\rho}(\vec{H})$ which must then be compared with experiment.

For aluminum, the induced torque technique gave fully reproducible results (which the four-probe method did not), and provided the necessary extensive data for the comparison with the path-integral predictions. There was excellent agreement between these experiments and the path-integral theory, with a RMS deviation of less than 2.5%. The rather involved dependence of the induced torque on $\overleftrightarrow{\rho}(\vec{H})$ was no handicap. The path-integral calculations and the induced torque technique complemented one another beautifully, the calculations being supported by the experiments and the experimental results being explained by the theory. The induced torque anisotropy of some 10% was interpreted as confirmation of the calculated longitudinal conductivity anisotropy, which required a careful k_z integration over all orbits, and could not have been determined using a small number of "representative" orbits.

Induced torque experiments in high-purity aluminum (to $\omega\tau \sim 25$) showed no sign of the linear transverse magnetoresistance which is regularly reported in four-probe measurements, except for a narrow (±3°) band around <001>

which was tentatively identified as a consequence of magnetic breakdown. The reported anisotropy of the linear magnetoresistance slope (measured by the four-probe technique) was used to show that this linear magnetoresistance cannot be due to a simple orbital enhancement of the path-integral conductivity, as had been suggested.

The path-integral method was found to be an efficient means of evaluating the semi-classical conductivity tensor function. It is a technique which can encompass arbitrary Fermi surfaces, anisotropic Fermi velocities (including anisotropic electron-phonon mass enhancements), anisotropic relaxation times and magnetic breakdown. It is valid for any magnetic field and is economical of computer time: even for our simplified Fermi surface models consisting of re-mapped spheres, the evaluation and ordering of the single-OPW Fermi surface arcs took some 20 times as long as the path-integral evaluation (assuming a uniform relaxation time) for one $\omega\tau$ value, (although the latter procedure was carefully optimized while the former was not). Thus the use of high-field approximations in the calculation of magnetoconductivity tensor components is not justifiable except for cases where the catastrophic scattering approximation is not to be applied. The anisotropy of $\overleftrightarrow{\rho}(\vec{H})$ should be of considerable assistance in determining the form of

the scattering and its anisotropy. The separability of Fermi surface geometry effects and the effects of scattering anisotropy were demonstrated using the low-field Hall coefficient anisotropy and value.

The single-OPW Fermi surface model of aluminum was shown to be a good model for most of the high-field galvanomagnetic properties, but for $\omega\tau \lesssim 1$ the effects of the lattice potential are important, as they are for the longitudinal magnetoresistivity in any field regime. The single-OPW results also indicated that the longitudinal-transverse magnetoconductivity components can be safely ignored, for practical purposes, in the matrix inversion to obtain the magnetoresistivity tensor.

The different calculated anisotropies of the galvanomagnetic properties of aluminum and indium were related to the geometric features of the Fermi surface from which they arose. This understanding of these semi-classical effects of the Fermi surface geometry is a prerequesite for harnessing the full potential of the galvanomagnetic anisotropy and its field and temperature dependence, for the testing of transport theories and scattering mechanisms.

BIBLIOGRAPHY

Amundsen, T., Proc. Roy. Soc. (London) 88, 757 (1966).

Amundsen, T., and Seeberg, P., Phys. Lett. 25-A, 718 (1968).

Ashcroft, N.W., Phil. Mag. 8, 2055 (1963).

Ashcroft, N.W., Phys. Kondens. Materie 9, 45 (1969).

Babiskin, J., and Siebenmann, P.G., Phys. Kondens. Materie 9, 113 (1969).

Babiskin, J., and Siebenmann, P.G., Phys. Rev. Lett. 27, 1361 (1971).

Balcombe, R.J., Proc. Roy. Soc. (London) A275, 113 (1963).

Balcombe, R.J., and Parker, R.A., Phil. Mag. 21, 533 (1970).

Barett, C.S., Advances in X-ray Analysis (Plenum Press, New York, 1962), p. 33.

Borovik, E.S., Zh. Eksp. Teor. Fiz. (USSR) 23, 83 (1952).

Borovik, E.S., and Volotskaya, V.G., Zh. Eksp. Teor. Fiz. (USSR) 48, 1554 (1965), (trans: Soviet Physics JETP 21, 1041).

Castaing, B., and Goy, P., J. Phys. C: Solid State Phys. 6, 2040 (1973).

Chambers, R.G., Proc. Roy. Soc. (London) A238, 344 (1956).

Chambers, R.G., and Jones, B.K., Proc. Roy. Soc. (London) A270, 417 (1962).

Chiang, Yu. N., Eremenko, V.V., and Shevchenko, O.G., Zh. Eksp. Teor. Fiz. (USSR) 57, 1923 (1969), (trans: Soviet Phys. JETP 30, 1040).

Delaney, J.A., and Pippard, A.B., J. Phys. C: Solid State Phys. 4, 435 (1971).

Falicov, L.M., and Sievert, P.R., Phys. Rev. 138, A88 (1965).

Falicov, L.M., and Smith, H., Phys. Rev. Lett. 29, 124 (1972).

Feder, J., and Lothe, J., Phil. Mag. 12, 107 (1965).

Fickett, F.R., Phys. Rev. B.3, 1941 (1971).

Forsvoll, K., and Holwech, I., Phil. Mag. 10, 921 (1965).

Gaidukov, Yu. P., Zh. Eksp. Teor. Fiz. (USSR) 49, 1049 (1965), (trans: Soviet Phys. JETP 22, 730).

Garland, J.C., Phys. Rev. 185, 1009 (1969).

Garland, J.C., and Bowers, R., Phys. Rev. 188, 1121 (1969).

Gilman, J.J., The Art and Science of Growing Crystals (Wiley, New York (1963)), p. 322.

Greissen, R., and Sorbello, R.S., Phys. Rev.B.6, 2198 (1972).

Harrison, W.A., Phys. Rev. 118, 1190 (1960).

Heidenreich, R., J. App. Phys. 20, 993 (1949).

Holroyd, F.W., Datars, W.R., and Douglas, R.J., Can. J. Phys. Can. J. Phys. 51, 1786 (1973).

Kesternich, W., and Ullmaier, H., Phys. Lett. 36A, 411 (1971).

Lifshitz, I.M., Azbel', M.Ia., and Kaganov, M.I., Zh. Eksp. Teor. Fiz. (USSR) 30, 220 (1956-a), (trans: Soviet Phys. JETP 3, 143.

Lifshitz, I.M., Azbel', M.Ia., and Kaganov, M.I., Zh. Eksp. Teor. Fiz. (USSR) 31, 63 (1956-b), (trans: Soviet Phys. JETP 4, 41).

Lück, R., Phys. Stat. Sol. 18, 49 (1966).

Lutes, O.S., and Clayton, D.A., Phys. Rev. 138, A1448 (1965).

Mina, R.T., and Khaikin, M.S., Zh. Eksp. Teor. Fiz. (USSR) 48, 111 (1965), (trans: Soviet Phys. JETP 21, 1).

Pippard, A.B., Proc. Roy. Soc. (London) A282, 464 (1964).

Prange, R.E., and Kadanoff, L.P., Phys. Rev. 134, A566 (1964).

Richards, F.E., Bull. Am. Phys. Soc. 17, 74 (1972-a).

Richards, F.E., Proc. Thirteenth International Conference on Low Temperature Physics, (1972-b).

Simpson, A.M., J. Phys. F: Metal Phys. 3, 1471 (1973).

Vanerkooy, J., and Datars, W.R., Phys. Rev. 156, 671 (1967).

Visscher, P.B., and Falicov, L.M., Phys. Rev. B.2, 1518 (1970).

Volotskaya, V.G., Zh. Eksp. Teor. Fiz. (USSR) 44, 80 (1963), (Trans: Soviet Phys. JETP 17, 56).

Wagner, D.K., Phys. Rev. B.5, 336 (1972).

Young, R.A., Phys. Rev. 175, 813 (1968).

Ziman, J.M., Principles of the Theory of Solids, (Cambridge University Press, London, 1964).